RICE UNIVERSITY

Nosie measurement in strongly correlated systems

by

Liyang Chen

A THESIS SUBMITTED
IN PARTIAL FULFILLMENT OF THE
REQUIREMENTS FOR THE DEGREE

Doctor of Philosophy

APPROVED, THESIS COMMITTEE

Douglas Natelson, Chair of the committee
Professor of Physics and Astronomy

Pengcheng Dai
Professor of Physics and Astronomy

Hanyu Zhu
Assistant Professor of Material Science
and Engineering

HOUSTON, TEXAS
04/05/2023

ABSTRACT

Nosie measurement in strongly correlated system

by

Liyang Chen

Noise comes from the current or voltage fluctuations in devices. The three most common types of noise are thermal noise, 1/*f* noise, and shot noise. Correctly interpreting noise signal can provide extra information beyond common electron transport experiments. In this thesis, we used the noise signal to study the strongly correlated materials, and found interesting results in two different systems, a Mott insulator and a strange metal. This thesis starts from introduction of three common types of noise and their applications in Chapter 1, followed by the introduction of the Mott insulator in Chapter 2 and the strange metal in Chapter 3, especially V_2O_3 and $YbRh_2Si_2$ respectively. Then I introduce our noise measurement setup and calibration process in Chapter 4. In Chapter 5, we show our study of percolation and nano second fluctuators in the V_2O_3 metal insulator transition, through measuring both the low frequency(below 1MHz) and high frequency(10MHz-1GHz) 1/*f* noise spectrum dependence on bias and temperature. In Chapter 6, we shows our finding of strongly suppressed shot noise intensity in a $YbRh_2Si_2$ nanowire compared with a gold nanowire, and this may indicate the lack of well-defined quasiparticles in this strange metal. In Chapter 7, we discussed possible follow-up research based our projects. Supplementary information including probe design and experiments tips are attached in Appendix.

Acknowledgments

First of all, I would like to thank my advisor, Dr. Douglas Natelson, who provided me with invaluable guidance during the past six years. His advice and encouragement not only greatly helps me to grow as a researcher, but also supports me in everyday life. I would also like to thank Dr. Pengcheng Dai and Dr. Hanyu Zhu for being in my defense committee and provide insightful comments and suggestions for the projects.

I would like to thank all my collaborators for the projects, without whom this thesis would never be possible. I want to thank Dr. Yoav Kalcheim and Dr. Ivan K. Schuller for their effort on the V_2O_3 project, and Dr. Silke Paschen and Dr. Qimiao Si for their works on the $YbRh_2Si_2$ project.

I also want to thank Dr. Panpan Zhou, who has many important contributions to the projects. I also want to express my gratefulness to Dr. Loah Stevens, Dr. Xuanhan Zhao and Dale Lowder for all the inspirational discussions about experiemnt skills and the underlying physics of the projects, from which I benefited a lot.

Lastly, I would like to thank my friends and family for their unconditional support during my difficult times. Their love is the most precious gift I have ever received, and I'll always be grateful to have them in my life.

Contents

List of Figures

Chapter 1

Electronic noise

Electronic noise is the random fluctuations of the voltage or the current through an electrical device. The most common types of noise are thermal noise, 1/*f* noise (also known as flicker noise) , and shot noise. In this section, I introduce each type of noise and their related works.

1.1. Thermal noise

Thermal noise is also called Johnson–Nyquist noise. It was predicted since the Einstein's study of Brownian motion in 1906 [1], It was discovered experimentally by John B. Johnson in 1928 [2], and H. Nyquist performed the theoretical derivation of Johnson noise at the same time [3]. Classically Johnson-Nyquist noise comes from the random movement of electrons in an electrical device because of their Brownian motion. H. Nyquist calculated the thermal noise by means of thermodynamics and statistical mechanics. Here I briefly introduce how H. Nyquist did the derivation. Consider a circuit (Figure 1.1) made up with two identical resistors R_1 and R_2 with resistance R at same temperature T, and they are connected with non-dissipative wires of length l with characteristic impedance R. Let the speed of energy propagation be v. When the system enters thermal equilibrium state, the energy transmission from R_1 to R_2 must be equal to the energy transmission from R_2 to R_1. If we isolate the line from the resistors after the thermal equilibrium established, there would be complete energy reflection at the two ends and the energy would be trapped in the line. Now, we can describe the line as a one-dimensional cavity. The frequency of each resonant mode is $nv/2l$, where n is any integer greater than zero, and by classical equipartition each mode contains average energy k_BT, where k_B is Boltzmann's constant. So the total energy within frequency interval df is $2lk_BTdf/v$. This stored energy is the energy transmission happening in time period l/v and contains the contributions from both from R_1 to R_2 and R_2 to R_1. The power transferred from one resistor to another within frequency interval df is k_BTdf. If we model that this power comes from a voltage source along with the resistor, we find:

$$S_V df = 4k_BTRdf \text{ or } S_V = 4k_BTR \tag{1-1}$$

where $S_V(f)$ voltage noise power density (V^2/Hz). This is the common equation of thermal noise in the voltage form, it also can be expressed in current form as $S_I = 4k_BT/R$. One important feature is the thermal noise intensity is frequency independent. It is a white noise with constant value through the frequency domain, in the classical limit.

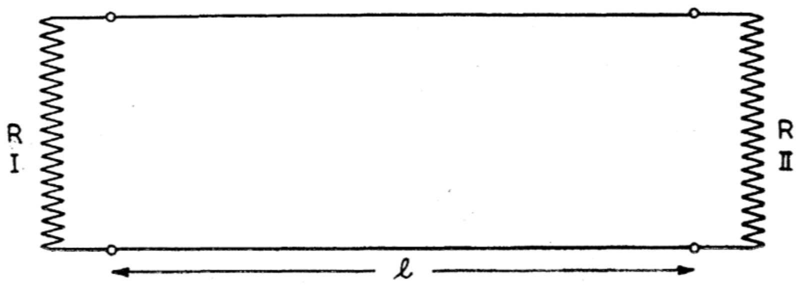

Figure 1-1 [1]: Diagram of two resistors transfering thermal energy through transmission line of length l.

The equation above is calculated based on the classical equipartition result that each electromagnetic mode has energy k_BT. If we consider the proper quantum canonical distribution, the average energy of each mode would be $\frac{hf}{e^{hf/k_BT}-1}$ [3], and the thermal noise expression would be

$$S_V(f) = \frac{4hfR}{e^{hf/k_BT} - 1} \tag{1-2}$$

where h is Plank's constant. When hf/k_BT is much smaller than 1, which is true in this thesis, the formula above reduces to the classical result, $S_V(f) = 4k_BTR$. For a sense of scale, T = 1 K corresponds to a frequency crossover of approximately 20 GHz, above which deviations from white noise would be expected.

The equivalent circuit diagram of a resistor with thermal noise is shown in Figure 1.2. R is an ideal stable resistor without resistance fluctuation. This system can be modeled as an equivalent stable constant resistor R in series with a voltage noise source V_{noise} or a stable constant resistor R in parallel with a current noise source I_{noise}.

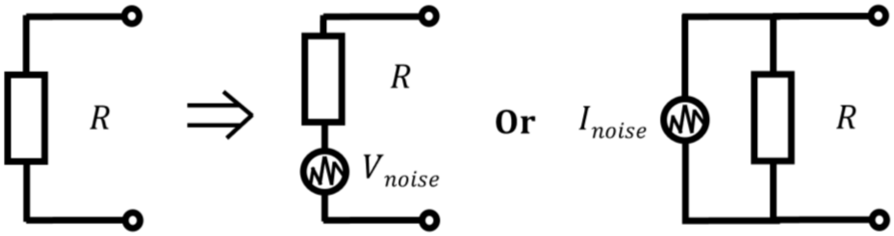

Figure 1-2: Diagram of equivalent electrical circuits of thermal noise of a stable resistor.

Thermal noise is universal in all devices and it decides the limit of signal to noise ratio in any measurement. The only way to reduce it is to lower the temperature. Although people in many industries, like communication [4], circuit design [5,6], and even biology [7,8], are annoyed by the existence of thermal noise, researchers have ways to utilize it. The most common usage is thermometry [9–12].

Using thermal noise to measure temperature has its own advantages and disadvantages. First, on the positive side, it does not require driving currents, on compared to other thermal sensors, so the heat dissipation can be reduced to a minimum, making noise thermometry a good candidate for low temperatures [13]. This was first realized in measuring lambda point of helium in 1959 [14] and recent advanced techniques has made it able to measure temperatures down to below 50 μK [15];

Secondly, since the thermal noise intensity is only decided by the real part of impedance and temperature, the sensor itself can be cheap and easy to obtain. In situations where the thermal sensors have to be placed in harsh environment like high temperature and corrosive, normal sensors will need to be replaced and recalibrated frequently, but thermal noise sensors don't need calibration beyond a resistance measurement because of universally well-defined intensity [9]; Thirdly, thermal noise can be used to directly measure the sample temperature. In real situations, no matter how close the thermal sensor to your sample, you cannot guarantee the temperature reading from the thermal sensor is exactly same as the local temperature of the sample. However, measuring the resistance and thermal noise of your sample can directly derive the local temperature of your sample.

Apart from the advantages mentioned above, the noise thermometry has some drawbacks making it less common. Firstly, the thermal noise signal is often small due to its nature. Unlike other thermal sensors, noise thermometry measures the current(voltage) fluctuation rather than current(voltage) itself, and this tiny signal can be easily corrupted by other noise such as amplifier input noise. This sets high requirements for a system that it must be able to measure small signals and block or eliminate unwanted noise. For example, people use cryogenic preamplifiers and two channels cross-correlated to reduce the input noise from preamplifiers. Secondly, the small size signal requires longer times to average. The researchers who succeeded in measuring temperature using noise thermometry below 50μK need 400 s averaging time to reach a statistical precision better than 1% for given bandwidth 100Hz [15], and agreement of better than 5% in comparison with standard thermometers in the entire temperature range. This means that what the noise thermometer measures is the average temperature during this 400 s averaging time. In other words, it cannot react quickly to the temperature change. This low temperature thermometer data is shown in the figure below, because author use SQUID to measure magnetic fluctuation, so the unit is magnetic flux noise:

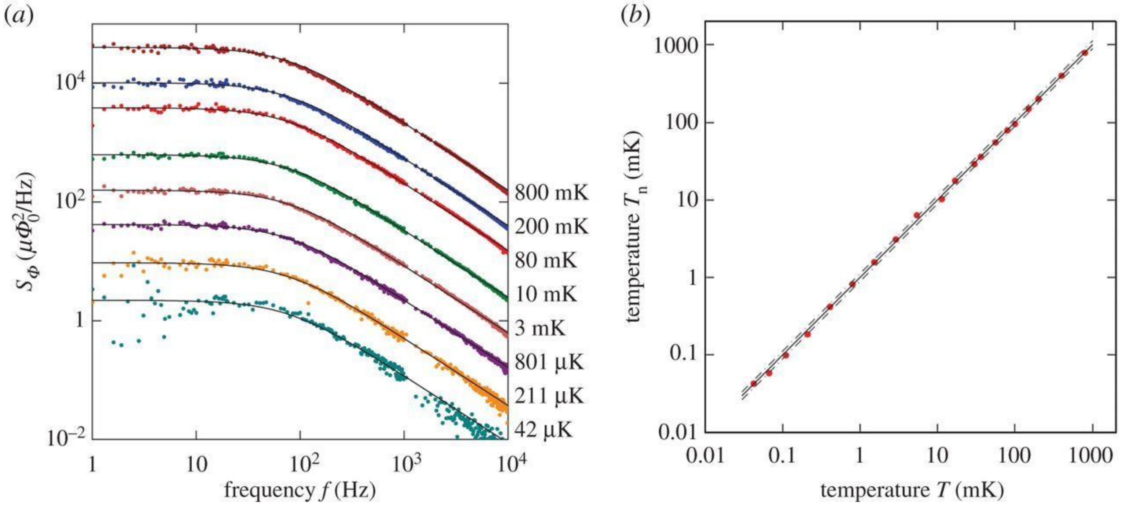

Figure 1-3 [15]: thermal noise thermometer. (a) Log-log scale thermal noise spectra at different temperature(42 μK to 800mK) as noted on the right end of each curves. Solid line fitting is used to extract the noise intensity at low frequency. (b) Comparison between deduced temperature from noise thermometer(red dots) and standard thermometers(solid line). The data fall in the 5% error range of standard thermometers(dashed lines).

1.2. 1/*f* noise

1/*f* noise or flicker noise is observed in almost all devices and materials [16–18]. Its noise spectrum from resistance fluctuations typically has a spectral density (mean square voltage fluctuations per unit bandwidth) $S(f) \sim 1/f^{\alpha}$, where f is the frequency and α is close to 1. Figure 1-4 shows a typical example of 1/f noise. In log scale and the low frequency side, the noise intensity vs frequency has a slope of -1, and the spectrum becomes flat at higher frequency because of thermal noise.

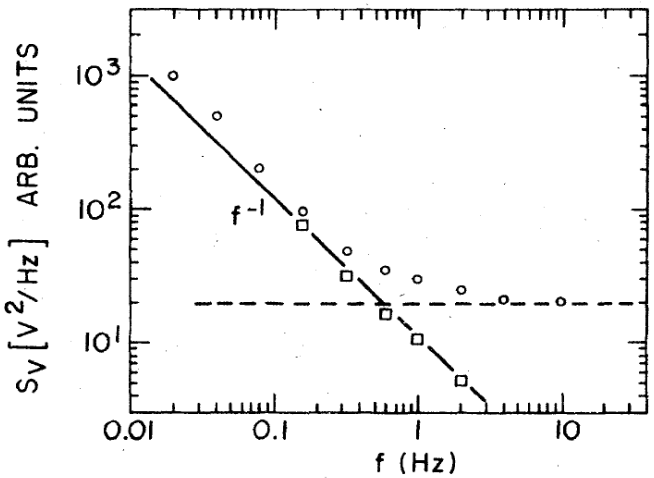

Figure 1-4 [19]: Typical $1/f$ noise spectrum with thermal noise. Circles are original spectrum, solid line indicates the slope equals -1, dashed line stands for thermal noise background, and squares are the pure $1/f$ noise through removing the thermal noise.

Because $1/f$ noise shows almost same frequency dependence in a lot of different systems, people have long tried to find a general model to explain its origin. There are two well-known models for now, one is raised by Hooge in 1969 [20], the other is proposed by McWhorter in 1957 [21].

Hooge proposed a model with an empirical formula for homogeneous semiconductors or metals [20,22]

$$\frac{S_R}{R^2} = \frac{\alpha}{fN} \qquad 1\text{-}3$$

Where S_R is the spectral power density of the resistance (□^{2}/Hz), R is the resistance, f is the frequency, N is the total number of free electrons, and α is an empirical dimensionless constant. He suggested that the $1/f$ noise comes from the fluctuation of mobility of each free electron, and this mobility fluctuation mainly comes from the interaction of electrons and the lattice. In 1981 [16], Hooge extended his formula to explain the $1/f$ noise in MOSFETs. Although majority of results of $1/f$ noise measurements can be described by this empirical relation, his formula can not be the ultimate answer because of some imperfections. For example, the integration of spectra from zero to infinity would diverge if the spectral always follows the form $S(f) \sim 1/f$, and there is no generally accepted theory so far for the Hooge formula.

The McWhorter model is also known as the number fluctuation model. It suggested that the 1/*f* noise is caused by the trapping and detrapping of carriers. More generally, people extended the mechanism to multiple two-level states. The switching of resistance between two discrete states would cause Lorentzian noise of the form

$$S_L(f) \propto \frac{\tau}{(2\pi f)^2 + (1/\tau)^2} \qquad \text{1-4}$$

Where τ is effective lifetime $\frac{1}{\tau} = \frac{1}{\tau_1} + \frac{1}{\tau_2}$, τ_1 and τ_2 are the lifetimes for the system to switch from one state to another. To produce a 1/*f* frequency dependence, the system should have a large number of two-level fluctuators of different characteristic lifetimes. Suppose the distribution function of τ is $D(\tau)$, then

$$S(f) \propto \int \frac{D(\tau)\tau}{(2\pi f)^2 + (1/\tau)^2} d\tau \qquad \text{1-5}$$

When $D(\tau)$ has the form $1/\tau$, the noise spectrum will have $1/f$ shape. For example, consider the an electron hopping between two different trap states. If the switching process is simple quantum tunneling, the tunnel rate will have form

$$\frac{1}{\tau} \propto \frac{1}{\tau_0} \mathrm{e}^{-l/l_0} \qquad \text{1-6}$$

Where l is the distance between localized traps, and τ_0 and l_0 are two constants. Under the assumption that the distribution of distances is uniform, in other words $D(l)$ is constant, we can get $D(\tau) \propto 1/\tau$ and $S(f) \propto 1/f$.

The $1/f$ noise in most cases is unwanted. For example, it decreases the signal to noise ratio in circuit, cause decoherence in quantum information [23–25], and can overwhelm everything useful in low frequency side when doing spectral analysis. Research tried to reduce $1/f$ noise by many methods [26–30]; one of the easy and practical ways to reduce $1/f$ noise in MOSFET is using switched bias to reduce accumulation of charge [29,30].

Apart from finding ways to reduce $1/f$ noise, scientists also found many ways to utilize it. For example, in biology, researchers use $1/f$ noise in the human brain and neurons to study the related cognitive processing speed [31] and aging [32,33]. In material science, $1/f$ noise can be used to extract trap density [34], mobility fluctuations [35], and charge density wave properties [36]. The example of finding charge density wave sliding in $\mathrm{1T-TaS_2}$ thin film is shown below, and more details can be found in [36]:

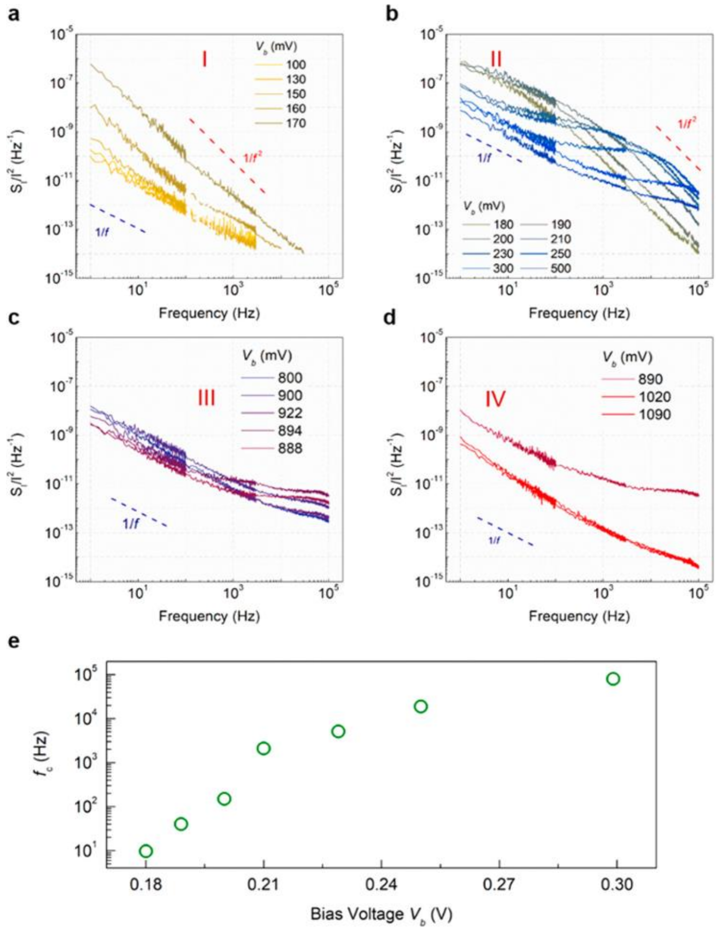

Figure 1-5 [36]: (a)-(d) low frequency noise spectra under different bias. (a). Low bias range. Slope change from -1 to -2, indicating the formation of Lorentzian noise. The corner frequency now is very low so only the tail of Lorentzian noise is observed. (b). The sliding of corner frequency as bias increases. (c). The slope at low frequencies turns back to -1 and flat spectra because of Lorentzian noise at higher frequency side. (d)Lorentzian noise corner frequency increase to higher frequency and only $1/f$ noise is measured. (e). Corner frequency sliding of Lorentzian noise for all bias ranges.

1.3. Shot Noise

Shot noise is a consequence of the quantized charge, and it provides extra information from normal conductance measurement [18,37–40]. Electronic shot noise was first discovered by Walter Schottky in the study of current fluctuation in vacuum tube in 1918 [41]. Unlike thermal noise which comes from thermal fluctuation, shot noise needs driving current to make electrons move. If you observe one point in a system with sufficient time resolution and count the electron arrival, the current is not continuous as water flow, but rather a discrete chain of events. If electrons' movements are not affected by other electrons, and their arrival time to the point you observe are independent to each other, the arrival time intervals in this situation are described by Poisson distribution and the corresponding noise is Poissonian noise or classic shot noise. The whole time series can be regarded as a sum of discrete δ functions with integral of each peak equal to a single charge carrier q, one example is shown in Figure 1-6 below.

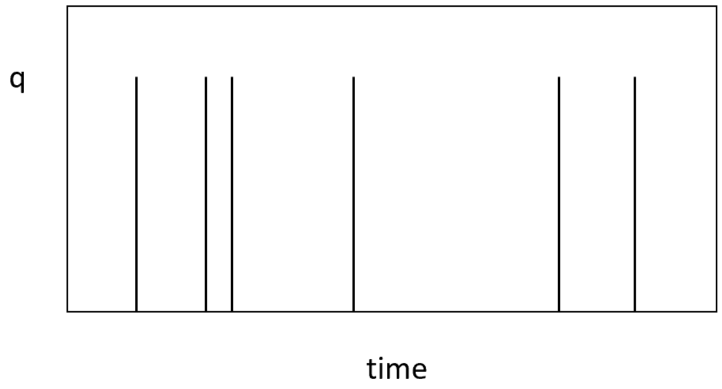

Figure 1-6: Example of discrete pulse time series because of the arrivals of quantized charge. Each pulse represents a carrier arrival with charge q, in other word each pulse is a δ function with integral equals q.

Here I briefly introduce the way to derive the shot noise formula based on the assumption above. Let $x(t)$ be the time series formed by the random pulses, and note that $x(t)$ is composed with many δ functions. If we suppose there N pulses detected from time $t = 0$ to $t = T$ distributed at $t = t_1, t_2, t_3, \ldots. t_N$. Then $x(t)$ during time T can be expressed as:

$$x(t) = \sum_{i=1}^{N} q\delta(t - t_i) \tag{1-7}$$

The autocorrelation function of this time series can be expressed as

$$R(\tau) = \frac{1}{T}\int_0^T x(t)x(t-\tau)dt = \frac{q^2}{T}\sum_{i=1}^{N}\sum_{j=1}^{N}\int_0^T \delta(t-t_i)\delta(t-\tau-t_j)dt \qquad \text{1-8}$$

The independent random arrival property decides that the autocorrelation function $R(\tau \neq 0) = 0$ (this also can be obtained from more detailed calculation). When $\tau = 0$, equation above becomes:

$$R(0) = \frac{q^2}{T}\sum_{i=1}^{N}\sum_{j=1}^{N}\int_0^T \delta(t-t_i)\delta(t-t_j)dt = \frac{q^2N}{T}\delta(0) \qquad \text{1-9}$$

Therefore $R(\tau) = \frac{q^2N}{T}\delta(\tau)$. The spectrum in the frequency domain can be obtained from Fourier transform:

$$s(f) = \int_{-\infty}^{+\infty} R(\tau)e^{-i2\pi f\tau}d\tau = \frac{q^2N}{T}\int_{-\infty}^{+\infty}\delta(\tau)e^{-i2\pi f\tau}d\tau = \frac{q^2N}{T} \qquad \text{1-10}$$

qN is the total charge passed during time interval T, so the current $I = qN/T$. Then we get $S(f) = qI$. Considering $S(-f) = S(f)$ and in the real world we actually measure the summation of positive frequency and negative frequency, we finally got the shot noise formula $S(f) = 2qI$, when the charge carrier is electron, $S(f) = 2eI$, and this is the most common form of the classic shot noise formula.

To observe shot noise, special systems are required. The shot noise discovered by Walter Schottky in 1918 is classical shot noise and can be fully explained by the statistical method above. Recent research of shot noise found in mesoscopic conductors, like tunnel junctions, quantum point contacts and so on, originate from scattering of electrons, and detailed derivations can be found in [37,42,43]. Here I summarize the final results for shot noise formulas, in a two terminal tunneling conductor(see diagram in Figure 1-7) with resistance R, assuming ideal one dimension tunneling model:

$$S_I = \frac{2}{R}\int \left[f_r(E)\big(1-f_l(E)\big) + f_l(E)\big(1-f_r(E)\big)\right] dE = 2eIcoth\left(\frac{eV}{2k_BT}\right) \qquad \text{1-11}$$

Here $f_r(E)$ and $f_l(E)$ represent the Fermi-Dirac distribution in the left and right electrodes, $f_r(E)\big(1-f_l(E)\big)$ stands for the tunneling from right side to left side and $f_l(E)\big(1-f_r(E)\big)$ is the tunneling from left to right, k_B is Boltzmann constant, T is temperature, I is current and e is the electron charge. Looking at the formula above, we can find two interesting properties, first, as $V \to 0$, $2eIcoth\left(\frac{eV}{2k_BT}\right) \to \frac{4k_BTI}{V} = 4k_BTG$, which means the noise signal in the low bias limit is actually the thermal noise where G is the conductance, and this is consistent with the fact that shot noise need driving current ; second, when $\frac{eV}{2k_BT} \gg 1$, $coth\left(\frac{eV}{2k_BT}\right) \to 1$, and $2eIcoth\left(\frac{eV}{2k_BT}\right) \to 2eI$, it becomes the classic shot noise and only related to the current and charge carrier. The formula above assumes that the tunneling probability in all channels are close to zero, if it is not, the shot noise formula at finite bias and temperature would be [37,42]

$$S_I = F\left(2eIcoth\left(\frac{eV}{2k_BT}\right) - 4k_BTG\right) + 4k_BTG \qquad \text{1-12}$$

where F is called Fano Factor. F is related to device geometry, material properties, effective charge and so on. In the two terminal tunneling model above, the Fano factor F is decided by the transmission probability T_n of all channels as $F = \frac{\sum_n T_n(1-T_n)}{\sum_n T_n}$, when $T_n \to 0$, $F = \frac{\sum_n T_n(1-T_n)}{\sum_n T_n} \approx 1$. When $T_n \to 1$, $F = \frac{\sum_n T_n(1-T_n)}{\sum_n T_n} \approx 0$. An diagram of shot noise with Fano factor F equals 1 is shown below [44]:

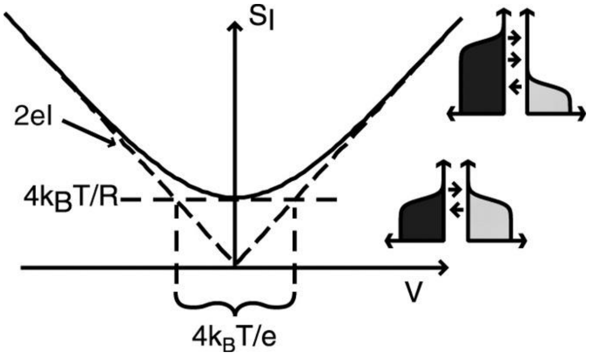

Figure 1-7 [44]. Expected shot noise of a tunnel junction as a function of bias voltage at finite temperature. Inserted black/gray diagram on right sides represent the Fermi Dirac distribution at nonzero and zero bias on two sides of tunnel junction. The shot noise at zero bias equals thermal noise, and the system need to be driven out of equilibrium ($eV \gg k_BT$) to obeserve shot noise.

Although sometimes shot noise also causes an undesired decrease of the signal to noise ratio like thermal noise and $1/f$ noise, shot noise at the same time provides extra information that is challenging to obtain from usual transport measurement [37,42,44,45]. One of the most famous applications of shot noise is to study the effective charge of current-carrying excitations [45–56], and these works were done in different systems like fractional quantum Hall devices [49,53–56], Josephson junctions [50], superconductors [45,51,52]. The structure of the devices also varies from planal tunnel junction [45], to scanning tunnel microscope(STM) junctions [52], to quantum point contacts [57], and to edge channels [49]. The earliest theoretical prediction of fractional charged carriers is proposed by Laughlin [58,59], in order to explain the fractional quantum Hall effect [60] which was observed in two-dimensional electron gas subjected to strong perpendicular magnetic field. The theoretical works that use shot noise to study fractional charge were authored by C.L. Kane in 1994 [46] and P. Fendley in 1995 [61]. The first experiments that directly observe of effective charge $e^* = \frac{e}{3}$ were done by R. de-Picciotto in 1997 [53], and almost simultaneously by L. Saminndayar [54]. Here I introduce R. de-Picciotto's work to show how shot noise decides the effective charge.

The authors measured back scattered current noise from a quantum point contact in two-dimensional electron gas (2DEG). The 2DEG is embedded in a GaAs-AlGaAs heterostructure, and the quantum point contact is formed by two metallic gates evaporated on the surface of the structure. The current quantum shot noise for a non-interacting single one-dimensional channel is given by:

$$S_I = 2g_0t(1-t)\left[QVcoth\left(\frac{QV}{2k_BT}\right) - 2k_BT\right] + 4k_BTg_0t \qquad \text{1-13}$$

Where $g_0 = e^2/h$, Q is effective charge, V is applied voltage, T is temperature and t is transmission probability. The key finding is shown in the Figure 1-8 [53] below.

The measured quantum shot noise value is much smaller than classic shot noise and very close to shot noise with F = 1/3 and hence effective charge equals $e/3$. This experiment unambiguously supports the existence of fractional charge in the fractional quantum Hall system.

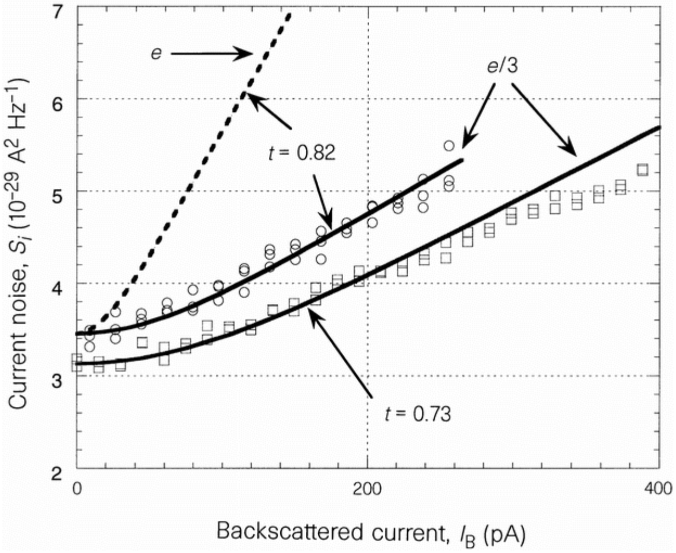

Figure 1-8 [53]. Quantum shot noise as a function of backscattered current I_B in the fractional quantum Hall regime at v=1/3, for two different transmission coefficients t. Solid and dashed lines are plots using formula above corresponding to different effective charge.

1.4. Shot noise in nanowires

Here I introduce shot noise in nanowires since this is directly related to my work. People have done detailed research in Fermi gas and Fermi liquid nanowires in both theory and experiment sides. Here I first show the theoretical conclusions of the relation between Fano factor and length of the wire. We start with Fermi gas expectations.

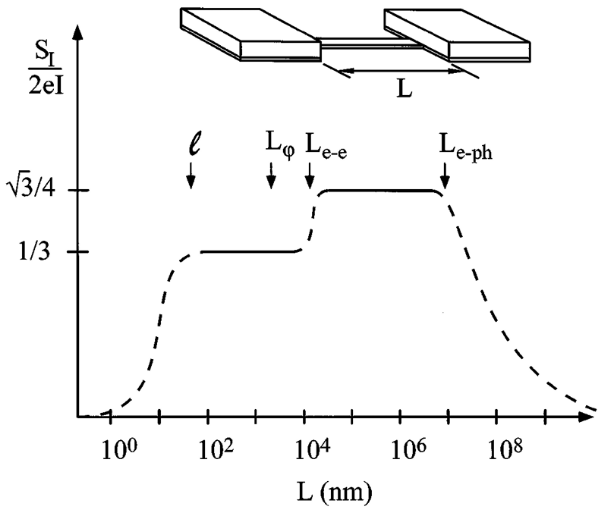

Figure 1-9 [62]. Theoretical predictions of current noise intensity $S_I/2eI$ versus nanowire length L when $eV \gg k_BT$.

In the diagram above, we can see four different expected F values as nanowire length changes. Let's first look at the first range where $L < l$, l is the electron elastic mean free path(around 100 nm in this figure). When the nanowire device length is much shorter than the elastic mean free path, the electrons transport from one contact to another is ballistic, and the shot noise would vanish, and this is equivalent to transmission coefficient $t \sim 1$ in Equation 1-13. In the second range $l \ll L \ll L_{\varphi}$, Fano factor equals to 1/3 [63,64], where L_{φ} is the electron phase breaking length. In other word, when nanowire device length $L \ll L_{\varphi}$, electron transport from one contact to another remains phase coherent, which is necessary for one of theoretical works which predict Fano factor F = 1/3 shot noise in diffusive nanowire as we will see later. In the third range $L_{\varphi} \ll L \ll L_{e-ph}$, Fano factor is predicted to be $\sqrt{3}/4$, where L_{e-ph} is the electron-phonon scattering length. In this range, the electrons undergo electron-electron inelastic scattering and thermalize their energy via the electron-electron interaction. The electronic thermal conductor along the wire transfer the energy to two contacts where thermal conductivity is decided by the Wiedemann-Franz law, and the result is a local temperature profile $T_e(x)$ along the nanowire. The direct calculation of Johnson noise based on $T_e(x)$ gives $S_I = 2k_BT/R[1 + (v + 1/v)\tan^{-1} v]$, where $v = \sqrt{3}eV/2\pi k_BT$. For $eV \gg k_BT$, $S_I = (\sqrt{4}/3)2eI$ [62,65,66]. Since the shot noise signal in this range comes from increased temperature of electrons, this is also called hot electron noise. In the fourth range $L \gg L_{e-ph}$, the nanowire is long enough so that the heat generated in wire is directly removed by phonons as well as transfer to the two contacts following the Wiedemann-Franz law. The Fano factor decreases to zero as nanowire length increases sufficiently [67]. It is worth pointing out that part of description in some references has been revised. For example in Andrew H. Steinbach 1996 [62], the claims in fourth range where $L \gg L_{e-ph}$ that the noise is $S_I = 4k_BT/R$, independent of I, and thus the nanowire displays no shot noise as commonly expected, but this was corrected later by M. Henny's work in 1997 [68] showing that when $L \gg L_{e-ph}$, the electron temperature T_e and phonon temperature T_{ph} are not exactly same, and $T_e \propto I^{2/5}$ when $T_e \gg T_{ph}$, and T_e is related to electron-phonon coupling parameter which can be obtained from additional noise measurement. To help the reader understand the shot noise in nanowires better, I will spend several paragraphs discussing the theory and experimental results for th second ($F = 1/3$), third ($F = \sqrt{3}/4$) and fourth ($F \to 0$) length.

1.4.1. F = 1/3 shot noise in nanowire

The prediction of F = 1/3 shot noise in diffusive metal nanowire is ubiquitous, and there are actually two main theories that reached same conclusion. The first is proposed by Beenakker and Buttiker in 1992 [64]. In their theoretical paper, they claim shot noise in a disordered phase-coherent conductor, much longer than the mean free path, but much shorter than an inelastic scattering length, is one third of the classic value of a Poisson process, and this reduction is caused by noiseless open quantum channels. Start from the Landauer-Buttiker approach to conductor for a phase-coherent regime [69]:

$$S = 2eV\frac{e^2}{h}\mathrm{Tr}\,\boldsymbol{tt}^{\dagger}(1-\boldsymbol{tt}^{\dagger}) = 2eV\frac{e^2}{h}\sum T_n(1-T_n) \tag{1-14}$$

Here $\boldsymbol{tt}^{\dagger}$ is N by N transmission matrix and T_n are eigenvalues of transmission matrix. They consider the case that device length L is much longer than mean free path l but much smaller than localization length Nl. Their calculation applies a result from random matrix theory of quantum transport, and use the concept of channel dependent localization length ζ_n related to the transmission eigenvalues by $T_n = \cosh^{-2}(L/\zeta_n)$. Under assumption that the inverse localization length is uniformly distributed between 0 and $1/\zeta_{min}$, for arbitrary function $f(T)$ that vanishes for $T \ll 1$, we have:

$$\frac{< \sum_{n=1}^{N} f(T_n) >}{< \sum_{n=1}^{N} T_n >} = \int_0^\infty f(\cosh^{-2} x) dx \tag{1-15}$$

Where < > represent expected values. With eh equation above, one can evaluate the ratio of different order transmission matrix trace values as $C_p = \frac{<\mathrm{Tr}(\boldsymbol{tt}^\dagger)^p>}{<\mathrm{Tr}\,\boldsymbol{tt}^\dagger>}$, $p = 1,2, \ldots$ Using $f(T) = T^2$ for the equation above, we find $C_2 = \frac{\Gamma(\frac{1}{2})\Gamma(2)}{2\Gamma(2+\frac{1}{2})} = \frac{2}{3}$. This implies that:

$$< S > = 2eV\frac{e^2}{h} < Tr\, \boldsymbol{tt}^\dagger > \left(1 - \frac{2}{3}\right) = \frac{2}{3} eV < G > \tag{1-16}$$

This equation means that the Fano factor is 1/3. The author claims that the reduction of shot noise in a diffusive wire is the result of quantum interference. It comes from the bimodal distribution of transmission eigenvalues, such that a fraction of l/L of eigenvalues is close to 1 and the remainder are exponentially small, close to 0.

Another theory that gives Fano factor 1/3 is proposed by Nagaev also in 1992 [63]. Unlike Beenakker and Buttiker's method, which requires phase coherent transport and quantum interference, Nagaev's theory is semiclassical and does not require phase coherent transport. Nagaev's theory starts from a kinetic equation for the electron occupation probability $f(E,x)$, and current noise S_I is derived showing that it is proportional to the fluctuations of occupation number $f(1-f)$ that:

$$S_I = 4G\,\langle \int_{-\infty}^{\infty} f(E,x)[1-f(E,x)]dE \rangle \qquad \text{1-17}$$

where G is conductance and x is the position along the wire. According to Nagaev's theory, one can introduce the contribution of the electron-electron scattering integral I_{ee} and the electron-phonon scattering integral I_{ph} into the diffusion equation:

$$D\frac{d^2}{dx^2}f(E,x) + I_{ee}(E,x) + I_{ph}(E,x) = 0 \qquad \text{1-18}$$

Hhere D is the electron diffusion coefficient [66]. In the range $l \ll L \ll L_{ee}$, where L_{ee} is electron-electron scattering length, $I_{ee}(E,x) \approx I_{ph}(E,x) \approx 0$, then we get $\frac{d^2}{dx^2}f(E,x) = 0$, or $\frac{d}{dx}f(E,x)$ equals a constant value. So for same energy E, $f(E,x)$ linearly increases/decreases from one end of wire to the other end. To solve the diffusion equation, we also need two boundary conditions. Assuming two ideal contacts at the two ends, $f(E,x)$ is given by Fermi-Dirac distributions by $f(E,0) = 1/[\exp(\frac{E}{k_BT}) + 1]$ at left end and $f(E,L) = 1/[\exp(\frac{E-eV}{k_BT}) + 1]$ at right end. Then we can solve $f(E,x)$ easily:

$$f(E,x) = \frac{L-x}{L}f(E,0) + \frac{x}{L}f(E,L) \qquad \text{1-19}$$

Putting $f(E,x)$ into the noise integration equation, one obtains:

$$S_I = \frac{2}{3}\left[\frac{4k_BT}{R} + \frac{eV}{R}\coth\left(\frac{eV}{2k_BT}\right)\right] \qquad 1\text{-}20$$

The equation above is the quantum shot noise with Fano factor equals 1/3. Based on these theoretical predictions, there were several experimental results published in the following years. The first work about the 1/3 shot noise in nanowire is reported in 1994 done by F. Liefrink et al [70]. The experiment was in a two-dimensional electron gas system, and the nanowire is formed by applying a gate voltage on two sides of a split-safe structure. By changing the gate voltage, the authors can adjust the electron density, nanowire width, mean free path and inelastic scattering length. The result is shown in Figure 1-10 below:

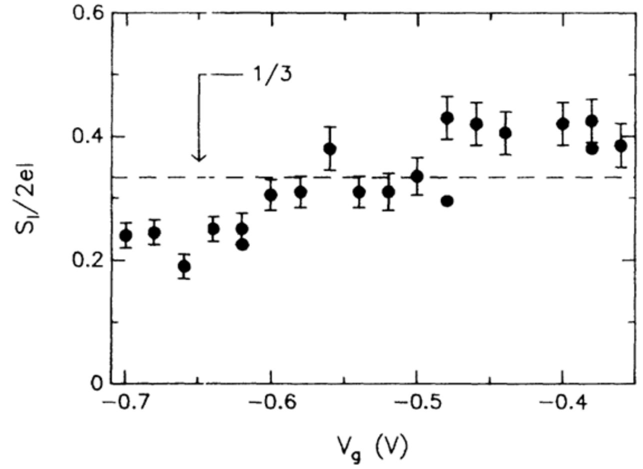

Figure 1-10 [70]. Fano factors dependence on gate voltage at $T = 4.2$K. Dashed line indicates the expected value from theory.

The results vary from 0.2 to 0.45 in this experiment, not far from 1/3. It is worth pointing out that the authors claim that the wire length is longer than electron coherence length in the device, so coherent transport maybe is not necessary for this reduced shot noise. Two years later, R.J Schoelkopf et al measured shot noise in a nanowire at very high frequency(1-20 GHz), and differential noise dS_I/dI is close to $2/3e$, but the total shot noise curve is not shown [71]. In 1998, M. Henny et al did very careful analysis of experimental design and considered the effects of the contact reservoirs. By making the two reservoirs more closer to ideal heat sinks, he fabricated nanowire devices with better well-defined Fermi-Dirac distributions at the two ends, and observed 1/3 shot noise at last [72]. The main result is shown in Figure 1-11 below:

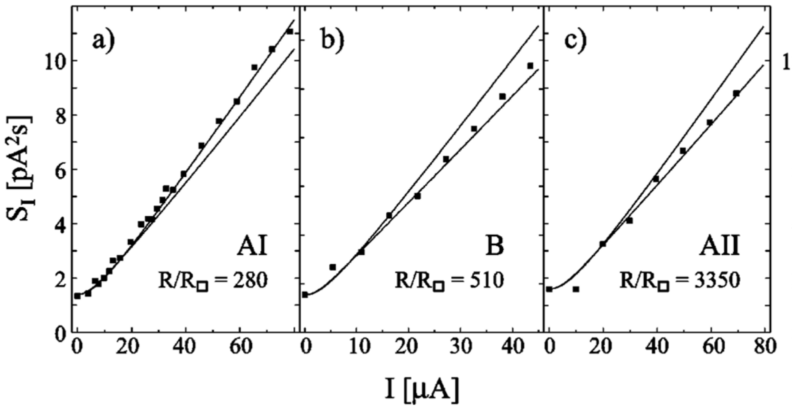

Figure 1-11 [72]. Shot noise measurements of three different samples with different $R/R_{\blacksquare}$ ratio at T=0.3K, where R is the resistance of wire and $R_{\blacksquare}$ is the resistance of contact reservoirs. The upper and lower line corresponds to predictions of $L \gg L_{ee}$ $(F = \sqrt{3}/4)$ and $L \ll L_{ee}(F = 1/3)$ respectively. The result shows that the reservoirs are significantly heated when the $R/R_{\blacksquare}$ ratio is not large enough.

1.4.2. F = √3/4 shot noise in nanowire

In the previous subsection, I introduce the case where $l \ll L \ll L_{ee}$, here I focus on the situation when $L_{ee} \ll L \ll L_{e-ph}$. There were two theoretical works published in 1995 by Kozub [65] and Nagaev [66]. Both papers concluded that $S_I = \frac{\sqrt{3}}{2}\frac{eV}{R}$ when $eV \gg k_B T$, and the derivations are similar. When $L_{ee} \ll L$, the electron-electron scattering is strong that carriers exchange energy effectively with each other, and reach thermodynamic equilibrium locally; therefore, the occupation probability $f(E,x)$ can be described by a local Fermi-Dirac distribution with a local temperature $T_e(x)$ higher than the phonon temperature and a local chemical potential $\mu(x) = (x/L)eV$ as:

$$f(E,x) = \frac{1}{e^{[E-\mu(x)]/k_B T_e(x)} + 1} \qquad \text{1-21}$$

Now we can compare the electron distribution function between $L \ll L_{ee}$ case and $L \gg L_{ee}$ case based on Nagaev's theory. The result is shown in Figure 1-12

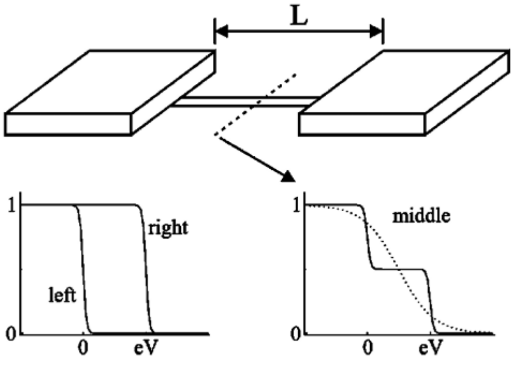

Figure 1-12 [72]. Electron distribution of a nanowire connected to two large reservoirs. The distributions at the two ends are Fermi-Dirac distributions with a chemical potential difference eV. When $L \ll L_{ee}$, electron distribution inside the wire is a linear combination of the two distributions at the two ends, so it forms a two-step function. If we look at the position exactly in the middle, the step is at 0.5, and the step will move up/down as the position moves to right/left. When $L \gg L_{ee}$, the distribution is Fermi-Dirac everywhere, but the local temperature is higher in the middle, so the Fermi-Dirac distribution is less sharp.

Recall the Nagaev's diffusion function in last subsection, we ignore phonon effects and only consider the electron-electron scattering integral I_{ee}.

$$I_{ee}(\epsilon) = -\frac{\pi^2}{64}\epsilon_F^{-1}\frac{k}{p_F}\int_{-\infty}^{\infty} d\epsilon' \int_{-\infty}^{\infty} d\omega\{f(\epsilon)f(\epsilon'-\omega)[1-f(\epsilon-\omega)][1 - f(\epsilon')] - f(\epsilon-\omega)f(\epsilon')[1-f(\epsilon)][1-f(\epsilon'-\omega)]\} \quad \text{1-22}$$

Using the Fermi-Dirac distributions for the density functions above, the diffusion function becomes:

$$\frac{d^2T_e^2}{dx^2} = -\frac{6}{\pi^2}\left(\frac{eV}{k_B L}\right)^2 \quad \text{1-23}$$

The same conclusion would be obtained if we use local Joule heating and the Wiedemann-Franz law to construct the temperature profile $T_e(x)$. To easily understand this, the equation above can be rewritten as $\frac{L_0}{2}\frac{d^2T_e^2}{dx^2} = -\left(\frac{V}{L}\right)^2$, where $L_0 = \frac{\pi^2}{3}\frac{k_B^2}{e^2}$ is the Lorenz number. Then it is easy to see that the left side is heat a diffusion equation decided by the electron thermal conductivity and right side is Joule heating.

Solving the equation above yields a temperature profile:

$$T_e(x) = \sqrt{T^2 + \frac{x}{L}\left(1 - \frac{x}{L}\right)\frac{V^2}{L_0}} \tag{1-24}$$

The integral of J-N noise along the wire gives $S_I = 2k_BT/R[1 + (v + 1/v)\tan^{-1} v]$, where $v = \sqrt{3}eV/2\pi k_BT$. For $eV \gg k_BT$, $S_I = (\sqrt{4}/3)2eI$.

The first experimental work that focuses on the electron heating effects by was done Steinbach et al [62] in next year(1996) after the theoretical results. They measured noise signals in different lengths (1μm to 7mm) of silver thin film resistors at low temperature, and part of the results are shown below:

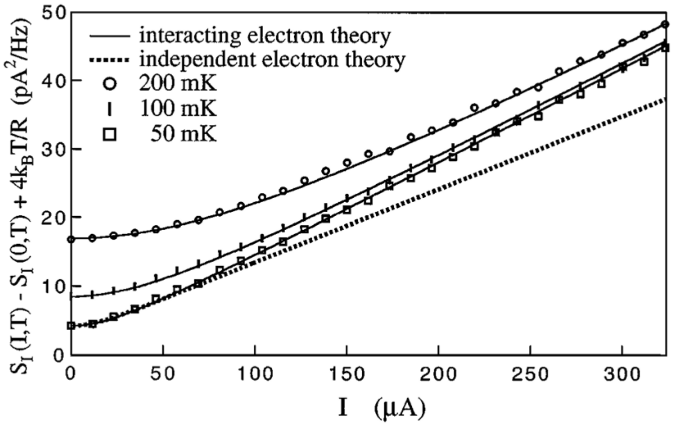

Figure 1-13 [62]. Noise signal dependence on current I for a 30 μm long device at 50, 100, and 200 mK. Solid and dashed lines represent theoretical predictions of strong electron-electron interaction(50, 100 and 200 mK) and independent electron(50 mK) cases respectively. The experiment data show great agreement with interacting electron theory.

1.4.3. Phonon effects on shot noise in nanowires

In this subsection, I briefly discuss the phonon influence on the shot noise signal. Phonons are the vibration modes of the sample and do not produce the electrical noise signal directly. Phonons affect the conductivity and noise through scattering with conductor electrons. In term of noise signal, phonons can have two effects: 1. Produce $1/f$ noise in low frequency [73]. 2.Supress the noise signal by absorbing energy from hot electrons. In this thesis, we focus on second effect. The initial theoretical work was developed by Nagaev in 1995 [66], where he covers both the effect of electron-electron scattering and electron-phonon scattering. Here I jump to the final diffusion function including the phonon effects:

$$\frac{L_0}{2}\frac{d^2T_e^2}{dx^2} = -\left(\frac{V}{L}\right)^2 + \Gamma\left(\frac{k_B}{e}\right)^2 (T_e^5 - T^5) \tag{1-25}$$

Here $L_0 = \frac{\pi^2}{3}\frac{k_B^2}{e^2}$ is the Lorenz number, and Γ is a phenomenological electron-phonon scattering strength parameter. The item on the left is heat diffusion decided by the Wiedemann-Franz law, the first item on the right is related to Joule heating, and the last item accounts for energy transfer from hot electrons to phonons. When $L \gg L_{e-ph}$, the heat transfer along the wire to the two reservoirs can be ignored, the temperature profile would be dominated by electron-phonon scattering. The local electron temperature becomes almost constant along the wire and:

$$T_e = \left(T_{e-ph}^5 + \frac{1}{\Gamma}\left(\frac{eV}{k_B L}\right)^2\right)^{\frac{1}{5}} \tag{1-26}$$

And the noise intensity is given by:

$$S_I = \frac{4k_B}{R}\left(T_{e-ph}^5 + \frac{1}{\Gamma}\left(\frac{eV}{k_B L}\right)^2\right)^{\frac{1}{5}} \tag{1-27}$$

Steinbach et al's work in 1996 [62] shows data consistent with the equation above, and Henny et al did more detailed work in 1997 [68]. Here I show part of Henny's results below in Figure 1-14. It is worth noting that when the wire is 50 μm long, the temperature for the most of the wire is constant and the profile $T_e(x)$ is flat. The electron-phonon scattering strength parameter can be estimated using the noise measurement as a function of bias. Henny got $\Gamma \approx 5 \times 10^9\ \mathrm{K^{-3}m^{-2}}$ for his gold nanowires.

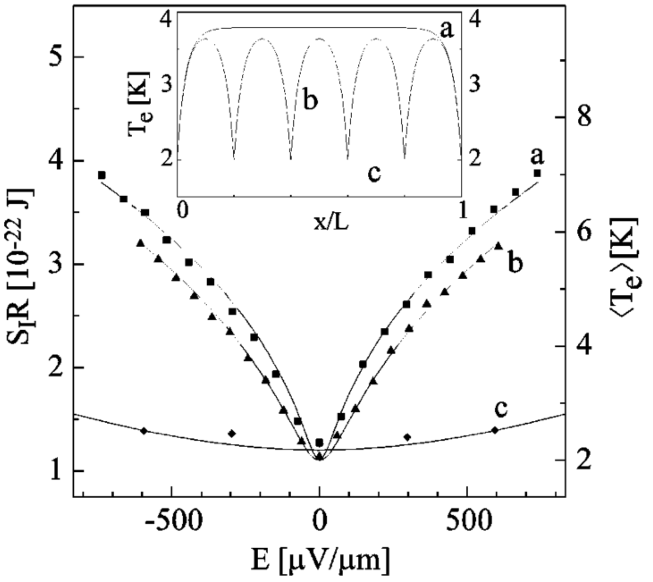

Figure 1-14 [68]. Noise intensity versus electric field along the wire for three different length sample. Sample A is a 50 μm long Au wire, sample B has five 10 μm long wires in series, and sample C is made with 30 wires with a length if 0.84 μm. The inset shows the calculated temperature profile along the wire for the three samples.

Equation 1-25 will be discussed more in details in Chapter 6, and we add one item to correct the thermal conductivity change when the resistance varies with temperature. It is worth noting that the original theory description for shot noise in diffusive wire was based effectively on a Fermi gas. It was believed to extend to more correlated Fermi liquid with interaction corrections [74], but a full treatment has only very recently been done by our collaborators Yiming Wang et al [75]. Yiming Wang et al have examined the Fermi liquid case with strongly renormalized but not zero quasiparticles weight Z. They find that $F \to \sqrt{3}/4$ for this case, as all Landau parameters cancel and Z never appear in the noise calculation.

Chapter 2

Mott insulators

2.1. Mott insulators

In 1937, researchers, such as de Boer and Verwey, found that some metal oxides which are supposed to be metallic based on the band theory are actually insulators [76,77]. For example, NiO, which should be a metal because of a partially filled d-band according to band theory, actually turns into an insulator as temperature goes down. Sir Neville Mott among others considered the problem of how electron-electron interactions could lead to insulating properties in systems where simple electron counting would suggest a metallic state (electronic chemical potential in the middle of a band). Still taking NiO as an example, Mott modeled that electric conduction comes from the hopping of electrons from one site to another. When an electron is about to hop to a new site which is already occupied by an electron, it will be pushed back by the "on-site" Coulomb repulsion energy U. If the repulsion energy U is greater than the electron's kinetic energy t, the electron would not be able to hop to another site and would become localized in its original site, so the system will behave like an insulator.

In 1963 [78], Hubbard first proposed a simple model considering the Coulomb repulsion and hopping matrix element in a 1-D long chain. The Hamiltonian can be expressed as

$$H = -\sum_{i,j,\sigma}^{N} t_{ij}\left(c_{j\sigma}^{+}c_{k\sigma} + c_{j\sigma}c_{k\sigma}^{+}\right) + \sum_{i}^{N} U_{i}n_{i\sigma}n_{i,-\sigma} \qquad \text{2-1}$$

Where H is Hamiltonian, t_{ij} is hopping matrix element, $c_{j\sigma}^{+}$ is the creation operator of one electron in site j with spin σ, $c_{j\sigma}$ is the annihilation operator of one electron in site j with spin σ, U_i is Coulomb repulsion energy and $n_{i\sigma} = c_{j\sigma}^{+}c_{j\sigma}$ is the number operator on electron at site j. Figure 2.1 shows the diagram shows the 1-D chain diagram.

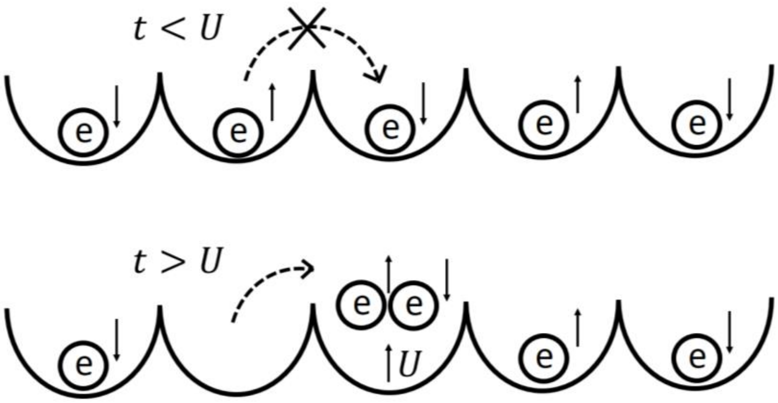

Figure 2-1: Diagram of electron hopping and repulsion from electron Coulomb interaction. When the electron kinetic energy is smaller than on-site repulsion energy, the electron will be localized.

When the Coulomb repulsion energy is much larger than electron hopping matrix element, the electron interaction will effectively split the original half-filled band into two bands. One is called upper Hubbard band and the other is called lower Hubbard band. The typical Mott-insulator Hubbard band structure is show in Figure 2.2. The left side is the band structure of a metal phase, where the *d*-band is half-filled, and there is energy gap $\Delta = |\varepsilon_d - \varepsilon_p|$ between *d*-band and *p*-band. When the system goes through the Mott metal-insulator phase transition, the *d*-band is split into two bands and separated by a charge gap because of the electron-electron repulsion energy *U*.

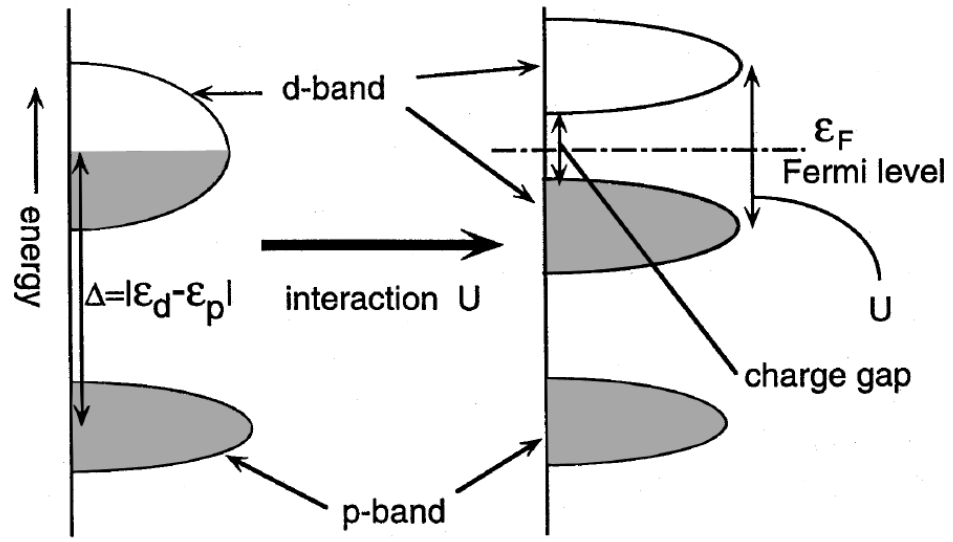

Figure 2-2 [79]: Typical Mott-insulator band structure. As electron-electron on-site interactions are "turned on", the system goes through a metal-insulator phase transition; the *d*-band is split into two bands separated by a charge gap because of the electron-electron repulsion energy U.

From the band structure shown above, we could find two ways to tune the metal-insulator transition. The first one is to increase the bandwidth of electron band. When the bandwidth is larger than the charge gap caused by electron interactions, the lower Hubbard band and upper Hubbard will overlap and form a single band with the Fermi energy lying in the middle, and the system will become metallic. One of the methods to increase the bandwidth is to increase the overlap of electron wave functions by compressing the material. The second method is to dope electrons (or holes). Doping can change the positon of Fermi surface, and if it moves from at the middle of upper Hubbard band and lower Hubbard band shown in the Figure 2.2, the resulting partial-filled upper band (electron doping) or lower band (hold doping) will turn the system into metallic state.

2.2. V_2O_3 phase transition

Metal-insulator transitions in metal oxides remain at the core of physics and draw much attention in past decades [80–84]. The emerging technologies such memories and neuromorphic computing [85] rely on the understanding of the fundamental mechanism of this phase transition. Vanadium sesquioxide (V_2O_3), as an archetypal material with strong electronic correlations, undergoes a rhombohedral paramagnetic metal to monoclinic antiferromagnetic insulator transition [86] when cooled below 160 K, with films showing a range of phase coexistence of ~30 K [87]. The resistance can increase by several orders of magnitude with cooling as antiferromagnetic insulating domains grow at the expense of paramagnetic metallic domains. The metal-insulator transition may be triggered by several stimuli: temperature [88], light [89,90], strain [91], pressure [91], and electric field [92]. Increased interest in such metal-insulator materials for neuromorphic computing [85] applications has emphasized the importance of understanding fluctuations in the transition both in and out of equilibrium. The structures of these two phases are shown in Figure 2.3. Each corner represents a vanadium atom, other vanadium and oxygen inside are omitted for clarity.

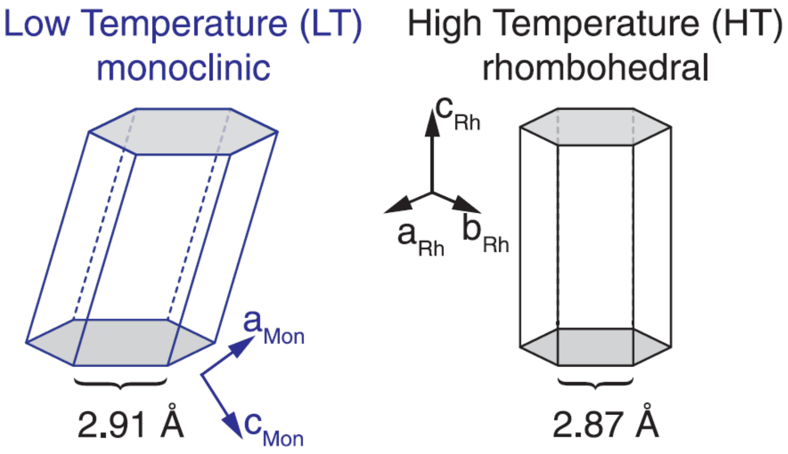

Figure 2-3 [93]: The monoclinic insulating and rhombohedral metallic structures of V_2O_3.

2.3. Percolation theory

Percolation theory is actually based on statistics and probability theory. It studies a network formed from a collection of points distributed in a space, where the points are randomly linked to each other, or the points' positions are randomly located, to form different linked clusters. The situation of points with fixed positions and random linkages is called "bond percolation"; the other situation where the points are randomly positioned and the linkage between each points follow a certain rule is called "site percolation". One of the earliest percolation problems was raised by Broadbent and Hammersley [94] who consider random linkage edges between vertices, where any pairs of vertices are linked with probability p.

When considering the size of a cluster in a percolation model, there is usually a percolation critical point (or percolation threshold). When the system goes beyond this critical point as a function of some control parameter (such as p), there is likely some giant cluster that spans the system; otherwise, it is statistically unlikely for the system to have a large cluster. The critical value of p required for percolation is dependent on the details of the model. For example, take the vertical percolation in a 2-D square lattice as an example. If each square has probability p to be a conductor, and probability $1-p$ to be an insulator, when the $p > p_c \approx 0.529$, it is very probable (essentially certain as system size becomes large) to find a conductive path from one side of the lattice to the other. On the other hand, if $p < p_c$, it is very unlikely (essentially no chance as system size becomes large) to find a conductive path from one side of the lattice to the other. So, when $p > p_c$ the system is metal, and when $p < p_c$, the system is insulator.

Unfortunately, there is still no exact analytical answer for this threshold, and this number is obtained by Monte Carlo simulation.

Percolation models are important in the real physics systems. For example, in 2015 [95], researchers studied the noise signal in VO_2 across its metal-insulator phase transition. In the coexistence regime of that phase transition, as in V_2O_3, the material breaks up into metallic and insulating domains. The metal-insulator transition can be regarded as proceeding through the change of fraction of each domain. So the resistance changes in a similar way to that mentioned above. Although the system is not a simple percolation model because the metal (insulator) domain tends to grow along the crystallographic c-axes, people still observed the percolative character in metal-insulator transition of VO_2. In classical lattice-percolation with a periodic lattice, when the system is sufficiently close to the percolation threshold, researchers claim there is scaling [96–98]

$$\frac{S_R}{R^2} \propto R^x \tag{2-2}$$

Where $\frac{S_R}{R^2}$ is normalized noise intensity, and x is noise scaling exponent related to the details of percolation model. People in VO_2 found this scaling effect (Figure 2.4) with $x \approx 2.6$, and it is explained by Pennetta–Trefan–Reggiani theory [99], which considers randomly switching defects in the lattice. Supposing a given lattice site has a failure probability to malfunction and becomes a defect and a healing probability for the defect to recover its original lattice resistance.

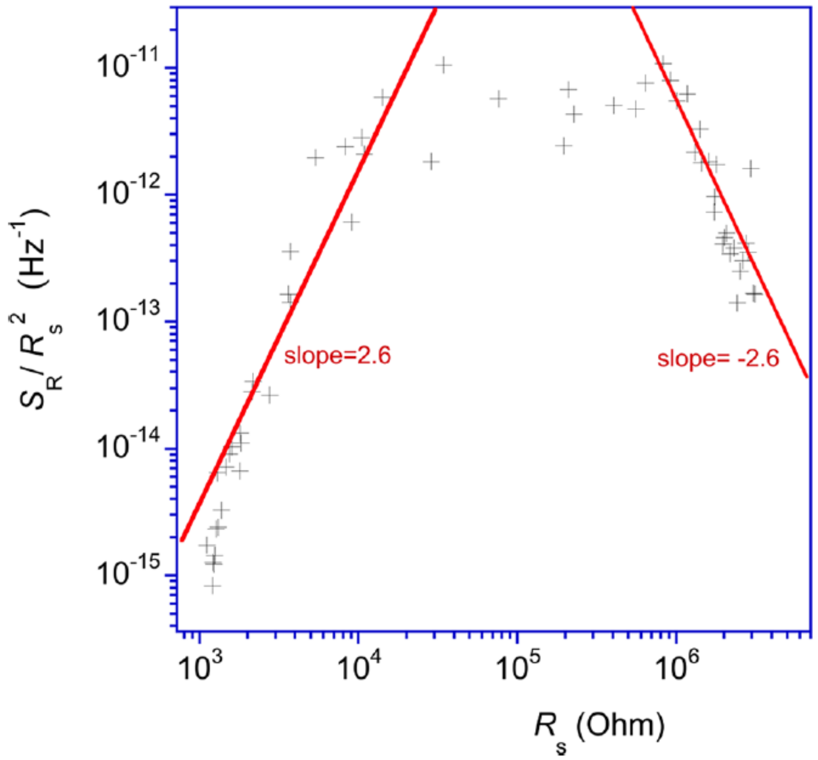

Figure 2-4 [95]: Normalized noise intensity versus sample resistance in log-log scale. It shows percolation noise scaling exponent around 2.6 at two side of threshold.

In scaling models of percolation, the resistance noise not only may come from the fluctuation of resistance of each region, but also may come from the fluctuation of volume of each fraction. In 1993, L.B. Kiss and P. Svedlindh [100] created a model to explain why the noise scaling factor in high temperature superconductor film is close to 1.5 rather than the predicted 1.3 by the classic percolation model. In this model, the noise results from fluctuations that switch off or on connections between conducting regions rather than changes in the resistance of the conducting regions themselves. The value of noise scaling factor is related to the resistance scaling factor s by $x = 2/s$. The relation can be expressed as [100]

$$R \propto (p - p_c)^s, \qquad \frac{S_R}{R^2} \propto R^x, \quad x = 2/s \tag{2-3}$$

where p is the fraction of insulating part and p_c is the threshold. The noise in this model comes from the random switching of the metal state and insulator state of each region, and people call this type noise "p-noise". In this case, the noise scaling factor is related to the dimension of system. x is predicted to be 2.7 for 3D, 1.5 for 2D and 2 for 1D.

Chapter 3

Strange Metal

Fermi liquid theory, also known as Landau's Fermi liquid theory, was firstly introduced to explain the behavior of ^{3}He in 1959 [101], and it was later used to explain the properties of normal metals with weak electron-electron interactions. It successfully explained important features of normal metals such as T^2 dependence resistivity and T dependence specific heat at low temperature, and became the cornerstone in dealing with many body interactions for past 70 years. However, in past decades, more and more metallic systems were found that violate this paradigm. The most evident violation is the electric resistivity dependence on temperature. In normal metal, resistivity increases with increasing temperature but saturate at both low temperature and high temperature side. But in strange metal, there is no saturation at either low temperature side, or high temperature side, or both. In this Chapter, I would give brief introductions from Fermi gas to strange metal.

3.1. Fermi Gas

Our basic understanding of electrons movement in metal starts from non-interacting electrons. In a metal with high density of free electrons, the screening effect [102] will be strong and screening length would be short, this means that the electrons feel less the Coulomb repulsion force from other electrons. This is true although it sounds counterintuitive.

In a three dimensional lattice with periodic boundary condition, the solution of single electron Schrodinger equation yields the electrons wave functions for non-interacting Fermi gas as:

$$\psi_k(r) = \frac{1}{\sqrt{V}} e^{i\vec{k}\cdot\vec{r}}, where\ \vec{k} = \frac{2\pi n_x}{L_x}\vec{x} + \frac{2\pi n_y}{L_y}\vec{y} + \frac{2\pi n_z}{L_z}\vec{z} \qquad 3\text{-}1$$

Where L_x, L_y, and L_z are size of lattice, V is the volume of lattice, and $\vec{x}$, $\vec{y}$, and $\vec{z}$ are unit vectors in three directions. The energy of each eigenstate $\epsilon_k = \frac{\hbar^2 k^2}{2m}$. In the low temperature limit, electrons tend to occupy the low energy eigenstates with small k values. Because of Pauli Exclusion principle, each eigenstate can have only two electrons with spin up and spin down. This results in a sphere in momentum space, where all states inside are occupied by electrons and all states outside are empty at zero temperature limit. This diagram is shown in Figure 3-1 [103] below. This sphere is called Fermi surface, the electron energy at the Fermi surface is called Fermi energy and the corresponding k is called Fermi wavevector.

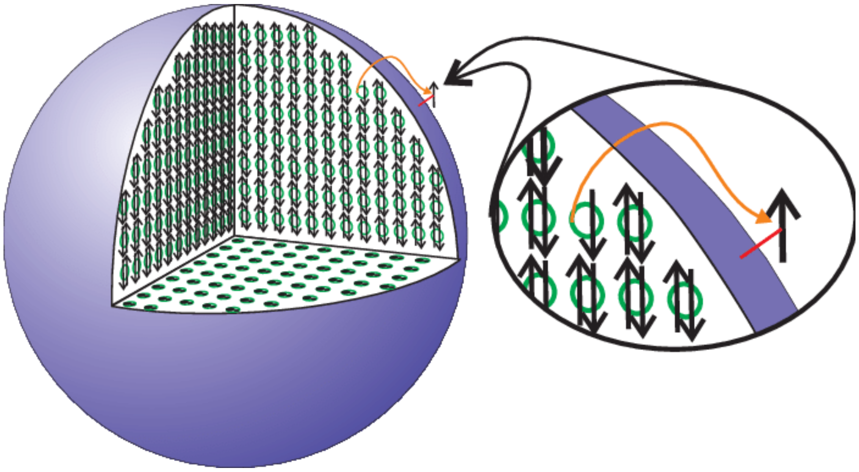

Figure 3-1 [103]. Ground state of three dimensional Fermi gas in momentum space. The low energy states (green circles) inside Fermi surface (purple sphere) are occupied by two spin electrons (up arrow and down arrow). One electron close to Fermi surface is excited and leaves a hole in original state.

At finite temperature, the electrons close to Fermi surface can be thermally excited to higher energy states (outside of the Fermi surface), and form electron-hole pairs with the holes in their original positions. These excited electrons ideally have infinitely long lifetime if they do not scatter with other electrons, and their excitation spectra would be delta functions. Since electrons are fermions, they obey the statistical law of Fermi-Dirac distribution that gives the occupation function f at given temperature T and chemical potential μ as:

$$f(\epsilon) = \frac{1}{e^{\frac{\epsilon-\mu}{kT}} + 1} \tag{3-2}$$

Using the Fermi-Dirac distribution, energy density of state (can be obtained from electron wave function), and necessary approximation, people can calculate the electrons' total energy at low temperature limit and partial differential of total energy yield specific heat $C_V \propto T$. This prediction from Fermi gas theory works well with real metal. In 1936, Landau and Pomeranchuk [104] found that at sufficiently low temperature, the electron-electron scattering can lead to T-square resistivity, and same theory result is proposed by Baber in 1937 [105]. These T-square resistivity and linear in T specific heat C_V extend to Fermi liquid as shown in section 3.2. Interestingly, the origin of T-square resistivity has recently been challenged by experiments in $SrTiO_3$ [106] and dilute metallic Bi_2O_2Se [107].

3.2. Fermi Liquid

Fermi liquid has been regarded as the standard model in explaining metal properties since its invention in 1960s [101]. It successfully deals with the electron-electron interactions, and preserves the T-square resistivity and linear in T specific heat C_V in metals. The basic idea of Fermi liquid theory is the "quasiparticle", an electron like excitation with effective mass modified by interactions with other electrons or lattice, some of the materials have very large effective mass are called heavy fermions, such as $YbRh_2Si_2$, the material we focused on in this thesis.

Fermi liquid theory starts from Fermi gas, and then slowly turn on the interactions. Landau assumes the original non-interacting states will smoothly and continuously evolve into interacting states. Take ^{3}He as an example. ^{3}He have two neutrons, one proton and two electrons, so the atom is a fermion. When the ^{3}He is in high temperature gas state, a negligible interaction between these fermions would be expected, and the whole system is Fermi gas. If we turn on the interaction adiabatically, the ground states of Fermi gas should transform into ground state of the interacting system. In this process, the spin and charge remain unchanged, but the effective mass and magnetic moment will be renormalized into different values. The old excited single particle states of non-interacting Fermi gas are occupied by quasiparticles. These states are not exactly eigenstates in the new interacting system, but they can approximate the excited eigenstates for long time when the excitation is close to Fermi surface. These long-lived quasiparticle excitations near Fermi surface is the primary assumption of Fermi liquid theory.

People might have question about the adiabatic switching process reliability, because when the electron interactions excite the quasiparticle states, these states should decay exponentially following Fermi’s golden rule, and whether we have quasiparticles left after we slowly turning on the interaction is a question. On the other side, if we turn on the interaction too fast, the process would not be adiabatic and there would be no one-to-one corresponding quasiparticles states. According to Fermi liquid theory, the only excitation states that remain stable are the states close to Fermi surface. We could get basic understanding of the reason considering the scattering process. Suppose the system is close to temperature limit that almost all states below Fermi surface are occupied.

Consider one particle excited above the Fermi energy E_F with energy $\epsilon_1 > E_F$ and momentum $\mathbf{P}_1$, if it scatters with another particle below Fermi surface with energy $\epsilon_2 < E_F$ and momentum $\mathbf{P}_2$, the only result is two particles with energy $\epsilon_3 > E_F$ and $\epsilon_4 > E_F$, and the momentum are $\mathbf{P}_3$ and $\mathbf{P}_4$ respectively, because almost all states below Fermi surface are fully occupied, so the two particles after scattering must be above Fermi surface. The conservation of energy and momentum require that:

$$\epsilon_1 + \epsilon_2 = \epsilon_3 + \epsilon_4 \ \ and \ \ \mathbf{P}_1 + \mathbf{P}_2 = \mathbf{P}_3 + \mathbf{P}_4 \qquad 3\text{-}3$$

This process can be represented in below:

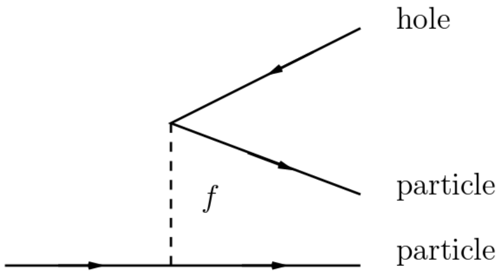

Figure 3-2 [108]. Feynman diagram showing the scattering process that starts with on particle and ends up with two particles and one hole.

Looking at the conservation constraints above, we notice that $\epsilon_1 + \epsilon_2 = \epsilon_3 + \epsilon_4 > 2E_F$, so $E_F > \epsilon_2 > E_F - (\epsilon_1 - E_F)$. Intuitively speaking, when ϵ_1 becomes closer to E_F, ϵ_2 would have less choices, and this means less scattering rate and longer lifetime according to Fermi's golden rule. If we take a more detailed look in momentum space, and rewrite the conservation constraints above as:

$$\mathbf{P}_1^2 + \mathbf{P}_2^2 = \mathbf{P}_3^2 + \mathbf{P}_4^2 \ \ and \ \ \mathbf{P}_1 + \mathbf{P}_2 = \mathbf{P}_3 + \mathbf{P}_4 \tag{3-4}$$

Because $\mathbf{P}_1^2 + \mathbf{P}_2^2 = \frac{(\mathbf{P}_1+\mathbf{P}_2)^2}{2} + \frac{(\mathbf{P}_1-\mathbf{P}_2)^2}{2}$ and $\mathbf{P}_3^2 + \mathbf{P}_4^2 = \frac{(\mathbf{P}_3+\mathbf{P}_4)^2}{2} + \frac{(\mathbf{P}_3-\mathbf{P}_4)^2}{2}$, the constraints above can be rewritten as:

$$(\mathbf{P}_1 - \mathbf{P}_2)^2 = (\mathbf{P}_3 - \mathbf{P}_4)^2 \ \ and \ \ \mathbf{P}_1 + \mathbf{P}_2 = \mathbf{P}_3 + \mathbf{P}_4 \tag{3-5}$$

In momentum space, the first constraint means the two particle “distance” does not change, and second constraint means that the two particles “center of mass” position does not change. So it is easy to see that for given $\mathbf{P}_1$ with $|\mathbf{P}_1| > |\mathbf{P}_F|$ and $\mathbf{P}_2$ with $|\mathbf{P}_2| < |\mathbf{P}_F|$, the possible scattering results $\mathbf{P}_3$ are distributed on a sphere with center at $\frac{\mathbf{P}_1+\mathbf{P}_2}{2}$ and radius equals $\frac{|\mathbf{P}_1-\mathbf{P}_2|}{2}$, and $\mathbf{P}_4$ is at the symmetric other side of sphere. To guarantee possible solutions exist, in other words there is solution that $|\mathbf{P}_3| > |\mathbf{P}_F|$ and $|\mathbf{P}_4| > |\mathbf{P}_F|$, this sphere should has at least half of surface area outside of the Fermi surface, and this limit the possible choice of $\mathbf{P}_2$. When $\mathbf{P}_1$ becomes very close to Fermi surface, the possible volume of $\mathbf{P}_2$ and solution sphere area for $\mathbf{P}_3$ and $\mathbf{P}_4$ go to zero, and this means the lifetime of particle will diverge and the quasiparticle is well-defined. To better understand this idea, I plot a diagram to represent possible $\mathbf{P}_2$ choice and possible $\mathbf{P}_3$ and $\mathbf{P}_4$ solutions in figure below:

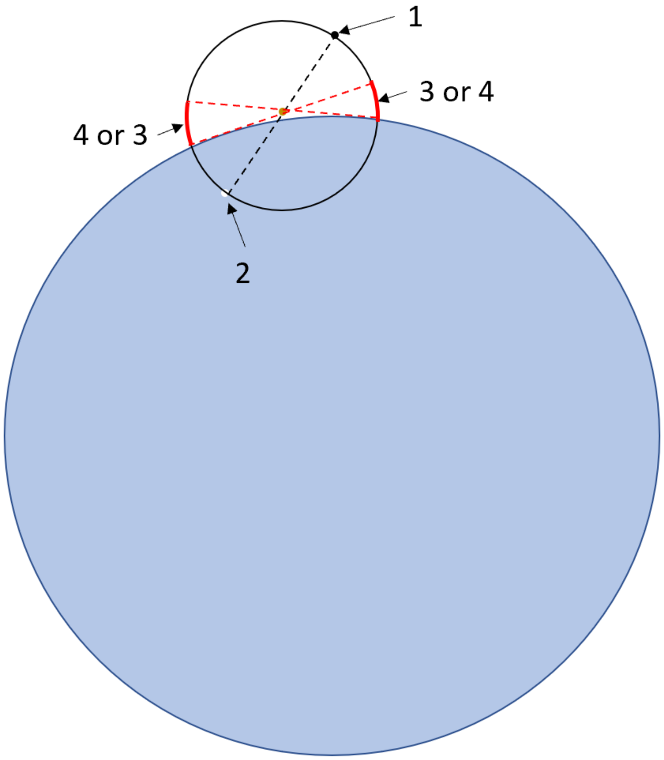

Figure 3-3. possible scattering process between a particle(1) above Fermi surface and another particle(2) below Fermi surface. The results are two particles(3 and 4) above Fermi surface. Blue circle represents Fermi sea or Fermi surface, black circle is the possible solution that decided by particle 1 and particle 2, red curves(corresponds to belt in three dimension) are the possible solution for particle 3 and particle 4.

If we define $\delta P = |\mathbf{P}_1| - |\mathbf{P}_F|$, as $\delta P \rightarrow 0$, the possible choice of $\mathbf{P}_2$ is limited to a thin shell with thickness δP and radius $|\mathbf{P}_F|$. The ratio total volume of this shell to the whole Fermi sea is proportional to $\frac{\delta P}{|\mathbf{P}_F|}$. Also, the choice of $\mathbf{P}_3$(length of red curve in

Figure 3-3) is proportional to $\frac{\delta P}{|\mathbf{P}_F|}$. So the total possible number of solutions is proportional to $\left(\frac{\delta P}{|\mathbf{P}_F|}\right)^2 \propto \left(\frac{\delta \epsilon}{E_F}\right)^2$, where $\delta\epsilon = \epsilon_1 - E_F$. According to Fermi's golden rule, the decay rate is proportional to the total number of possible scattering, and the lifetime, inverse of scattering rate, is proportional to $\left(\frac{E_F}{\delta\epsilon}\right)^2$ which diverges as $\delta\epsilon \to 0$. So, the quasiparticle states close to Fermi surface would be stable. Here I only consider the interaction with particles below Fermi surface and assume states below Fermi surface are fully occupied, in real situations, the interaction between quasiparticles and unoccupied states below quasiparticles always make them have finite lifetime. The well-defined quasiparticles make the Fermi liquid share many similar features with Fermi gas, such T-square resistivity at low temperature. More theoretical explanations can be found in Ref [108–111].

3.3. Strange metal

Normal metal's resistivity changes with temperature mostly because electron phonon scattering reduce the electron mean free path. This leads to two saturations at both low temperature side and high temperature side. At low temperature side, the quantized lattice vibrations are frozen out, and metal should have normal metal T-square resistivity plus residual resistivity according to Fermi liquid theory. At high temperature side, the mean free path can not be shorter than the atom distance, which set the lower bound for electron mean free path and higher bound for resistivity which is called Mott-

Ioffe-Regel(MIR) limit. However, there exist some “metals” have linear in temperature resistivity but do not saturate at either low temperature end or high temperature end or both. One of the most well-known example is cuprate which can have linear in temperature resistivity down to millikelvin [112,113] and up to 1100 K [114,115]. The mechanism of this “strange” behavior is still unclear, and people are even not sure if these “strange” behaviors in different systems share same reason because they show different types of “strange” behavior. For example, $SrRuO_3$ [116] and Sr_2RuO_4 [117] show linear in temperature resistivity at high temperature(1000 K) that is much higher than MIR limit, but have T-square resistivity at low temperature that is consistent with Fermi liquid theory. Another type of “strange” metal, such as $YbRh_2Si_2$ [118,119] and $YbBAl_4$(T exponent close to 1.5 rather than 1 at lowest temperature in $YbBAl_4$) [120], have strange metal properties at low temperature but the resistivity saturates at high temperature. Most of time, the strange metals refer to the materials with linear in temperature resistivity at low temperature. More examples of strange metals can be found in Ref [121]. Recently, researchers even find strange metal behavior in a bosonic system by punching array of holes on superconductor YBCO film [122], and they suggest there is a fundamental principle governing the transport that transcends the particle statistics.

There are many models trying to solve the strange metals problems such as phenomenological marginal fermi liquid [123], numerical Hubbard model [124], and gravity-related anomalous dimensions/Einstein-Maxwell-Dilaton model [125]. We won’t discuss the details of theory model in this thesis, and reader can find more information in Ref [121]. YbRh2Si2, the material we focused on in this thesis, show quantum criticality below 70mK by tuning magnetic field, and there is large range strange metal phase about this temperature. There are two broad classes of theories on metallic quantum critical point (QCP). One follows the standard Landau approach of order parameter fluctuations, and quasiparticles retain their integrity. Other approaches go beyond the Landau framework, by contrast, no long-lived quasiparticles are expected to remain. We hope to use noise measurement to reveal the possible mechanism in this system.

3.4. Quantum critical point in $YbRh_2Si_2$

In 1990s, people found some Ce-based f-electron heavy fermions deviate from Fermi liquid theory prediction at low temperature, where they can be tuned through antiferromagnetic quantum critical point by one control parameter such as doping, pressure and magnetic field [126,127].The non Fermi liquid behavior in $YbRh_2Si_2$ was first experimentally discovered by Trovarelli in 2000 [128]. They found the linear in temperature resistance below T = 10 K and magnetic phase transition around T = 65 mK. The results are shown in Figure 3-4. The left panel shows the magnetic phase transition below 65 mK, and this phase transition can be suppressed by increasing magnetic field. The resistivity is almost flat at high temperature range, but decreases fast below T = 100 K. The right panel shows the strange metal linear in temperature resistivity behavior below about 10 K. And this strange metal recover Fermi liquid T-squared resistivity after applying 6 T or higher out of plane magnetic field. They ascribed the non fermi liquid behavior to the presence of quasi-2D antiferromagnetic spin fluctuations related to this weak magnetic phase transition.

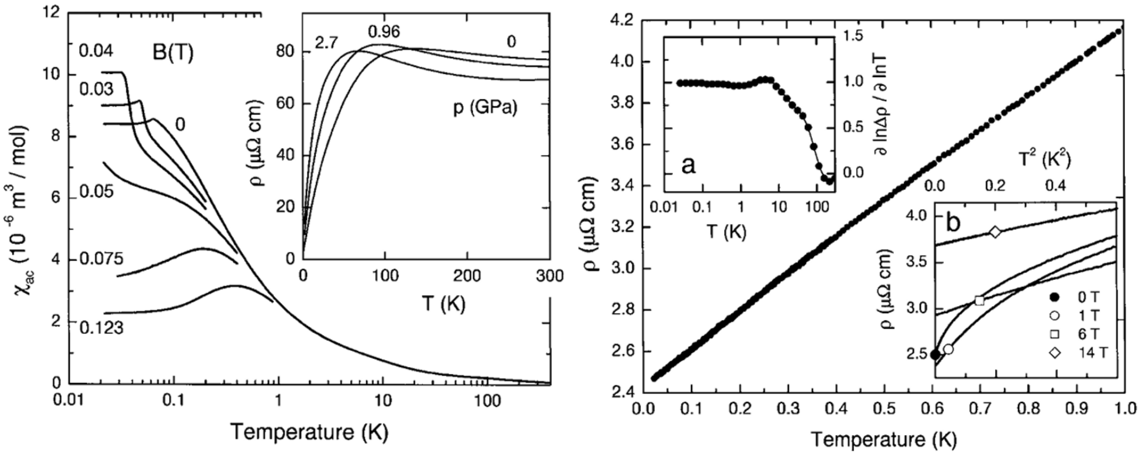

Figure 3-4 [128]. $YbRh_2Si_2$ non Fermi liquid behavior at low temperatures. Left: magnectic susceptibility of $YbRh_2Si_2$ dependence on temperature at different magnectic field. There is magnetic phase transition below T = 65 mK at B = 0 T, this phase transition is suppressed by increasing magnetic filed and disapper at T = 0.05 T. Inset shows the resistivity dependence on large temperature range at different pressure. Right: low-temperature electrical resistivity of $YbRh_2Si_2$ at pressure p = 0 measured along a axis as function of temperature, following $\rho(T) = \rho_0 + bT^{\varepsilon}$ with $\varepsilon \approx 1$. (a). Temperature dependence of the effective exponent ε, defined as the logarithmic derivative of $\Delta\rho = \rho - \rho_0$ with respect to temperature T. (b). resistivity dependence on temperature T^2. The T-squared resistivity recovered when the out of plane magnectic field increases higher than 6 T.

Two years later, researchers from same group got more detailed data on $YbRh_2Si_2$ [129]. They measured resistivity depending on temperature for multiple magnetic field perpendicular and along c axis, and plot phase diagram according to the resistivity measurement shown in Figure 3-5 below. Panel C shows the phase diagram with quantum critical phase transition. The quantum critical point at temperature T = 0 K by tuning magnetic field separates an antiferromagnetic phase and weakly polarized heavy fermion phase.

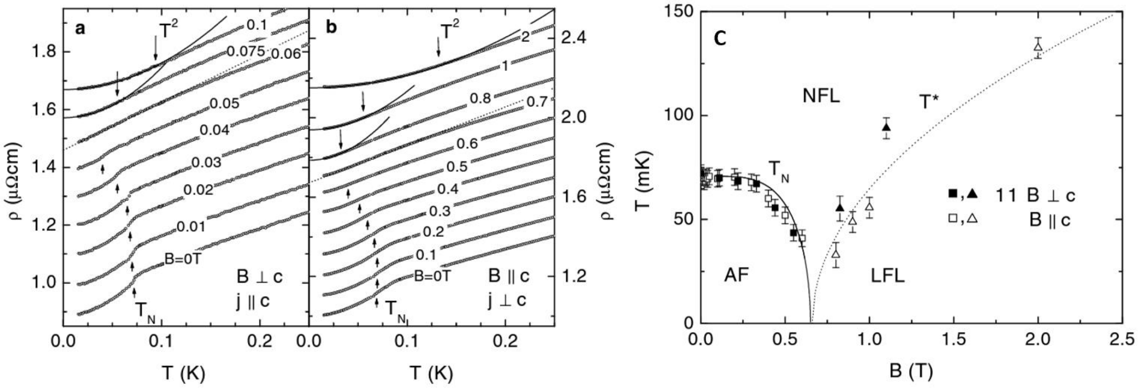

Figure 3-5 [129]. $YbRh_2Si_2$ low temperature resistivity dependence on temperature at varying magnetic fields applied along a axis (a) and along c axis (b). The resistivity are shifted by 0.1 $\mu\Omega$cm for different magnetic fields for clarity. The solid and dotted line are fittings using $\Delta\rho \sim T^{\varepsilon}$ with $\varepsilon = 2$ and 1 respectively. Arrows indicate the temperature below which the $YbRh_2Si_2$ has Fermi liquid T-squared resistivity. (c). The Fermi liquid T-squared resistivity is suppressed by increasing magnetic field. The $YbRh_2Si_2$ T-B phase diagram. T_N is the Neel temperature seperating the antiferomagnetic phase and non fermi liquid phase. T^* is the temperature seperating the non fermi liquid phase and Landau Fermi liquid phase. The magnectic filed values for B perpendicular to c axis is multiplied by a factor 11 to clarity.

More and more experiments on $YbRh_2Si_2$ were done after this. In 2003, people dope Ge to $YbRh_2Si_2$ and make high quality $YbRh_2(Si_{0.95}Ge_{0.5})_2$ single crystal with critical field heavily suppressed as low as $B_C = 0.027$ T ($\mathbf{B} \perp \mathbf{C}$), as shown in Figure 3-6 [118]. They found universal behavior in the temperature dependence of the specific heat and resistivity when $YbRh_2(Si_{0.95}Ge_{0.5})_2$ is tuned away from quantum critical point. In 2007, people reported an energy scale in the equilibrium excitation spectrum in addition to the one expected from slow fluctuations of the order parameter. Both energy scales go to zero when quantum critical point is reached, and provide evidence of a new class of quantum criticality [130]. In 2009, researcher found more complicated field-chemical pressure(by changing doping) phase diagram at low temperature [131]. In 2016, people even discovered the superconducting phase in $YbRh_2Si_2$ at extremely low temperature (around T < 2 mK) [132]. There is also experiment focusing the strange metal phase in $YbRh_2Si_2$. In 2020, people measured optical conductivity on molecular beam epitaxy-grown thin $YbRh_2Si_2$ films, and the results suggest that critical charge fluctuations play a central role in the strange metal behavior [133].

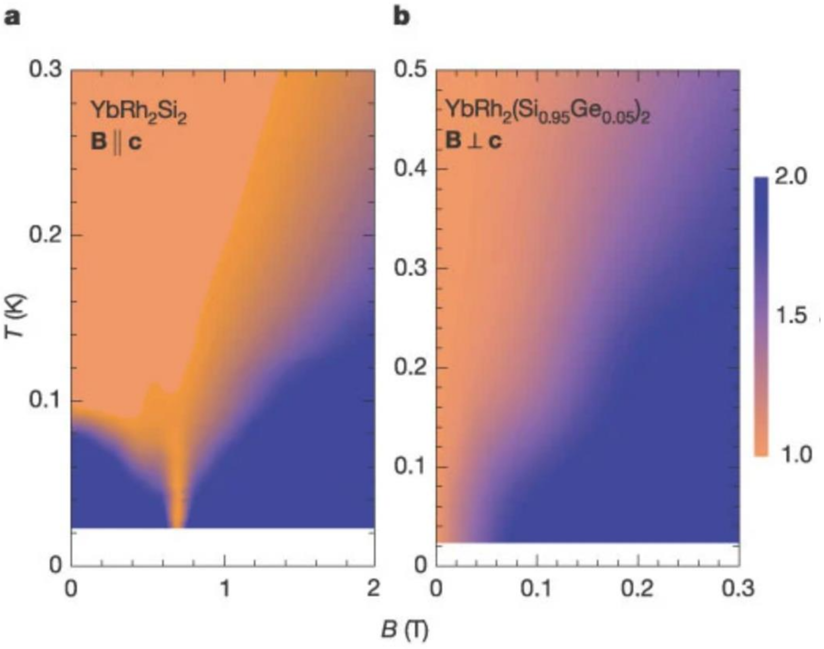

Figure 3-6 [118]. Evolution of ε, the exponent in $\Delta\rho(T) = [\rho(T) - \rho_0] \propto T^{\varepsilon}$, within the temperature-field diagram of YbRh$_2$(Si$_{0.95}$Ge$_{0.5}$)$_2$ single crystal.

Chapter 4

Experiment setup

4.1. Low frequency noise measurement

4.1.1. Low frequency noise measurement setup

To mitigate the input noise of the voltage amplifiers used in the measurement, we used two independent amplifier chains to measure the low frequency (below 100 kHz) voltage noise under a known dc current bias. Amplifier noise for the two chains is nominally uncorrelated, while voltage fluctuations across the sample will be detected by both chains. Cross-correlation of the amplifier outputs then reveals the noise from the sample itself [134]. Figure 1C shows the electrical circuit diagram of the experimental setup. A programmable voltage source (NI-DAQ6521) was followed by multiple LC filters to drive a clean dc current through two large current-limiting resistors (~1 MΩ each). The sample was mounted on a custom low frequency measurement probe and inserted into a cryostat (Quantum Design PPMS). The noise measurement is very sensitive to environmental influence, so the whole probe is isolated from PPMS's ground.

The measurement wiring are twisted pairs to reduce magnetic field induced noise. The sample, LC filters, transmission lines and first pair of pre-amplifiers are shielded by a Faraday cage to reduce environmental noise. The voltage noise generated by the resistance fluctuations is collected by two separate amplifier chains, each consisting of two preamplifiers (NF LI-75 and Stanford Research SR-560). The two amplified signals are recorded by a high-speed data acquisition device (Picoscope 4262). Typically time series containing 2,000,000 data points is taken with a sampling rate of 10 MHz. The cross-correlated noise spectral density is calculated based on the two separate time series (x_t and y_t) from each amplifier chain, averaged over 200 to 300 times:

$$S_{xy}(f) = \sum_{\tau=-\infty}^{\infty} \mathrm{E}[x_t y_{t+\tau}]\, e^{-2\pi i \tau f} \tag{4-1}$$

where E[ ] is expectation value. Unavoidable parallel parasitic capacitance comes from the sample mounting and cryostat wiring, leading to the capacitive suppression of measured voltage noise at high frequencies. The measured noise spectral density can be expressed as:

$$S_V(f) = \frac{4k_B TR + S_{v,R}}{1 + (2\pi f R C_P)^2} \times G \tag{4-2}$$

where R is the differential resistance of the sample at the applied bias current, $4k_B TR$ is the Johnson-Nyquist thermal voltage noise, $S_{v,R}$ is the voltage noise from resistance fluctuations, C_P is parasitic capacitance, and G is the total power gain. Data are consistent with a constant C_P (~320pF).

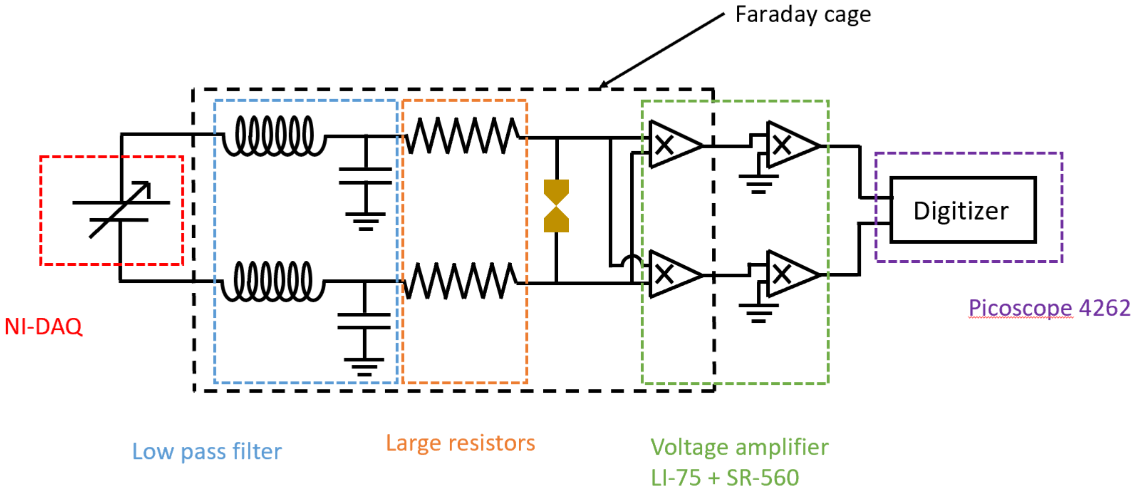

Figure 4-1: Electrical circuit diagram of low frequency noise measurement setup. The filtered constant current flows through the device, supplied by a programmable voltage source NI-DAQ (red color) and current-limiting series resistors (orange color, values depend on maximum current required). Customized low pass filters (blue color) prevent high frequency noise from the voltage source from reaching the sample. The voltage fluctuations across the sample (shaded rectangle) are amplified by two chains of preamplifiers in parallel (green color); both amplifier chains are recorded by a high speed digitizer Picoscope 4262 (purple color). The dashed line is a Faraday cage to shield the environment noise.

4.1.2. Low frequency noise measurement calibration

The room temperature thermal noise of a variety of resistors was used to calibrate the setup. The voltage noise power spectral density found from the cross-correlation can be expressed as

$$S_V(f) = \frac{4k_BTR_s}{1 + (2\pi f R_s C_P)^2} \times A \qquad 4\text{-}3$$

where $4k_BTR_s$ is the Johnson-Nyquist voltage noise at the resistor Rs, $1/(1 + (2\pi f R_s C_P)^2)$ is the decay coefficient because of parasitic capacitance, A is a coefficient containing the squared amplifier gain and a numerical factor related to the cross-correlation parameters (number of data points of each time series, the sampling frequency and the Hanning window for the Fourier transform).

The thermal noise spectra for different resistors are shown in Figure 3.2.a. The lowest spectrum is corresponding to 15 Ω thermal noise, and highest one is 10 kΩ. The noise peaks at 60 Hz, 120 Hz, 180 Hz and higher harmonics result from pick-up of environmental noise. Despite strong efforts to optimize measurement grounding, these peaks are related to AC electrical power and are very hard to totally suppress even by the cross-correlation method. The decay of $S(V)$ at high frequencies results from effective low-pass filtering due to parasitic capacitance and the differential resistance of the device. As expected from the expression $1/(1 + (2\pi f R_s C_P)^2)$, the noise of larger resistance devices decays more rapidly with increasing frequency. Each spectrum is fitted with the formula:

$$S_{V,meas}(f) = \frac{S}{1 + (2\pi f R_S C_P)^2} \times A \qquad 4\text{-}4$$

The fitting curves are shown by narrow colorful curves. A robust fitting technique [45,135] was applied to reduce the impact of environment pick up peaks on the fitting results.

In Figure 3.2.b, we plotted the fitting results $S \times A$ versus R_s. A linear regression finds the relation between noise intensity and resistance:

$$S \times A = 5.14^{-13} \times R_s + 1.129^{-12} \qquad 4\text{-}5$$

The intercept means the system has around 2 Ω room temperature (T ≅ 297K) thermal noise background, and this is much smaller than the noise intensity we measured. The linear fitting is shown by the red line in Figure 3.2.b. The fitting matched very well with experiments, showing that the zero-bias noise intensity is strictly linearly proportional to the resistance, as expected for Johnson-Nyquist thermal noise. The fitting is shown in log scale to see all data clearly. From the formula above, we find the value of $A = \frac{5.14^{-13}}{4k_B T} = 3.14 \times 10^7$. From our definition, A is dimensionless.

It is worth noting that the value A maybe related to the parameters setting of the data taking program, including sampling frequency, window function, data points, noise probe and so on. We calibrate every time after we adjust these parameters setting. We also used the thermal noise change of constant resistor from 300K to 2K to calibrate setup. The process is totally same as above, but varying T rather than R, and I won't repeat the description.

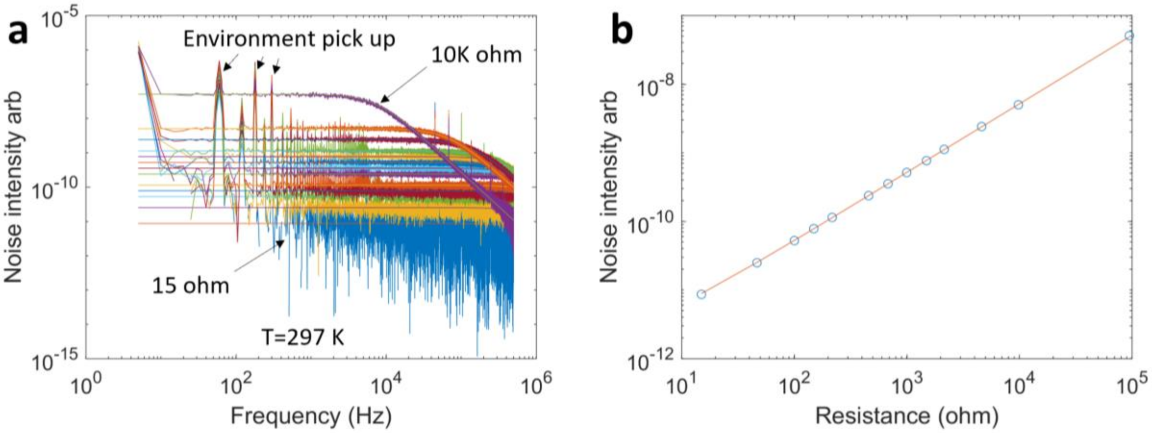

Figure 4-2: (a) Low frequency thermal noise spectra for different resistors at room temperature. Resistance varies from 15 Ω to 10 kΩ. A robust fitting procedure is applied to reduce the influence of unintended environmental pick up of discrete narrow-band signals. (b) Noise intensity versus resistances value. Linear fitting between the noise intensity and resistance is shown by the red line.

4.2. High frequency noise measurement

4.2.1. High frequency noise measurement setup

We used two approaches to measure noise power at radio frequencies in the V_2O_3 experiments, both requiring that the sample be mounted on a second custom probe with coaxial wiring and a RF-specialized sample carrier with integrated bias-tee (1nF capacitor and 12 μH inductor). In the first approach, we use high frequency amplification and a spectrum analyzer to record the frequency-dependent noise spectral density (10 MHz - 1 GHz) directly. Effective bias tees allow the separation of current-biasing of the sample and measurements of the RF power. The voltage source (NI-DAQ6521) and current-limiting resistor provide a constant bias current through sample, and the unfiltered signal is amplified by three RF power amplifiers (20dB gain for each). The high frequency spectrum is recorded by a spectrum analyzer(E4402B) and each spectrum is averaged over 200 times. It is necessary to account for the frequency-dependent background noise power (originating from noise on the input stage of the first RF amplifier and waveguide modes due to impedance mismatch between the sample and the 50 Ω RF system). To do this, the extra noise spectrum due to the applied bias current (the data of interest) is obtained by subtracting the zero-bias spectrum from each particular spectrum.

We also used a lock-in technique [136,137] to measure the integrated noise power from 225 MHz to 580MHz. A square-wave bias (7.7 Hz) between 0 V and the desired bias voltage level is generated by a function generator (DS345) and applied to one side of the sample through a current-limiting resistor and LC circuit (to limit the current and suppress any extrinsic high frequency noise from the biasing setup, respectively). At the output port, the low frequency current flows through the inductor and is recorded by the combination of current amplifier (SR 570) and lock-in amplifier (SR 7265). The high frequency noise signal flows through the capacitor and is filtered by a low pass filter (< 580 MHz) and high pass filter (>225 MHz). The filtered signal is amplified by three RF power amplifiers (20dB for each) and detected by a power detector (Mini-Circuits zx47-60LN-S+ 10-8000MHz). The integrated RF noise intensity is thus converted to a voltage signal and recorded by a lock-in amplifier (SR7270) synchronous with the square wave.

Analogous to the low frequency approach, we used thermal noise of different value resistors to calibrate the high frequency setup. Because of the huge range of V_2O_3 sample resistance change during the metal-insulator transitio, the impedance mismatch is unavoidable for our measurement. The dominant contribution to the sample impedance appears to be the resistance. We used the thermal Johnson-Nyquist noise of different value resistors to calibrate the RF setup detection efficiency as a function of sample resistance. The total collected power can be expressed as:

$$P = \frac{4k_BT}{R} \times \frac{ZR^2}{(R+Z)^2} \times A + S_b \tag{4-6}$$

where P is the total detected power; $4k_BT/R$ is thermal Johnson-Nyquist current noise intensity, R is the resistance for each resistor used to do the calibration, Z (50 Ω) is the impedance of transmission line, power amplifier and power detector. A is the product of bandwidth and gain, which is independent of sample resistance. S_b is the measurement system background noise power.

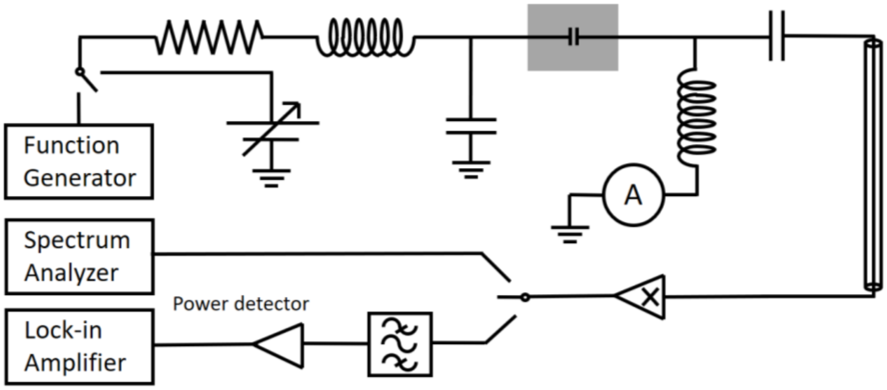

Figure 4-3: Electrical circuit diagram of high frequency noise measurement setup. Current bias is applied to the sample (shaded rectangle) using a voltage source and function generator and a current-limiting series resistor (20 k Ω). The high frequency signal and low frequency bias current are separated by bias tees (C = 1 nF, L = 12 μH). Function generator and lock-in amplifier combined to measure integral noise (225 MHz to 580 MHz). High frequency spectra are recorded by spectrum analyzer when applying constant current by voltage source.

4.2.2. High frequency noise measurement calibration

One key difficulty for the high frequency noise measurement is the impedance mismatch problem between the device of interest and the 50 Ω RF measurement electronics. When RF power is transferred to one end of a coaxial cable, the signal would be reflected back if the terminating impedance is different than the effective impedance of coaxial cable. The reflection of the signal is related to the signal frequency. The reflected signal will interfere with the original to make frequency-dependent standing wave resonances in the system. In many standard RF circuits, all the components, such as the transmission lines and input/output impedances of filters and amplifiers, are designed to a characteristic impedance of 50 Ω, to minimize reflections and standing waves as well as free-space radiation. However, the resistances of our devices can vary over several orders of magnitude across the metal-insulator transition, altering the RF pick up efficiency. For loads well over 50 Ω, one approach is to use LC circuits to transform or match the impedance to measurement electronics, but it is difficult for such a network to work for a large resistance range, and the narrow-band matching tends to lose broad-band information.

We used the thermal noise from different resistors at different temperatures to calibrate our broadband RF setup in two different ways, determining the frequency-dependent measurement efficiency for different resistance values. The noise spectra for substituting a 50 Ω resistor for the sample from T = 300 K to 10 K are shown in Figure 3.4.a. The upper blue curve is the thermal noise spectrum at 300 K, and the lowest one is 10 K. The peaks below 100 MHz and around 750 MHz are the background from the power amplifier chain and spectrum analyzer, which affect the measurement in those ranges. The spectrum is frequency dependent because the power amplifiers (Minicircuits zx60-33LN-S+) have frequency-dependent gain over this broad range. The small oscillation at higher frequency is likely caused by parasitic reactance contributions. The integrated noise from 250 MHz to 400 MHz for a 50 Ω resistor as a function of temperature are plotted in Figure S2.b. The red line is a linear fit. The noise and the resistor are expected to have the relation:

$$P = \frac{4k_BT}{R_0} \times \frac{Z{R_0}^2}{(R_0 + Z)^2} \times A + S_b \qquad 4\text{-}7$$

Here P is the total detected power; $4k_BT/R_0$ is thermal Johnson-Nyquist current power spectral density, R_0 is the resistance for each resistor, Z (50 Ω) is the impedance of transmission line, power amplifier and power detector. A is the product of bandwidth and gain, which is independent of sample resistance. S_b is the system background intensity, including the power amplifier background and the environment background from measurement system. We have repeated these temperature-dependent measurements for a variety of different resistors. The slopes for different resistors are shown in Figure 3.4.c. The formula for the measured power is used to fit the resistance-dependent slope and is shown by the red curve. The curve does not converge to zero in the high R_0 limit, implying that there is an environmental background changing with temperature. Using the relationship above, and the inferred values of A and Sb, we can then convert between measured broadband noise and the intrinsic noise at the sample.

For a related approach, we use the thermal noise of a 50 Ω load between two different reference temperatures as a known amount of input noise, to find the corresponding output noise of the amplifier chain. The ΔT = 290 K 50 Ω thermal noise spectrum is obtained by using the T = 300 K noise spectrum and subtracting the T = 10 K noise spectrum, to minimize the effect of background noise, and shown in in Figure S2.d. This standard 50 Ω ΔT = 290K thermal noise spectrum is used as a reference to calibrate other RF spectra we measure.

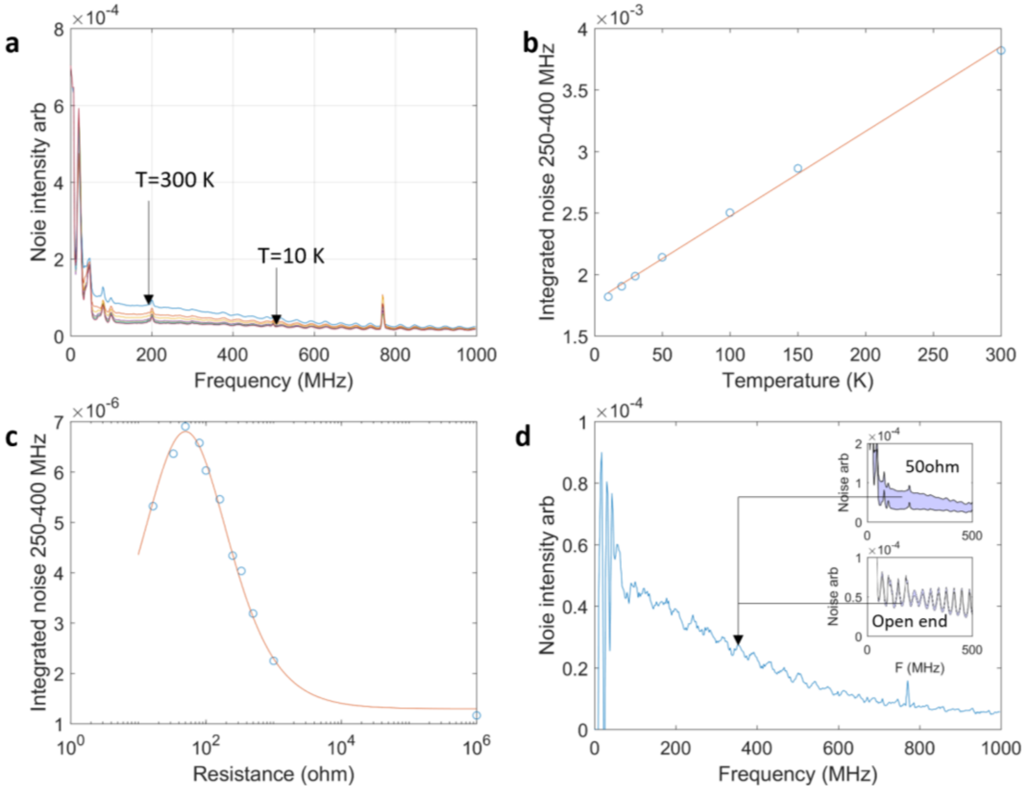

Figure 4-4: (a) High frequency thermal noise spectrum of 50 Ω resistor at different temperatures. (b) The integrated noise from 250MHz to 400MHz as a function of temperature. Linear fitting between noise intensity and temperature is shown by the red line. (c) The slope of analogous linear fits for different load resistors, as a function of the load resistance. Red line is the fit using the theoretical expectation for different resistors and including a background. (d) The standard ΔT = 290 K 50 Ω thermal noise spectrum obtained by using the increase of 50 Ω thermal noise from 10K to 300K minus the increase of background. The inserted figures are spectra of the 50 Ω resistor and the unterminated open ended measurement setup at 10 K and 300 K respectively.

Chapter 5

Percolation and nanosecond fluctuators in V_2O_3 films within the metal-insulator transiton

In this thesis we report measurements of the intrinsic, thermally driven resistance fluctuations in the mixed phase regime of the V_2O_3 metal-insulator-transition, via noise spectra under bias currents sufficiently small as to be non-perturbative [138]. We extend the frequency range of noise measurements up to 1 GHz, and find resistive fluctuations (noise intensity quadratic in measurement current) up to several hundred megahertz, implying the existence of nanosecond fluctuators, a timescale comparable to those found in experiments probing the nonequilibrium metal-insulator transition. Lorentzian-like roll-offs are seen at the upper limit of our frequency range, and particularly toward the insulating regime, indicating that noise can be dominated by a small numbers of fluctuators. We compare noise intensities and scaling with those expected from thermodynamic considerations of the transition and its percolative nature. We find quantitative agreement with a 2D percolation model based on fluctuations in percolating fraction, though the thermodynamics of the transition make it unlikely that fluctuation-driven transitions of entire domains between metallic and insulating states are at work. In devices with the largest current density, the dependence of the noise intensity with bias current becomes superquadratic, implying that the applied bias is perturbing the dynamics of the fluctuators.

5.1. Device fabrication

V_2O_3 thin films 100 nm-thick were grown epitaxially on r-cut sapphire substrates by RF magnetron sputtering deposition by our collaborator Ivan Schuller at UC San Diego. For measurement, 70 nm thick Au electrodes (6 nm V adhesion layer) were patterned by electron beam lithography, electron beam evaporation, and liftoff. After lithography and development, the exposed surface was cleaned by Ar plasma (9W) for 1 minute before electrode deposition. The ratio of width to height of each electrode gap is fixed to 1:4 for all device sizes as shown in Figure 1A. The large electrode bonding pads are farther to the two sides, separated by around 3 mm. To avoid possible inhomogeneities in composition and film degradation from the etching process, the films were left intact, with electrode design and aspect ratio ensuring that the device conduction is limited by the interelectrode region (Figure 5 -1 .a,b). Four device geometries (10 × 40 μm, 20 × 80 μm, 40 × 160 μm, 80 × 320 μm) were used, all with identical aspect ratios, such that two-terminal device resistances in the metallic state were identical for all devices, but with varying current densities for the same applied bias.

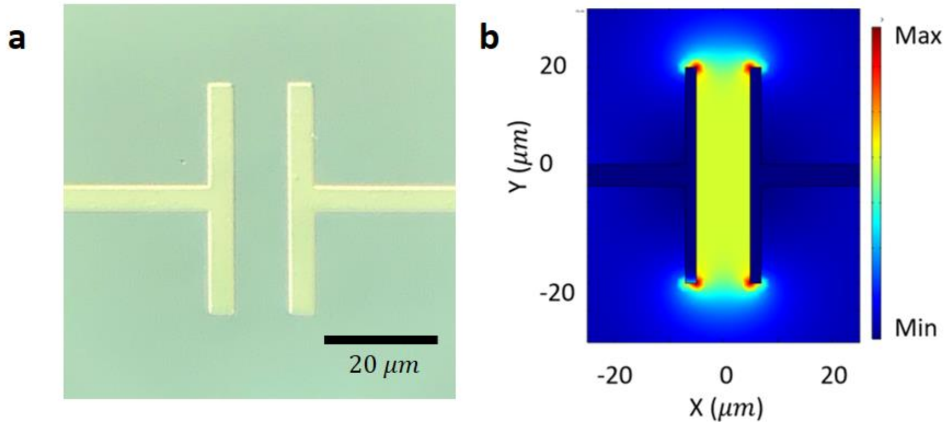

Figure 5-1: (a) Optical microscope image of the 10 μm × 40 μm device. The Au(70 nm)/V(7 nm) electrode are deposited on the surface of V_2O_3 film, leaving a narrow gap with width height ratio equals 0.25. (b) The simulation from Comsol shows most of current (shown here in arbitrary units) is confined in the small region between the gap when the film resistivity is in the range explored in the present noise measurements.

5.2. Device characterization

The DC electronic conduction of the V_2O_3 film devices was measured by recording the resistance during the cooling and warming cycle, using a source meter (Keithley 2400, 10 mV output). The temperature was settled for 5 minutes at every 0.5 K through the transition to allow the device temperature to stabilize. Figure 5-2.A shows the resistance changes with temperature in the cooling and warming cycle. In the cooling cycle, the antiferromagnetic insulating domains start to appear around 160 K, and gradually replace the paramagnetic metallic domains. This transition happens rapidly with temperature between 150 K and 130 K, causing the resistance to increase by about 4 orders of magnitude. The resistance continues to increase to almost $10^7\times$ larger than the pure metallic phase when cooling down to 100K. In the warming cycle, the transition from the antiferromagnetic insulating domains to the paramagnetic metallic domains is about 7 K higher than cooling cycle, showing thermal hysteresis.

At each temperature for which we measured noise, the current-voltage (*IV*) characteristic is also recorded. At the low voltage bias range, as shown in Figure 5-2.B, the *IV* curve is almost linear and did not show any obvious hysteresis (either from possible current-induced changes in domain configuration, or from heating coupled with thermal hysteresis), which allows us to take noise spectrum without considering the effect of change of thermal noise.

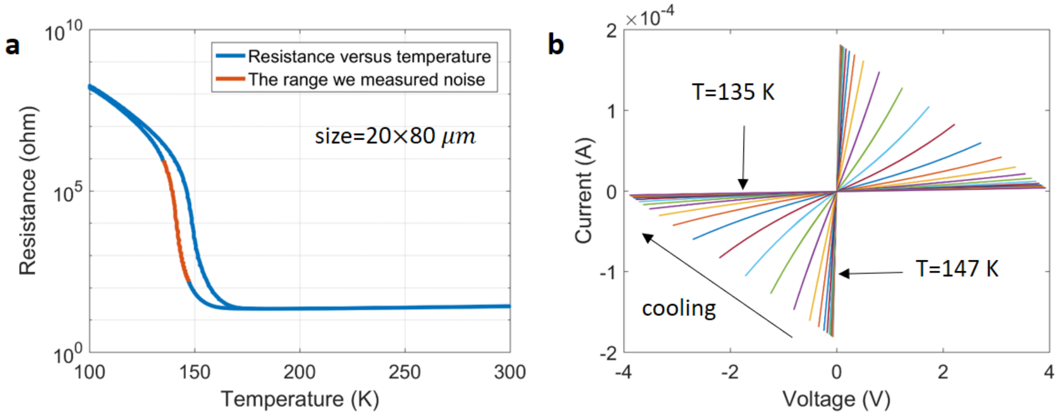

Figure 5-2: (a) Resistance of the device versus temperature on cooling and warming cycle. (b) The IV curve at small bias range in different temperature are almost linear.

5.3. Low frequency noise measurement

Figure 5-3.A shows a T = 143.5 K typical low frequency noise spectrum at equally stepped bias currents. The lowest flat spectrum corresponds to zero bias thermal noise background. A slope of -1, corresponding to pure $1/f$ dependence, is indicated by the black line. For initial analysis, we assume a $1/f$ form of the low frequency noise, to better highlight deviations from that form. The spectra are fitted with the formula:

$$S_I(f) = \frac{S_V(f)}{R^2} = \frac{4k_BT/R + \mathrm{S}_{1/f}/f}{1 + (2\pi f R C_P)^2} \qquad 5\text{-}1$$

where $\mathrm{S}_{1/f}$ is corresponding to the $1/f$ noise intensity at frequency equals 1 Hz at given current, R is the resistance of device, and $S_I(f) = \frac{S_V(f)}{R^2}$ is current fluctuation.

The contribution to the noise from the resistance fluctuations should have the form: $I + \delta I = \frac{V}{(R+\delta R)} = \frac{V}{R} - \frac{V}{R} \times \frac{\delta R}{R}$, $(\delta I)^2 = \left(\frac{V}{R}\right)^2 \left(\frac{\delta R}{R}\right)^2 = I^2 \left(\frac{\delta R}{R}\right)^2$. This implies that the current noise from resistance fluctuations should be proportional to the square of the bias current, if the resistance fluctuations do not change with current. The dependence of the inferred noise intensity $\mathrm{S}_{1/f}$ on bias is shown in Figure 5-3 B. The quadratic relation between noise intensity and current shows that this low frequency noise contribution results from resistance fluctuations.

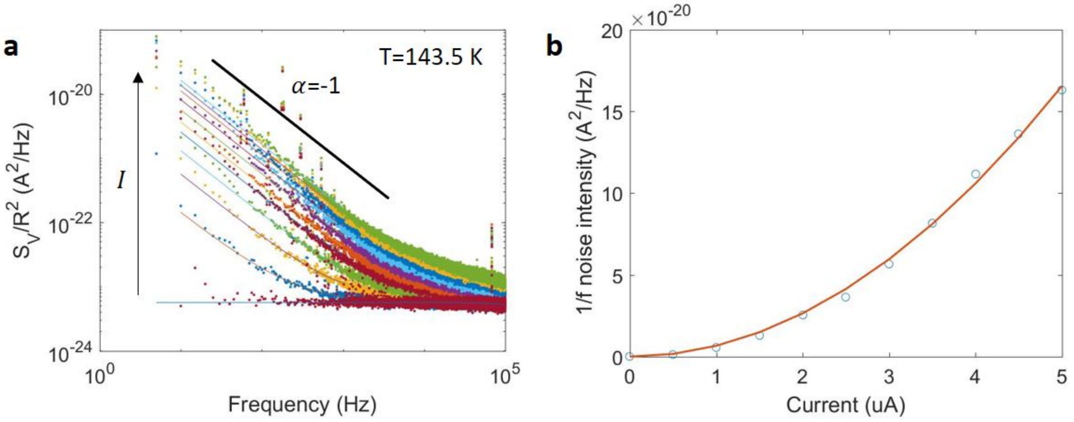

Figure 5-3: (a) typical spectrum of low frequency noise at 143.5K. The spectrum was taken at equally stepped bias. Black line indicates the slope equals -1. (b) Quadratic fitting of at 1Hz.

5.4. High frequency noise measurement and comparison with low frequency noise

Figure 5-4.A shows an example of the high frequency noise spectra (with the zero-bias spectrum subtracted) at several equally stepped bias current values. The normalized low frequency spectra are plotted on the same axes to show the full accessible frequency information. The low frequency spectra are scaled using the quadratic current dependence so that the highest bias current data for low and high frequency sets are equivalent, to account for the different currents in the low and high frequency measurements. The capacitive effects have also been compensated. From Figure 4.4.A, Lorentzian noise is observed in both the high frequency range and low frequency range, implying that individual fluctuators are strongly affecting the total resistive fluctuations here. A typical Lorentzian noise has the form

$$S_L(f) \propto \frac{1}{(2\pi f)^2 + (1/\tau)^2} \qquad \text{5-2}$$

where τ is the effective lifetime of the fluctuator. According to the fitting, the lifetime of these two dominant fluctuators are around 0.35 ns and 176 μs. More RF Lorentzian noise examples are shown section 4.5, and the inferred effective lifetimes range from 1 ns to 0.2 ns.

The RF lock-in detection method can increase the sensitivity at the cost of spectral information. Figure 5-4.B shows the measurement of integrated noise intensity at 141K. The blue curve is measurement data, the red one is a quadratic fit, again showing consistency with the noise intensity being produced through resistive fluctuations. The green curve is a calculation based on fitting the low frequency noise to an expected $1/f$ dependence and extrapolating to the RF bandwidth probed in the lock-in measurement. We routinely find that the measured RF signal is larger than the extrapolated expectation. This indicates the existence of more high frequency fluctuators than would be expected from either the usual $1/f$ noise or Lorentzian fluctuators at low frequencies.

The resistive noise, translated into voltage spectral density S_V via a bias current, is typically quantified by $(S_V/(IR)^2)v_s f = \alpha/n$. For reference, values of α/n found in disordered metals are 10^{-21}-10^{-23} cm^3 and 10^{-18}-10^{-21} cm^3 for semiconductors, respectively [18,139]. Surprisingly, in the mixed-phase regime of the $La_{5/8-x}Pr_xCa_{3/8}MnO_3$ MIT, α/n is as large as 10^{-10}-10^{-7} cm^3. In the VO_2 mixed phase regime [95], in contrast, α/n is around 10^{-22}-10^{-24} cm^3, comparable to the disordered metal cases. Here, we find α/n is around 10^{-18}-10^{-20} cm^3, much larger than in VO_2 . Further interpretation is challenging without additional assumptions of a microscopic model for the fluctuators, discussed below.

Figure 5-4.C,D show how the integrated noise and extrapolated $1/f$ noise expectation change with resistance. The noise is maximized in the mixed phase regime, and much smaller (below our sensitivity to detect) in the fully metallic state. In scaling models of percolation [18,97,139,140], there is a connection between percolation cluster size and resistive noise, such that $S_V/(I)^2 \propto (p - p_c)^{-k}$, where p is the percolating phase fraction, p_c is the critical concentration, and k is a critical exponent. Similarly, the resistance should also scale critically with p, with the resulting expectation that the normalized resistance noise $S_V/(IR)^2 \propto R^{-x}$ where x is another critical exponent. Looking at Fig 5-4.C and find values of x around 1.5. For comparison, VO_2 in the mixed phase regime showed x values of approximately 2.6 on both the insulating and metallic sides of the transition [95]. Differences in the resistive noise of the MIT between VO_2 and V_2O_3 is perhaps not surprising, given prior indications that the connections between structural and electronic transitions in the two oxides differ [141,142].

The value of x = 1.5 on both sides of the mixed phase regime (metal-rich and insulator-rich) is quantitatively consistent with predictions of so-called "p-noise" in 2D [100]. In this model, the noise results from fluctuations that switch off or on connections between conducting regions (that is, fluctuations in the conducting fraction p) rather than changes in the resistance of the conducting regions themselves. An additional assumption is that the temperature dependence of the fluctuations in p is weak compared to that of the resistance itself. To qualify as 2D, one would require typical domain sizes to be larger or comparable to the film thickness.

In light of this agreement with p-noise predictions, it is worth considering how the physics of the MIT constrains possible fluctuation mechanisms. In thermal equilibrium at temperature T, statistical mechanics in the canonical ensemble shows that the mean square energy content fluctuations of a volume v are given by $(\delta E)^2 = (C_v v)k_B T^2$, where C_v is the specific heat per unit volume. If the resistance fluctuations result from some thermally fluctuating volume v being fully converted between metallic and insulating phases, that would require $\delta E \sim Lv$, where L is the latent heat per unit volume, 65 J/cm^3. [143]. Rearranging, $v \sim (C_v/L^2)k_B T^2$. Assuming that the lattice specific heat dominates (approximately 3.2 J/Kcm^3) and T = 150 K gives a typical volume scale of 240 Å^3, comparable in volume to a single unit cell. This and the hysteretic nature of first-order transitions imply that it is unlikely that the resistance fluctuations involve wholesale switching of metallic or insulating domains. The thermal energy available in a typical fluctuation should only be sufficient to shift phase boundaries by a couple of lattice spacings. From nanooptical characterization of percolation in this system [87], it is unclear whether such small characteristic distances would be able to alter the connectivity of the conducting network sufficiently to explain the relevance of the p-noise model and the measured noise intensity. The appearance of Lorentzian noise in the measurements, particularly near the maximum in noise amplitude at the percolation threshold (Fig. 5-4.A) does suggest that small numbers of fluctuators can have a strong influence on the connectivity of the network as a whole.

An alternative possible source of resistive fluctuations and changes in the connectivity of conducting regions could be scattering of carriers by fluctuating antiferromagnetism, as the system sits at the boundary between the paramagnetic metal and the AFM insulator. Slow fluctuations of AFM domains [144] lead to $1/f$ noise in metallic Cr around and below the bulk Neel temperature [145]. The detection of resistive fluctuations up to the short timescales accessed in the present experiments further constrain possible fluctuation mechanisms to those compatible with such rapid dynamics. It is not clear that the hysteretic characteristic of the first-order bulk MIT including the structural transformation is compatible with such rapid equilibrium fluctuations.

We also compare the noise intensity for different size devices, the results are shown in Figure 5-4.F. For larger devices, the noise due to resistive fluctuations is smaller, presumably of ensemble averaging over the larger device area. In the smallest devices, in which the current densities and electric fields are largest, the lock-in measurement of integrated high frequency noise shows pronounced deviations from a quadratic dependence of the noise intensity with bias current (Figure 5-7. A). The measured noise shows instabilities at high biases (not readily apparent in the current-voltage characteristic itself), and tends toward a superquadratic dependence on current. These traits indicate that at the high current/field limit, the current itself is no longer serving as a nonperturbative probe of resistance fluctuations, but instead is driving domain dynamics, including those at hundreds of MHz. Noise of the kind presented here may serve as a sensitive probe for the dynamics of switching phenomena in this system, an area of fundamental interest and importance for neuromorphic applications of metal-insulator transitions [146].

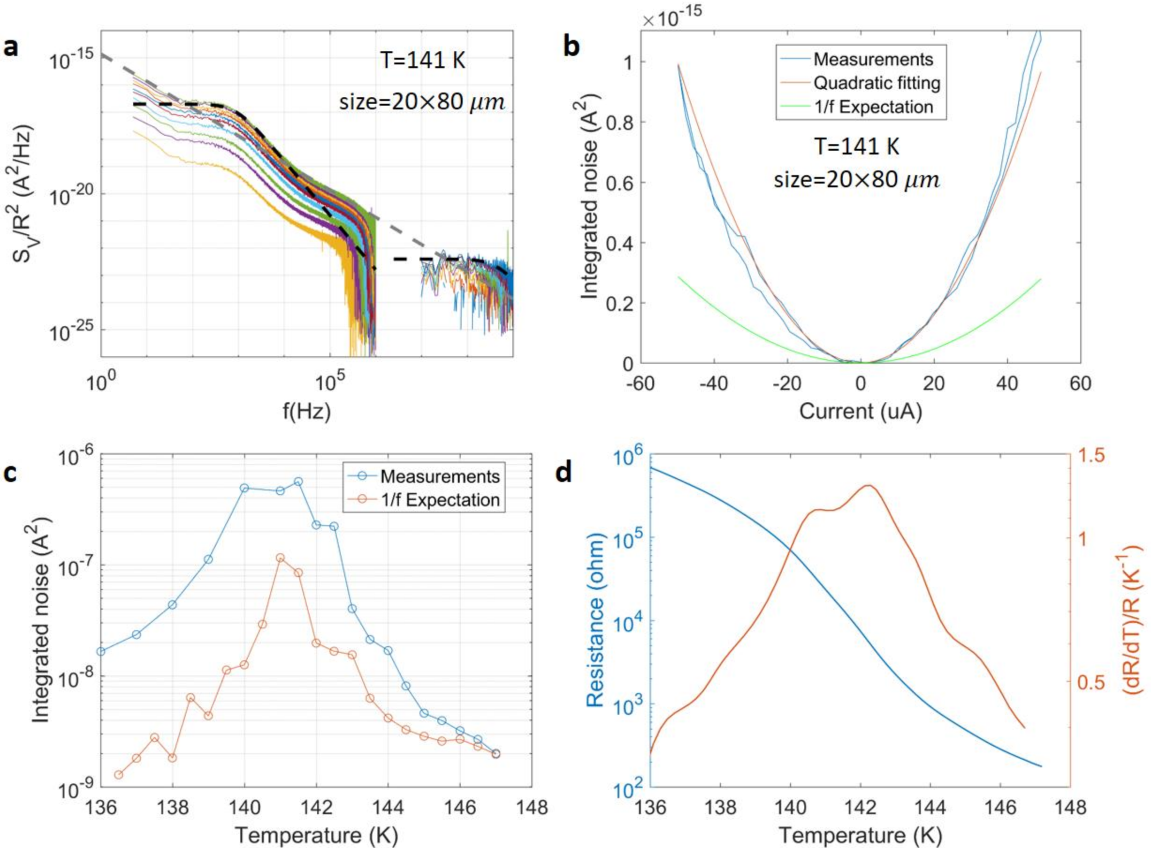

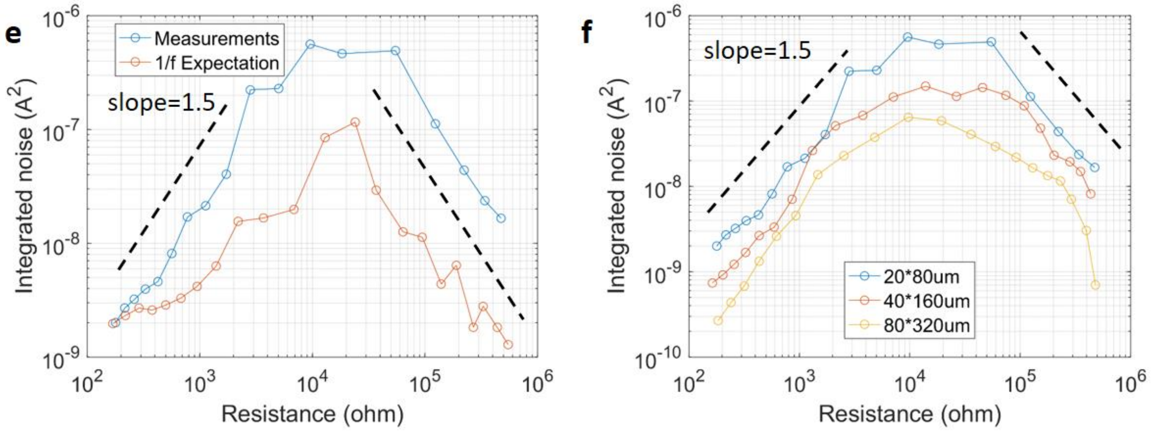

Figure 5-4: (a) Low frequency and high frequency spectrum of same device at 141 K (resistance $24\,\mathrm{k\Omega}$). The low frequency noise has been inferred accounting for the capacitive roll-off in Eq. (4) and multiplied by a factor to compensate for the quadratic current dependence and the current difference between the low and high frequency measurements. The three dashed line are corresponding to $1/f$ and two Lorentzian noise fitting. (b) The integrated noise measured by power detector(blue), a fit to a quadratic current dependence (red), and the expected integrated high frequency noise based on an extrapolation of the low frequency spectrum(green) at same temperature assuming a $1/f$ frequency dependence. (c) For each temperature, the integrated noise measured by RF power detector with lock-in amplifier, and the expected integrated noise over the same bandwidth based on an extrapolation of the low frequency noise assuming a $1/f$ frequency dependence. (d) For this same device, resistance R and normalized derivative $(dR/dT)/R$ as a function of temperature for a typical temperature cooldown. (e) The integrated noise measured by RF power detector with lock-in amplifier and the expected integrated noise over the same bandwidth based on an extrapolation of the low frequency

noise assuming a $1/f$ frequency dependence versus device resistance. (f) The integrated noise versus device resistance for different size devices.

5.5. Statistic of RF fluctuators lifetime

The noise spectra in the RF high frequency range shows clear Lorentzian noise shapes at some temperatures, which correspond to fluctuators with certain dominant effective lifetimes. We fit the noise to the Lorentzian form for noise spectra of the size 20×80 µm device, since of the devices it has relatively large signals and a clear Lorentzian noise shape. The statistical information is shown in Figure 5-5.A. The mean effective lifetime found through this analysis is around 0.5 ns. Two examples of Lorentzian noise fitting at T = 143.5K and 140K are shown in Figure 5.5.B and Figure 4.5.c. The fitting curves are indicated by the dashed lines.

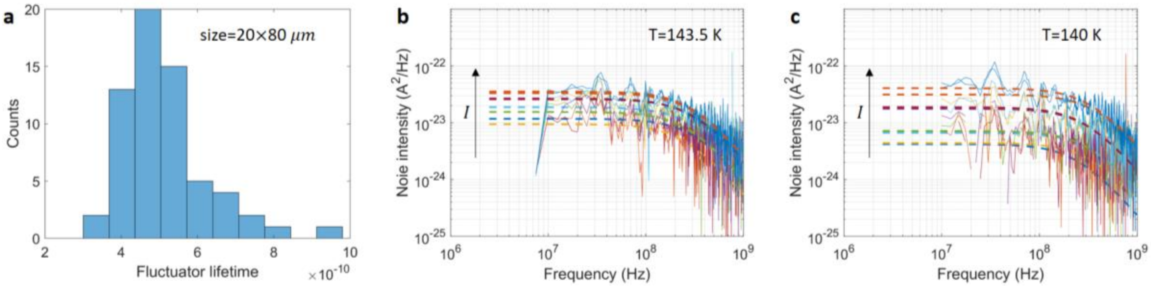

Figure 5-5: (a) Histogram of RF fluctuators characteristic times as inferred from Lorentzian noise fits. Most of the effective lifetimes obtained through fitting are around 0.5ns. (b) and (c) Two examples of Lorentzian noise fitting at T = 143.5K and 140K. The arrow indicates the increase of bias current.

5.6. Evolution of the low frequency spectrum across the coexistence regime

We examine in detail the evolution of the noise spectra as a function of temperature for the 20×80 μm device in Fig. 4.6. Clear low frequency Lorentzian noise is observed when the device resistance value is around 24 kΩ, corresponding to T = 141 K, near the maximum of the noise magnitude as a function of temperature. In the percolation framework, this should be near the percolation transition for the phase coexistence regime. Near that threshold it is reasonable that individual fluctuators could have an outsized influence, as current density can be high in key narrow conductive paths [147]. At surrounding temperatures, the noise looks less like a simple Lorentian shape, and at the temperature extremes of the coexistence range the noise is more $1/f$-like.

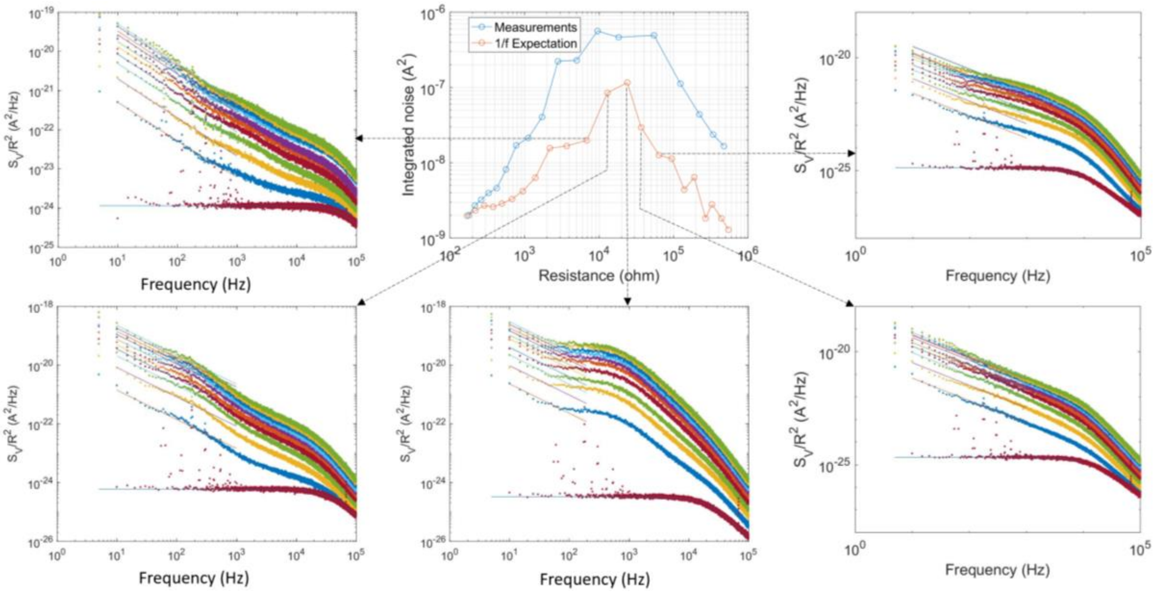

Figure 5-6: (a) The integrated noise measured by power detector and the expectation based on $1/f$ shape noise versus device resistance. (b) - (f) Low frequency spectrum at multiple resistance values. $1/f$ noise fittings are indicated by the straight lines.

5.7. Conclusion

We measured resistance noise in V_2O_3 films at both low frequency and radio frequency ranges across the mixed-phase range of the metal-insulator-transition. The variation of the noise with total resistance across the transition is quantitatively consistent with a p-noise model of 2D percolation, in which the noise arises from temporal fluctuations in the percolating fraction of the conducting medium. Lorentzian noise was observed in both low frequency and radio frequency ranges, showing the importance of individual fluctuators to the connectivity of the metallic domains. The inferred lifetime of fast fluctuators varies from 1 ns to 0.2 ns, approaching the timescale associated with the photo-induced insulator-to-metal-transition. The thermodynamics of the MIT suggest that fluctuations of entire domains between the equilibrium metallic and insulating structural phases are unlikely to be the source of the resistive noise. These noise results call for further examination of the electronic and magnetic dynamics in the mixed phase regime at the nanoscale and high frequency scales.

5.8. Supplementary information

5.8.1. noise shape dependence on the current density (electric field intensity)

We measured high frequency noise for different size devices with identical aspect ratios, from 10×40 μm to 80×320 μm. The integrated noise intensity measured by power detector and lock-in amplifier for different size devices at temperatures in the phase coexistence part of the metal-insulator-transition are shown in Figure S4.a-d. For the smallest size device with largest current density (electric field), the noise intensity is not quadratic with bias current (as would be expected for standard flicker noise due to temporal resistive fluctuations), and the noise intensity is not stable at some temperatures. As the size of devices increases and the current density decreases, the measured noise intensity becomes increasingly quadratic in the bias current. As in the low frequency measurments, the high frequency noise at finite bias current is quadratic in the current, consistent with its origination in temporally fluctuating resistive domains. However, at sufficiently large current densities, the more rapid dependence of the high frequency noise on bias current shows that the current itself is driving domain dynamics, rather than acting as a non-perturbative probe of the resistive landscape.

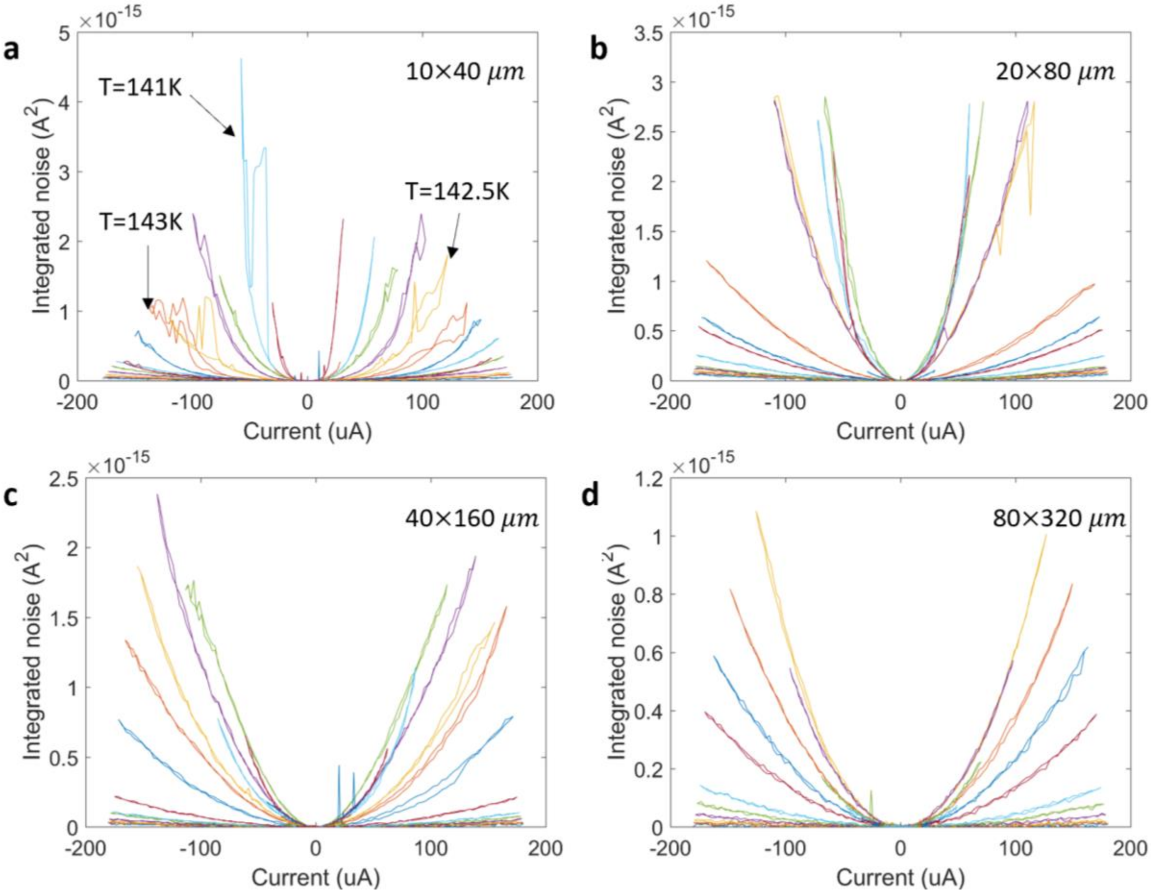

Figure 5-7. (a) - (d) High frequency (225MHz – 580MHz) integrated noise intensity for different size devices. The noise intensity versus current become more quadratic and stable as the size of device increases and the current density (electric field intensity) decreases. This indicates some electric field-induced change to the properties of the resistance fluctuations at the largest fields/highest current densities.

5.8.2. V_2O_3 metal insulator transition and IV curves for other size devices

We measured the metal insulator transition and IV curves for different size devices. The 20×80 μm device is already shown in the manuscript. The other three size devices are shown in Figure A2.a-f. The different sizes devices show similar metal insulator transition at same temperature range. However, in relatively large voltage range, the smallest device shows a nonlinear IV curve, because of the comparatively larger electric field and current density. This implies the bias conditions can induce dynamical changes in the state of the film.

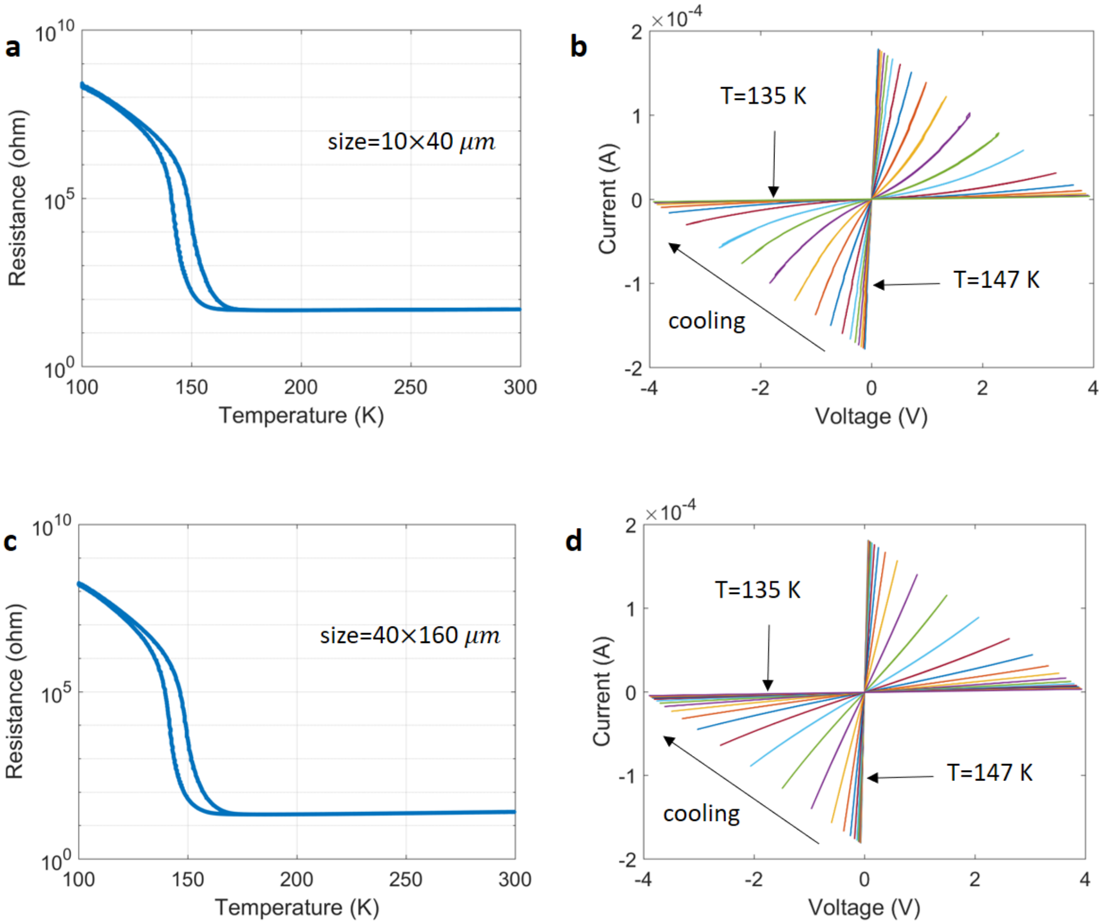

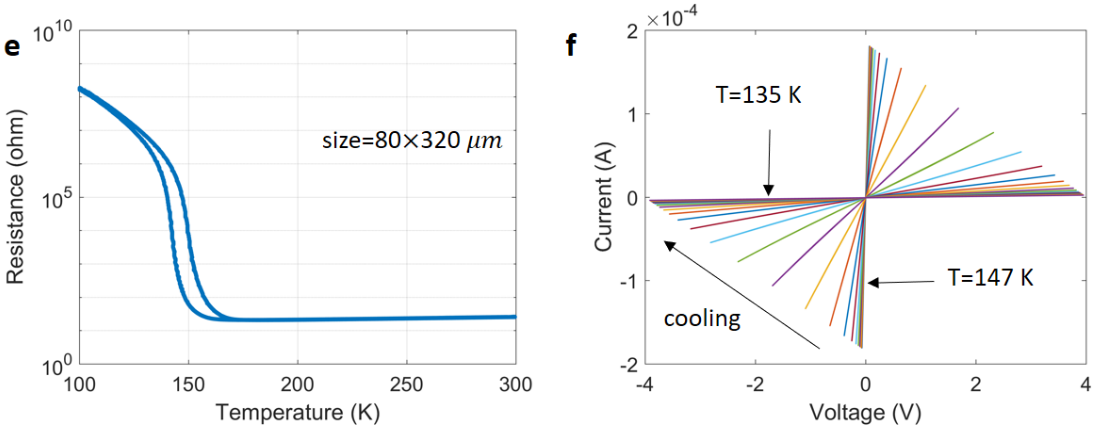

Figure 5-8. (a) Resistance versus temperature of size 10×40 μm device. (b) IV curves for the temperature range where the noise measurements were taken. The smallest size device shows nonlinear IV curves at higher voltage range. (b) - (f) Resistance versus temperature and IV curves for other larger sizes devices. The IV curves are more linear as device size increases.

Chapter 6

Shot noise indicates the lack of quasiparticles in a strange metal

This Chapter is largely based on the recently published manuscript [148]. Strange metals are non-Fermi liquids that most famously exhibit an electrical resistivity linear in temperature, *T*, at low temperatures [149], a response that has been reported across many materials families, including cuprate [150–152] and pnictide [153] superconductors, ruthenates [154], heavy fermion metals [126,155,156], and twisted bilayer graphene [157]. Strange metal properties typically arise at finite temperature above a quantum critical point (QCP), often in proximity to antiferromagnetic order [158]. There are two broad classes of theories on metallic QCPs. Within the standard Landau approach of order parameter fluctuations, quasiparticles retain their integrity [159,160]. In approaches beyond the Landau framework [161–164], by contrast, no long-lived quasiparticles are expected to remain. Thus, determining the nature of the low energy current-carrying excitations is an important means to elucidate strange metals near QCPs.

How can we determine whether the current carriers in strange metals are quasiparticles? Shot noise in electrical conduction [42] is a unique probe of mesoscopic systems in which the current noise, $S_I = \langle (I - \langle I \rangle)^2 \rangle$, in a system driven out of equilibrium reveals the discrete nature of the charge-carrying excitations. The Fano factor, F, gives the ratio between the measured noise S_I and $2eI$, the expectation for Poissonian transport of ordinary "granular" charge carriers of magnitude e with an average current I. Shot noise has revealed fractionalization of charge in the fractional quantum Hall liquid [53,54], fractional effective charges in quantum dot Kondo systems [165,166], and pairing in superconducting nanostructures in the normal state [45,52]. A lack of granular quasiparticles would naively be expected to suppress shot noise, since flow of a continuous fluid should have no fluctuations.

Despite their ubiquity, strange metals have yet to be examined through shot noise measurements for several technical reasons, and only few relevant theoretical predictions exist [167,168]. In many materials strange metallicity is cut off at low temperatures by the onset of superconductivity, which complicates matters because shot noise measurements also require an electrical bias eV large compared to the thermal scale $k_\mathrm{B}T$ to distinguish from thermal noise. Tunneling transport into a strange metal faces the challenge that only discrete, individual electrons can be added or removed, likely leading to noise dominated by single-electron effects. Fortunately shot noise can be measured *within* a material using a diffusive mesoscopic wire, though this requires nanofabrication of such structures without damaging electronic properties, a major challenge for many materials.

We have successfully made mesoscopic wires for noise measurements from epitaxial films of the heavy fermion material $YbRh_2Si_2$, a particularly well-defined strange metal [118,156]. $YbRh_2Si_2$ has a zero-temperature field-induced continuous quantum phase transition from a low-field antiferromagnetic heavy Fermi liquid metal to a paramagnetic one. The Hall effect displays a rapid isothermal crossover that extrapolates to a jump at the QCP in the zero-temperature limit, providing evidence for a sudden reconstruction of the Fermi surface across the QCP and an associated change in the nature of the quasiparticles between the two phases [169], as expected in the Kondo destruction description [161–163] for a beyond-Landau QCP. At finite temperatures, a quantum critical fan of strange metallicity extends over a broad range of temperature and field [118,129]. Recent time-domain THz transmission measurements [133] of optical conductivity of epitaxial films of $YbRh_2Si_2$ reveal the presence of quantum critical charge fluctuations, supporting the Kondo destruction picture in this system.

Measuring shot noise in $YbRh_2Si_2$ wires directly examines how current flows in a system thought to lack discrete charge excitations, and there are clear predictions in Fermi liquids for comparison. We report measurements of shot noise in mesoscopic wires patterned from epitaxial films of $YbRh_2Si_2$, examined in the strange metal regime below 10 K, where phonon scattering is not expected to be relevant to the conductivity. The measured noise is found to be far smaller than both weak- and strong electron-

electron scattering expectations for Fermi liquids, and actual measurements performed on a gold nanowire for comparison. Furthermore, the electron-phonon coupling determined experimentally using long $YbRh_2Si_2$ nanowires rules out strong electron-phonon scattering as a noise suppression mechanism. Therefore, the suppressed shot noise is evidence that current-carrying excitations in this strange metal defy a quasiparticle description.

6.1. Device Fabrication

6.1.1. Film growth

$YbRh_2Si_2$ thin films were grown by our collaborator in the setup of Prof Silke Paschen at TU Wien on Ge (001) wafers in a RIBER C21 EB 200 molecular beam epitaxy (MBE) system, using a high-temperature (RIBER HT 12) cell for Rh, a medium high-temperature (MHT) cell for the Si, and a dual zone low-temperature (DZ-MM) cell for Yb. The temperature-dependent growth rates for Rh and Si were determined with elemental films, that of Yb with a flux gauge. With these calibrations, the cell temperatures were set for stoichiometric growth. A series of films was grown at different rates. The film selected for the present study was closest to the ideal 1:2:2 stoichiometry according to energy-dispersive X-ray spectroscopy (EDX) measurements, showed no foreign phase in x-ray diffraction, had a smooth surface in atomic force microscopy (AFM), and the highest residual resistance ratio [170]. The quality is comparable to that of the films studied in ref [133], which were grown with electron beam evaporators instead of Knudsen cells for Rh and Si.

6.1.2. Reactive ion etch

To make nanodevices from the film, we need to etch away part of film to define the device geometry. There two common types of etching people usually use: 1. Wet etching: use chemicals solution that selective react with the sample you want to etch. The advantage of wet etching is relatively fast and cheap, and its isotropic etching property make it possible to fabricate some special structure device that requires undercut. However, wet etching has a big defect that it is hard to control the etch rate and depth, making it not practical to fabricate nano devices. 2. Dry etch: there are three major instruments to perform dry etch, reactive ion etch(RIE), ion milling and focused ion beam(FIB). RIE uses specific gas and electron magnetic field to generate plasma to etch samples, ion milling use Ar^+ beam to physically etch the sample, and FIB works similarly with ion milling but using a different ion Ga^+, higher ion energy, and a more focused beam. Among the three dry etch methods, RIE works in higher pressure and lower accelerating voltage(below 500V), FIB has highest energy ion up to 30 KeV, and Ar ion milling lies in the middle. In most cases, RIE is relatively gentle and leave less edge damage to your sample. The RIE instrument we used is an Oxford Plasmalab System 100/ICP 180 which is known as ICP-RIE. Figure 6-1 shows the mechanism of a ICP-RIE. ICP here is abbreviation of inductively coupled plasma. Compared to traditional RIE, ICP-RIE has a separate RF power apply current to a coil at the top part of chamber to generate switch magnetic field and plasma, then this plasma will be accelerated by electric field generated by the other RF power source.

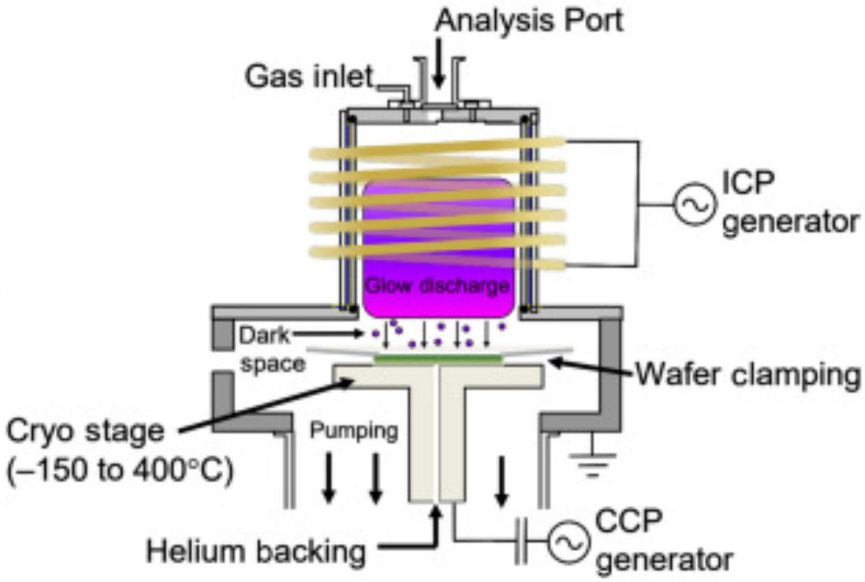

Figure 6-1 [171]. Diagram of ICP-RIE. This instrument has two RF power, one is used to generate plasma and the other used to generate accelarating electric field.

Because of the robustness of $YbRh_2Si_2$ film, it is difficult to find a proper chemical etchant or reactive ion etch (RIE) recipe to etch the $YbRh_2Si_2$ selectively without damaging the Ge substrate; most etchants remove the Ge faster than the $YbRh_2Si_2$. After working with SF_6, we choose to use pure argon plasma in a RIE system to etch the film through physical sputtering, which has a similar etch rate for both the $YbRh_2Si_2$ film and the substrate. The etch rate of the film under argon plasma depends on the radio frequency (RF) and inductively coupled plasma (ICP) power, but also heavily depends on the pressure. Lower pressure means lower scattering probability of argon atoms before hitting the film surface, and results in higher argon atom energy. We found that if the working pressure is comparatively high (such as 20 mtorr for usual RIE recipe), there will be many sharp islands left on the etched surface, most likely because the low energy argon atoms only destroy the surface structure, but do not effectively remove the $YbRh_2Si_2$ material. If the working pressure is too low, there is insufficient plasma density to etch the film. After trials with different pressures, we found that the following recipe works well in our Oxford Plasmalab System 100/ICP 180 etcher: pressure 4 mtorr, argon gas flow rate 35 sccm, RF power 185 W (corresponding DC voltage 400 V), ICP power 700 W. The edge of a region of film following 1 minute RIE etching in these conditions is shown in an atomic force microscopy (AFM) in Figure 6-2.A with a line-cut topograph in Figure 6-22.B. PMMA 950 was used as the protective cover of the unetched region and removed by warm acetone with brief sonication, and low energy oxygen plasma. The AFM scan image shows the etch rate using this recipe is about 47.5 nm per minutes.

It is worth noting that the etching rate and aspect ratio can change with film properties, recipe and instrument conditions, we attach more RIE etching test results in the Appendix.

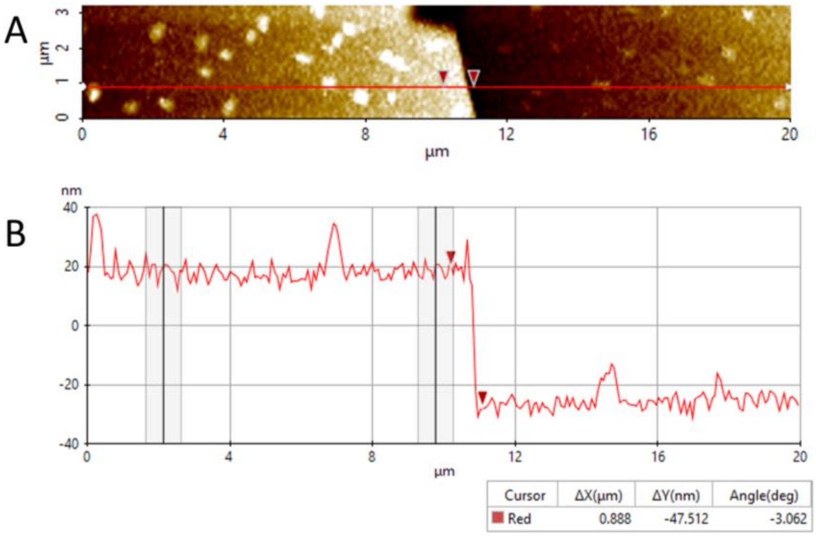

Cursor	ΔX(μm)	ΔY(nm)	Angle(deg)
🟥 Red	0.888	-47.512	-3.062

Figure 6-2 Ar RIE etch rate test on $YbRh_2Si_2$ film. (A) Surface topograph scanned by AFM on edge of argon etched film in a 3 μm × 20 μm area. PMMA was used as protective layer and removed by acetone. Red horizontal line indicates the position of the side view in (B), and red triangles are the two positions used to calculate etching rate. (B) Thickness change of etched film under one minute argon reactive ion etching. Two gray windows represent the two ranges on protected film to flatten the tilted surface and correct corresponding error. The AFM surface topograph shows the film was etched by about 47.5 nm in one minute.

6.1.3. Nanowire fabrication

The devices are made by several steps of e-beam lithography, sputtering, and etching. The steps are summarized in Figure 6-3 A-D. The first row displays the view from top, and second row shows the cross-sectional view of the same steps. In first step, standard e-beam lithography using an Elionix ELS-G100 lithography tool on PMMA 950/495 double layer resist defines the patterns for the two source and drain gold contacts. 200 nm thickness gold contacts pads and a 60 nm Cr hard mask layer for RIE etch are deposited via AJA ATC Orion Sputtering System, followed by liftoff. In the second step, another round of e-beam lithography and sputtering deposition makes the Cr nanowire that serves as the etch mask for the nanowire device. Two minutes of argon RIE under the conditions described above etch away the exposed $YbRh_2Si_2$ film. Finally, the Cr masks are removed by soaking in 70°C 37% HCl solution, leaving the gold pads and protected $YbRh_2Si_2$ nano wires. Wire bonding is used to make connection from the device to our customized probe. A small misalignment in the first patterning step left the edges of the gold pads exposed to RIE, causing some edge roughness, but this does not affect our measurements, because the gold pads close to the nanowires are protected well by the Cr nano wire mask in the second patterning step.

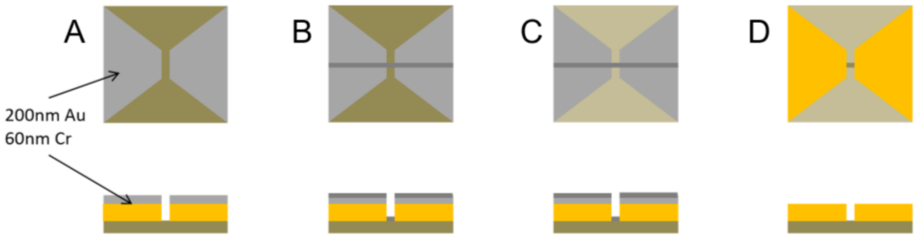

Figure 6-3. (A) Two 200 nm gold pads and 60 nm Cr hard mask on top are patterned by ebeam lithography and deposited using sputtering. Leaving small gap in middle for nano wires. The diagram on bottom shows the side view of same process. Film, gold pads and Cr masks are indicated by dark brown, yellow and light gray respectively. (B) Nanowire Cr mask is made using similar process as gold pads,

shown by the dark gray line. The width of nano wires varies from 150 nm to 300 nm. (C) The uncovered part of the $YbRh_2Si_2$ film is etched in argon reactive ion etch for 2 minutes using the recipe in Sect.ion 6.1.2. The light brown color represents the etched part, leaving only Ge substrate. (D) The Cr hard masks for gold pads and nanowires are removed by warm (70°C) concentrated HCl solution (37%), leaving only golds contact pads and $YbRh_2Si_2$ nano wires.

6.2. Device characterization

The films are patterned into nanowires using the method in section 6.1, and scanning electron microscope images are shown in Figure 6-4 (A) and (B). The nanowire shown is 60 nm thick, 660 nm long, and 240 nm in width. Thick source and drain contact pads ensure that the dominant voltage measured under bias is across the nanowire, and act as thermal sinks [72]. An important concern in fabricating nanostructures from strongly correlated materials is that the patterning process does not alter the underlying physics. As shown in Figure 6-4 (C), the normalized resistance $R(T)$ of the nanowire closely matches that of the unpatterned film, including a dominant linear-in-T dependence at low temperatures. Similarly, in Figure 6-4 (D) the normalized magnetoresistance (field in-plane, perpendicular to the current) in the nanowire is nearly identical to that of the unpatterned film, showing that the fabrication process did not alter the material's properties. This consistency also shows that the total R is dominated by the wire, as the large contacts are coated in thick gold and would not exhibit such a magnetoresistance. Three nanowires patterned from this same film all show essentially identical transport and noise properties.

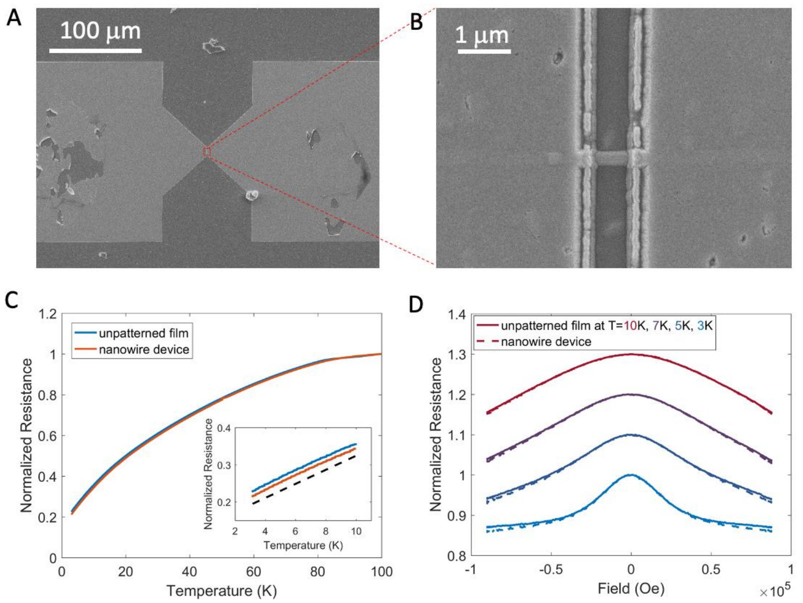

Figure 6-4. $YbRh_2Si_2$ nanowire device preparation and characterization. (A) $YbRh_2Si_2$ nanowire between two large area, thick sputtered Au contacts on top of the unpatterned $YbRh_2Si_2$ film, deposited to ensure that the measured voltage is dominated by the nanowire. (B) Higher magnification view. Sample fabrication is discussed in detail in SI. (C) Normalized resistance as a function of temperature for both the unpatterned film and the etched nanowire, showing linear-in-T resistivity in the low temperature limit, as seen previously [133]. (D) Normalized resistance as a function of in-plane magnetic field for both the unpatterned MBE film and the etched nanowire (B oriented transverse to the nanowire), with curves shifted vertically for clarity. The nearly identical response between nanowire and

unpatterned film confirms that patterning did not substantially alter the electronic properties of the epitaxial $YbRh_2Si_2$ material, and that resistance is dominated by the wire.

6.3. Shot noise measurement in nanowire

A current bias is applied to the device via a heavily filtered voltage source and ballast resistors. Using a custom probe, the voltage across the device is measured through two parallel sets of amplifiers and a high-speed data acquisition system. The time-series data are cross-correlated and Fourier transformed to yield the voltage noise S_V across the device, with the correlation mitigating the amplifier input noise. Figure 6-5 (A) shows the variation of the differential resistance as a function of bias current from T=3K to 10K. We observed non-linear resistance as bias increase, and we think it is related to both the intrinsic non-linearity and electron temperature increase. Figure 6-5 (B) gives examples of spectra at several bias currents at a base temperature of 3 K with zero bias spectrum removed. The spectra are almost flat from 300kHz to 600kHz, so the mean value in this range can be used as noise intensity. At the maximum bias currents applied, the voltage drop across the wire is several mV, a bias energy scale considerably exceeding $k_B T$ (0.25 meV at 3 K), as needed for shot noise measurements.

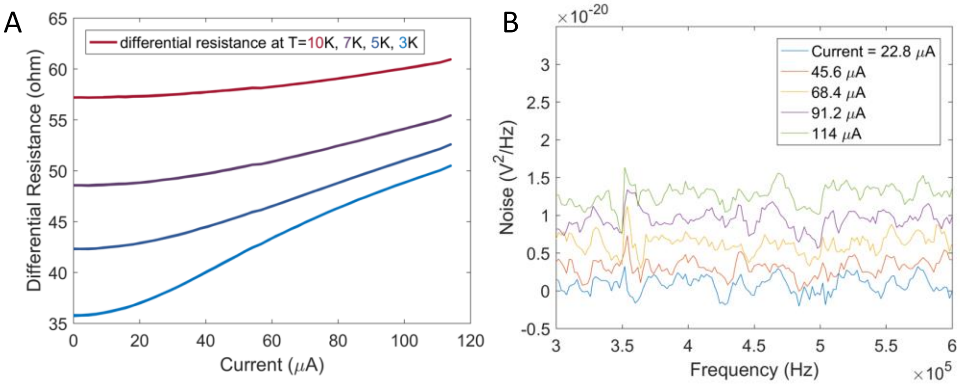

Figure 6-5. Noise characterization of a $YbRh_2Si_2$ nanowire. (A) Differential resistance dV/dI as a function of bias current at 10 K, 7 K, 5 K, and 3 K (top to bottom). Comparison with theoretical shot noise expectations requires this information. (B) Averaged voltage noise spectra (with zero-bias spectra subtracted) of a $YbRh_2Si_2$ nanowire device at different bias levels at T = 3 K, over a bandwidth between 300 kHz and 600 kHz. This spectral range is free of extrinsic features and these voltage noise spectra are used to determine the shot noise at each bias. Each spectrum shown is an average of 4500 spectra with 10 kHz bandwidth.

The shot noise with Fano factor F can be expressed as:

$$S_I = F \cdot 2eI \coth\left(\frac{eV}{2k_BT}\right) + (1-F)4k_BT\left(\frac{dV}{dI}\right)^{-1} \qquad \text{6-1}$$

This expression reduces to the Johnson-Nyquist current noise $S_{I,JN} = 4k_BT\left(\frac{dV}{dI}\right)^{-1}_{I=0}$ in the zero bias limit and becomes $S_I = F \cdot 2eI$ as expected in the high bias limit $eV \gg k_B T$. In the experiment we measure *voltage* noise, and for ease of comparison we subtract off the zero-bias Johnson-Nyquist noise, so that effective Fano factors may be estimated by fitting to the voltage-based expression for the shot noise:

$$S_V = \left(\frac{dV}{dI}\right)_I^2 \left[F \cdot 2eI \coth\left(\frac{eV}{2k_B T}\right) + (1 - F)4k_B T \left(\frac{dV}{dI}\right)_I^{-1}\right] - 4k_B T \left(\frac{dV}{dI}\right)_{I=0} \qquad 6\text{-}2$$

.

The fitting curves and theoretical shot noise with different Fano factor are shown in Figure 6-6. Based on our discussion in Chapter 1 section 1.4, the shot noise in Fermi liquid diffusive wire should be close to 1/3 if device length L is shorter than electron-electron scattering length L_{ee} or $\sqrt{3}/4$ if device length L is longer than L_{ee}, however, we observed the measured voltage noise is far below the theoretical expectations for shot noise in a diffusive nanowire of a Fermi liquid even in the weak electron-electron scattering limit. In the Fermi-liquid theory framework with well-defined quasiparticles, the only reason to greatly suppress noise to our knowledge is the electron phonon scattering, and we ruled out this in the later sections. So our results indicate the lack of well-defined quasiparticles.

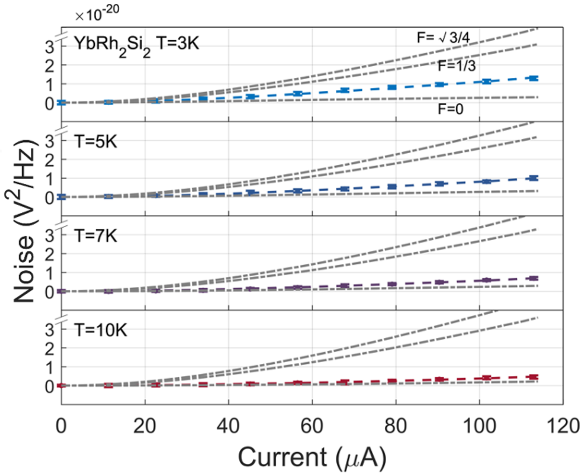

Figure 6-6. Noise vs. bias current for a $YbRh_2Si_2$ wire at various temperatures, with fits to equation above to extract effective Fano factors(fitted values shown in section 6.7), for temperatures 10 K, 7 K, 5 K, and 3 K from bottom to top. Error bars are the standard error from 15 repeated bias-sweep measurements. Also shown for illustrative purposes are expectations for $F = \frac{\sqrt{3}}{4}, \frac{1}{3}$ and 0 (dot-dashed curves top to bottom, respectively) calculated using the measured differential resistance at each temperature. At all temperatures, the measured voltage noise is far below the theoretical expectations for shot noise in a diffusive nanowire of a Fermi liquid even in the weak electron-electron scattering limit.

6.4. Comparison with gold nanowires

To directly compare the shot noise in $YbRh_2Si_2$ nanowire with shot noise in Fermi liquid nanowire, we fabricated gold nanowire using standard e-beam lithography ELS-G100 to design 100 nm wide wire pattern on double layers PMMA(950/495) coated

SiO2/Si chip, and using evaporator to deposit 18 nm gold/1nm Ti adhesion leary, finally remove PMMA in lift-off process. The two 200 nm thick gold/2nm Ti adhesion layer pads were made using same method, leaving about 900 nm gap as the nanowire length. The SEM image of the structure is shown in inset of Figure 6-7 (A). Resistance dependence on temperature is shown in Figure 6-7 (A), it decreases as temperature goes down and saturates quadratically below 10K. The tiny steps on the curves are due to the temperature delay between the base temperature and real temperature of devices. To guarantee the temperature get balanced, we always wait for 30 minutes at each temperature points before we start taking noise measurements. The voltage noise power values and Fano factors are much closer to the conventional Fermi liquid expectations, as shown in Figure 6-7 (C) and (D). The slight decrease in Fano factor starting at 10 K and above is expected to be a consequence of electron-phonon scattering. The suppressed shot noise in $YbRh_2Si_2$ nanowire compared with the 1/3 shot noise in gold nanowire tell us two things. First, our noise measurement system can correctly measure shot noise in nanowire as seen in the gold sample; second, there is something special making the shot noise in the strange metal $YbRh_2Si_2$ nanowire much smaller, and this indicates the lack of well-defined quasiparticles.

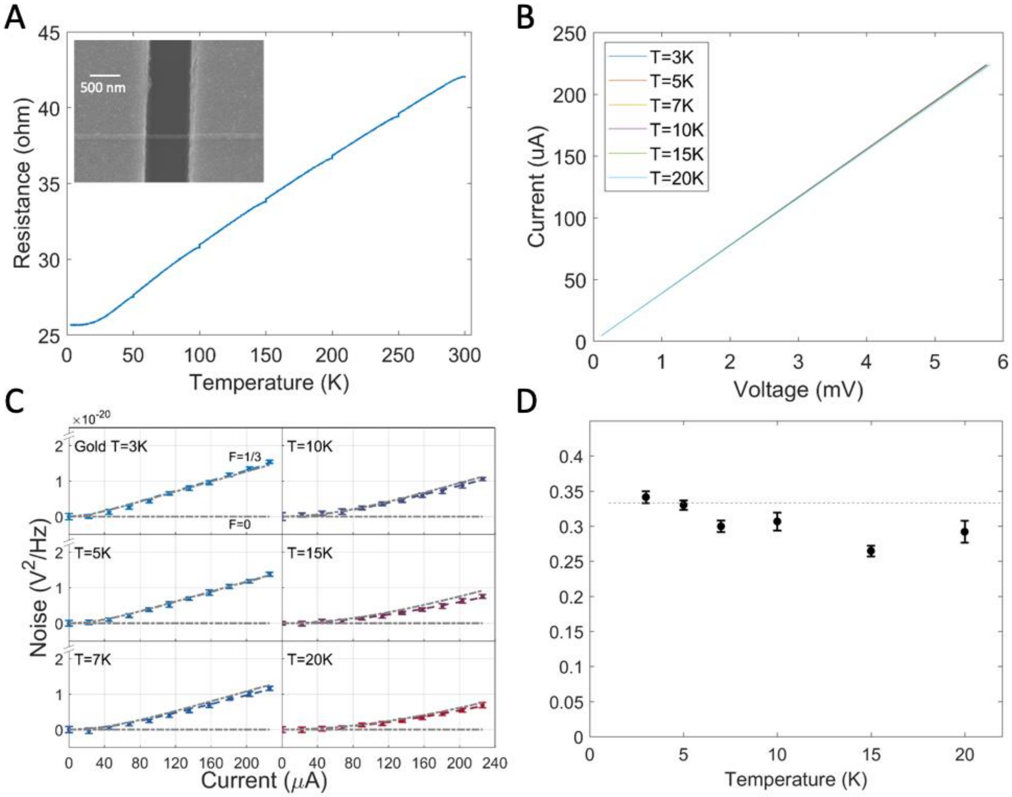

Figure 6-7. shot noise measurement in a gold nanowire. (A) Resistance dependence on temperature of the Au wire (shown in an electromicrograph in the inset). The resistance decreases with decreasing temperature and saturates quadratically below 10 K. (B) Representative *IV* characteristics of the Au nanowire at temperatures from 3 K to 20 K. (C) Noise vs. bias current at various temperatures (3 K, 5 K, 7 K, 10 K, 15 K, 20 K) plotted as in Fig. 3B. (D) The Fano factor of the gold nanowire decreases slightly as temperature increase from 3 K to 20 K, likely due to the onset of electron-phonon scattering at the higher temperatures, and remains much larger than that of the $YbRh_2Si_2$ devices across the whole temperature range.

6.5. Additional data

We have performed measurements on two additional nanowires with virtually identical results. Figure 6-8 is an additional data set on another wire fabricated on the same chip as the one in section 6.3.

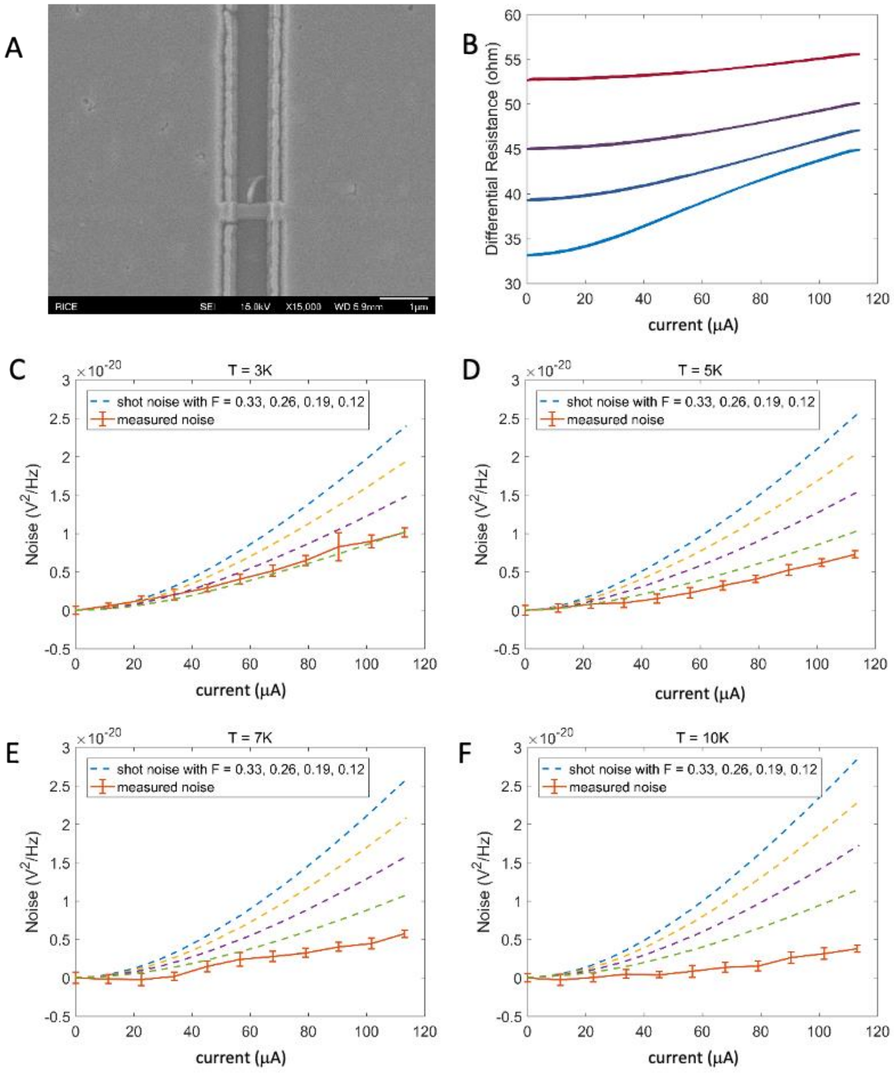

Figure 6-8. Additional data on another $YbRh_2Si_2$ nano wire device. (A) SEM image of the device. The nano wire in middle is connected by the two large gold pads on the

two sides. (B) Differential resistance dV/dI dependence on bias current at multiple temperatures. The curves from top to bottom are for 10 K, 7 K, 5 K, and 3 K respectively. (C)-(F) Noise vs. bias current at various temperatures (3 K, 5 K, 7 K, 10 K), with comparison dashed lines showing expectations for particular Fano factors. The orange color error bars are from 15 repeated measurements data and connected through straight guide lines. The measured noise remains far below theoretical expectations for a diffusive nanowire of a conventional Fermi liquid at all temperature.

While the differential resistance changes with increasing in-plane magnetic field, as shown in Figure 6-4 (D), apart from this there is no significant change in the noise response. In Figure 6-9 are data on the device in Figure 6-8 taken in an in-plane field of 9 T.

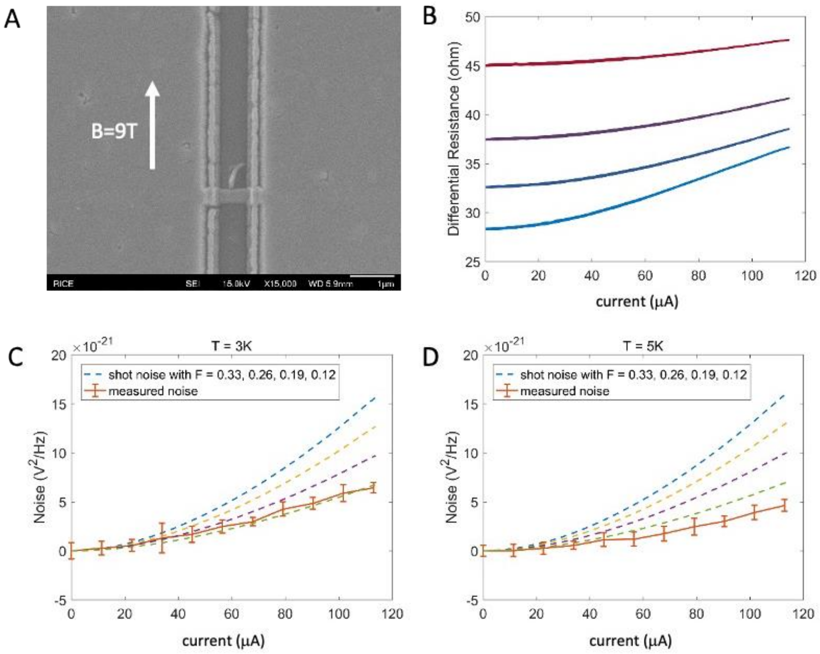

Figure 6-9. Additional data on another $YbRh_2Si_2$ nano wire device at high magnetic field. (A) SEM image of the device indicating the direction of magnetic field. (B) Differential resistance dV/dI dependence on bias current at multiple temperatures. The curves from top to bottom are for 10 K, 7 K, 5 K, and 3 K respectively. (C), (D) Noise vs. bias current at various temperatures 3 K and 5 K. The data are plotted in the same way as zero magnetic field, with comparison dashed lines showing expectations for particular Fano factors and orange color error bars showing the experiment data. The noise intensity shows same dependence on bias and temperature as in the data in Fig. 3A, except for a small difference in overall value due to the slightly varied differential resistance.

6.6. Phonon contribution estimation using noise measurement in long narrow wire

Electron-phonon coupling effects can suppress the noise in the usual Fermi Liquid quasiparticle scenario. $YbRh_2Si_2$ has a Debye temperature more than twice that of gold [172], which already makes that scenario unlikely in the present case. To experimently rule out this possibility, we need to design further stucture. Here we estimate the phonon contribution use the method discussed in subsection 1.4.3.

In a Fermi Liquid, strong electron-phonon scattering can suppress shot noise by anchoring the quasiparticle distribution function to the temperature of the lattice. As shown by Henny et al. in Ref [72], the electron-phonon coupling strength Γ can be determined experimentally by measuring the noise as a function of bias current in a wire much longer than the electron-phonon scattering lengthscale. In this limit, the electron temperature profile within the wire is modeled by the equation:

$$\frac{\pi^2}{6}\frac{d^2T_e^2}{dx^2} = -\left(\frac{eE}{k_B}\right)^2 + \Gamma\left(T_e^5 - T_{ph}^5\right) \tag{6-3}$$

where T_e is the local electron temperature, x the position on the nanowire, E the local electric field, and T_{ph} the phonon temperature, which equals the base temperature. The model is derived assuming that all the Joule heating power within a small segment of wire is conducted away via electronic thermal conductivity or lost to the phonons. Accounting for the measured temperature dependence of the electrical conductivity and assuming the electrical conductivity only depends on local temperature complicates the expression slightly to

$$\frac{\pi^2}{6}\frac{d^2T_e^2}{dx^2}-\frac{\pi^2T_e}{3r}\frac{dr}{dT_e}\left(\frac{dT_e}{dx}\right)^2=-\left(\frac{eE}{k_B}\right)^2+\Gamma\left(T_e^5-T_{ph}^5\right) \tag{6-4}$$

The resulting model may be solved numerically to find a consistent $T_e(x)$ for a given bias current. Given this, the integrated thermal noise may be computed by adding up the contributions of each segment of wire: $S_V=\int 4k_Br\big(T_e(x)\big)T_e(x)dx$, where r is the local resistance per unit length.

Figure 6-10(A) shows the measured voltage noise vs. bias current data at 3 K, 5 K, and 7 K for a 30 μm long $YbRh_2Si_2$ wire of comparable width to the short nanowires, fabricated through the same process. For a long nanowire with a length much longer than the electron-phonon scattering length, thermal transport is dominated by electron-phonon coupling. Following the method of Henny et al. in Ref [72], we numerically solved the equation $\left(\frac{eE(x)}{k_B}\right)^2=\Gamma\left(T_e(x)^5-T_{ph}^5\right)$. At each temperature the data can be fit extremely well with a single Γ, the values of which are 9×10^9 $K^{-3}m^{-2}$, 9.5×10^9 $K^{-3}m^{-2}$, and 10 ×

10^9 $K^{-3}m^{-2}$, for temperatures 3 K, 5 K, and 7 K respectively. These values are of the same order as the reported coupling for gold, 5×10^9 $K^{-3}m^{-2}$.

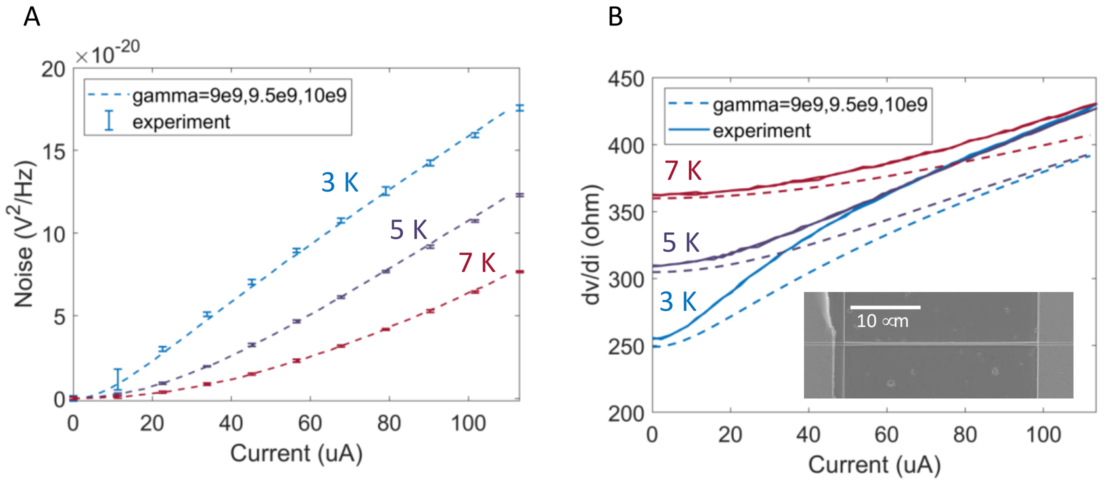

Figure 6-10. Inferring the electron-phonon coupling. (A) Voltage noise as a function of bias current in a 30 μm long $YbRh_2Si_2$ wire, of comparable width to the nanowires used in the main experiment. The dashed curves are fits to the model mentioned above, where the fitted electron-phonon coupling parameters are $\Gamma = 9 \times 10^9$ $K^{-3}m^{-2}$, 9.5×10^9 $K^{-3}m^{-2}$, and 10×10^9 $K^{-3}m^{-2}$ at T=3 K, 5 K, and 7 K, respectively. (B) Using the temperature profiles computed from the model with those values of Γ, we compare the computed $\frac{dV}{dI}$ as a function of bias (dashed lines) with the measured data (solid lines), showing good qualitative agreement while implying some intrinsic non-Ohmic response in the material. The inferred Γ values are of the same order as in gold, thus demonstrating that there is no greatly enhanced electron-phonon coupling in $YbRh_2Si_2$.

With these measured values for Γ, we can estimate the phonon contribution in the short nanowire. We reach conclusion that electron-phonon coupling cannot be responsible for the observed shot noise suppression using two ways.

First, we consider what the expected noise *would* be if there were strong electron-electron scattering (resulting in an effective $T_e(x)$) as well as electron-phonon scattering consistent with the experimentally determined value for Γ in $Yb_2Rh_2Si_2$ from Figure 6-10. We compute the temperature profile $T_e(x)$ expected within the wire at 3 K and $I \approx 113\mu A$, and then compute the expected noise from $S_V = \int 4k_B r(T_e(x))T_e(x)dx$ and the expected non-Ohmic response due to that $T_e(x)$. The results are shown in Figiure 6-11(A)-(C). Using the measured Γ in $Yb_2Rh_2Si_2$, the predicted noise and the predicted non-Ohmic response are much greater than what is actually seen in the experiments. The measured noise response is not compatible with the experimentally determined electron-phonon coupling.

In our second proof-by-contradiction approach (Figure 6-11 (D)), we work backward from the measured noise to estimate what electron-phonon coupling parameter would be necessary to match the experimental noise data at each current within the quasiparticle heating model. For the suppressed noise to result from electron-phonon scattering, Γ in $Yb_2Rh_2Si_2$ would have to be 3.4×10^{11} $K^{-3}m^{-2}$, which is about 35 times higher than the experimentally measured value. Again, we find that the measured electron-phonon coupling is incompatible with electron-phonon scattering as the mechanism responsible for the suppressed noise in the short nanowires.

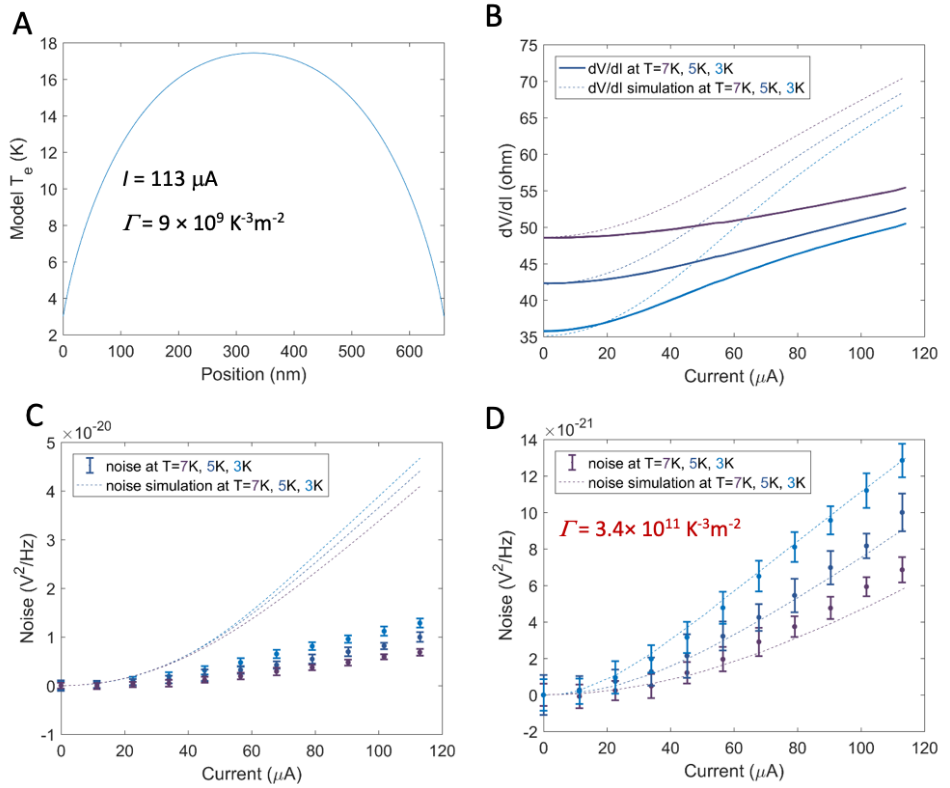

Figure 6-11. Simulations showing that the measured electron-phonon coupling cannot be the source of noise suppression. (A) The modeled local electron temperature in the wire (calculated from equation is this secton above) if we assume electronic heating and use the measured value of the electron-phonon coupling for $YbRh_2Si_2$ found from the experiments of Figure 6-10 ($\Gamma = 9 \times 10^9$ $K^{-3}m^{-2}$) at the lowest temperature and largest current. (B) The calculated differential resistance vs. bias (dashed lines) expected from the bias-dependent temperature profiles as in (A), which disagree greatly with the measured values (solid lines). (C)

The calculated noise expected from the model (dashed lines), which disagree greatly with the measured values (solid points). This shows that with the measured electron-phonon coupling Figure 6-10, in the usual quasiparticle/Fermi Liquid treatment, there should be much greater noise than what is seen in the experiment. (D) Achieving the experimentally observed noise suppression in $Yb_2Rh_2Si_2$ through electron-phonon scattering would require an electron-phonon coupling of 3.4×10^{11} $K^{-3}m^{-2}$, much larger than the measured value. Again, this shows that electron-phonon coupling cannot be responsible for the observed noise suppression.

6.7. Conclusion

To interpret these results, it is important to consider the nature of quasiparticles in terms of the single-particle spectral function and distribution functions. For a Fermi gas (i.e. in the absence of any interaction), the single-particle spectral function $A(k, \epsilon)$ at a given wavevector k is a delta function in energy ϵ at $\epsilon = E_k$, meaning that a particle excitation at (k, E_k) in the zero temperature limit is perfectly well-defined in energy and has infinite lifetime with a weight $Z = 1$. Correspondingly, the particle excitations follow the Fermi-Dirac distribution, and the Fermi surface is a perfectly sharp boundary at $T = 0$. In a Fermi liquid, the spectral function retains a peak for k near the Fermi surface, which describes a quasiparticle with a nonzero spectral weight $Z < 1$ The distribution function near the Fermi surface is smeared but still has a non-zero discontinuity at $T = 0$ [173].

In the case of the particular type of non-Fermi liquid with a complete destruction of quasiparticles, one had $Z = 0$ everywhere on the Fermi surface. With such a complete smearing of the Fermi surface, there is no discontinuity in the distribution function even at $T = 0$. In this limit, when driven by a bias that does not greatly perturb the non-FD distribution function, there are no granular quasiparticles that carry the electrical current. We can then expect a much-reduced shot noise, as we observe in the form of a Fano factor that is considerably smaller than not only the strong electron-electron scattering expectation $F = \sqrt{3}/4$ but even the weak electron-electron scattering counterpart $F = 1/3$. We highlight this contrast in Figure 6-12. For reference, when the electron spectral function is entirely featureless, the continuous electron fluid would have no shot noise $(F = 0)$. We expect our work to motivate future theoretical studies to fill the vacuum of model calculations on shot noise in strange metals.

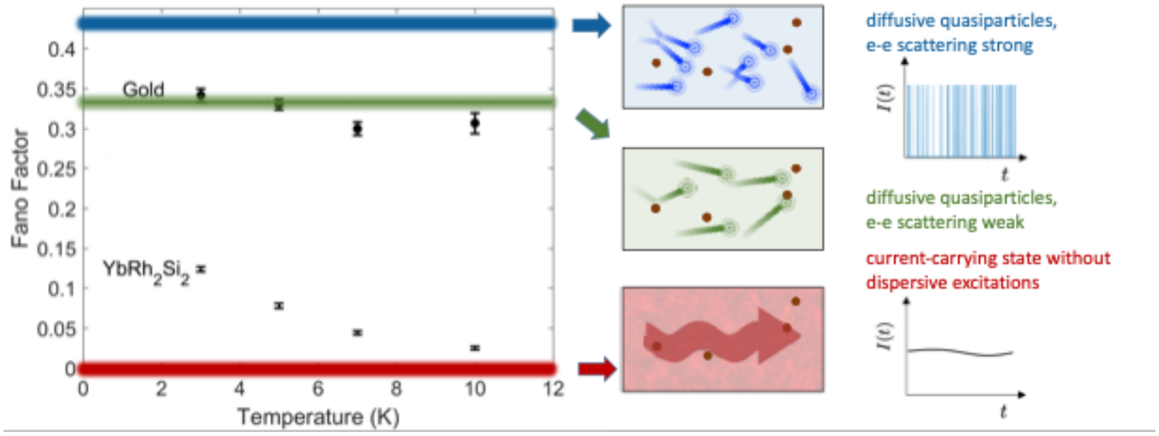

Figure 6-12. Fano factors and context for their interpretation. The main panel shows Fano factors found from fitting the data in Figure 6-6 and Figure 6-7, with error bars. In a Fermi liquid, current is carried by individual quasiparticle excitations, and the current as a function of time fluctuates with the arrival of each discrete transmitted carrier. Carriers scatter diffusively through static disorder (brown dots). When electron-electron scattering is weak (sample length $L < L_{ee}$), the expected Fano factor is $F = 1/3$ (green line), while electron-phonon coupling can suppress this at higher temperatures. When electron-electron scattering is strong ($L > L_{ee}$), the expected Fano factor is $F = \sqrt{3}/4$ (blue line). In a system without well-defined quasiparticles, charge transport is more continuous, leading to suppressed current fluctuations; in the extreme limit that electronic excitations are entirely non-dispersive, the Fano factor is expected to vanish (red line).

Shot noise is a probe that gives unique access to the discrete character of charge carriers. The suppressed noise shown in Figure 6-6 (A) and summarized in Figure 6-12 is clear evidence that current in this strange metal system is not governed by the transport of individual, granular quasiparticles. A Fano factor of zero is expected only for the most extreme case of a non-Fermi liquid, one that has a completely flat spectral function. A non-Fermi liquid that still has residual dispersive spectral features, in spite of a vanishing quasiparticle weight Z, and would thus lead to a finite Fano factor. These residual dispersive spectral features are naturally expected to somewhat sharpen as $T \rightarrow 0$, leading to the rise in F as temperature is lowered, but would never reach the $F = \sqrt{3}/4$ expectation for a strongly correlated Fermi liquid (where Z is finite).

While scattering techniques show incoherent, non-quasiparticle electronic response as a diffuse continuum across $(\boldsymbol{k}, \epsilon)$, shot noise specifically targets the current-carrying excitations. The shot noise probes both the equilibrium non-Fermi liquid distribution function and its nonequilibrium evolution when perturbed by the difference in source and drain chemical potentials. In Fermi liquids, this approach has given insights into inelastic electron-electron scattering and the evolution of the nonequilibrium distribution function. This technique will provide crucial experimental constraints on such processes in strange metals, physics that has a paucity of theoretical treatment thus far. Moreover, strange metallicity as inferred from the resistivity is observed across many systems with quite disparate underlying microscopic physics (*2-8, 10, 28*). Shot noise provides an opportunity to test the extent to which these apparently similar strange metals can fit within a single paradigm.

6.8. Supplementary information

6.8.1. Thermal noise correction for Non-linearity in $YbRh_2Si_2$ nanowire

Experimentally, the noise in the $YbRh_2Si_2$ nanowires is unequivocally suppressed relative to Fermi Liquid expectations. When attempting to extract an effective Fano factor, it is important to consider whether non-Ohmic response could be influencing the analysis. There are a number of approaches that try to address the issue of thermal noise in an intrinsically non-Ohmic device (e.g. [174,175]). The situation is particularly challenging in a mesoscopic device driven out of equilibrium, where it is not generally possible to cleanly separate the measured noise into contributions that are purely thermal and purely shot noise.

For a passive device without large reactive contributions, the typical approach in assessing the thermal noise is to consider a term with a nonlinear correction:

$$S_{V,Th}(I) = 4k_B T\left(\left(\frac{dV}{dI}\right)_I + \frac{1}{2}I\left(\frac{d^2V}{dI^2}\right)_I\right) \tag{6-5}$$

If we take the conservative approach and assume that *all* of the observed nonlinearity in Figure 6-5 (A) is intrinsic and not related to local electron temperature changes, we can analyze the data of Figure 6-6 (A) with this approach, as shown in Figure 6-13. The suppression of the measured noise below the Fermi Liquid expectations is unambiguous, as pointed out in the main text, and the difference between the inferred Fano factors with and without the nonlinearity correction are small.

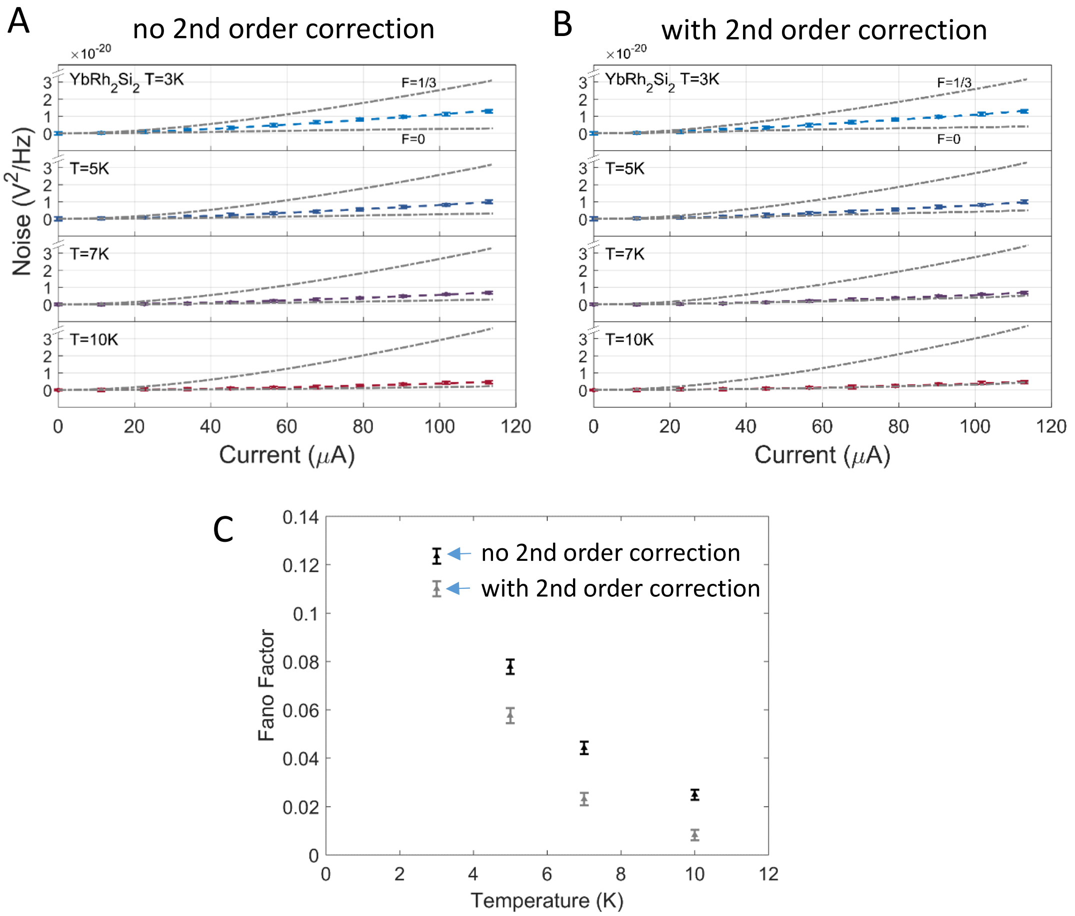

Figure 6-13. Noise vs. bias current with two different analyses (curves shifted vertically for clarity). The noise data are identical between the two panels and clearly fall far below the $F = \frac{1}{3}$ Fermi Liquid expectations. (a) The theory curves in this panel including the fits to the data are using the expression from the paper, $S_V = \left(\frac{dV}{dI}\right)_I^2 \left[F \cdot 2eI \coth\left(\frac{eV}{2k_BT}\right) + (1-F)4k_BT\left(\frac{dV}{dI}\right)_I^{-1}\right] - 4k_BT\left(\frac{dV}{dI}\right)_{I=0}$. (b) The theory curves in this panel including fits to the data are using an expression based on the second-order correction from M. S. Gupta, *Proc. IEEE* **70**, 788-804 (1982), $S_V = \left(\frac{dV}{dI}\right)_I^2 \left[F \cdot 2eI \coth\left(\frac{eV}{2k_BT}\right) + (1-F)\left(4k_BT\left(\frac{dV}{dI}\right)_I^{-1} + 2k_BTI\left(\frac{d^2V}{dI^2}\right)_I / \left(\frac{dV}{dI}\right)_I^2\right)\right] -$

$4k_BT\left(\frac{dV}{dI}\right)_{I=0}$. (c) Comparison of fitted Fano factors from (a) in black and (b) in gray. This shows that including a thermal noise correction that assumes an intrinsic non-Ohmic response *lowers* the inferred Fano factors by about 0.01 to 0.02.

6.8.2. One theoretical model for current fluctuations in a quantum critical metal

One explicit discussion of nonequilibrium noise in a quantum critical metal exists in the literature [167,168]. The applicability of the model in question, however, is limited and not necessarily well-suited to this experiment. That model considers an entirely different quantum critical metal, one associated with the Bose-Hubbard model of the superconductor-insulator transition. The approach is based on holography and maps between the nonequilibrium current fluctuations in the quantum critical metal and Hawking radiation within an effective black hole model. The result is an expression that interpolates between Johnson-Nyquist noise at zero bias and shot noise that scales like $\sqrt{V}$ at high bias, $S_I = 4k_B\,T^*/\left(\frac{dV}{dI}\right)$, where $\pi k_B T^* = [(\pi k_B T)^4 + \hbar^2 c_0^2 e^2 E^2]^{1/4}$, c_0 is a characteristic velocity, and $E = V/L$ is the driving electric field along the device. It is worth noting that this model has issues when extrapolated to the zero-temperature limit, as the predicted Fano factor diverges like $E^{-1/2}$ when approaching zero bias.

While this model is for an entirely different kind of quantum critical point, for illustrative purposes we can apply it to the measured data. Fitting the lowest temperature data best constrains c_0. We fit the 3 K noise as a function of bias current with this expression using c_0 as the only adjustable parameter. Comparing (Figure 6-14) with the measured data at higher temperatures and no further adjustable parameters shows good agreement for $c_0 = 6.6 \times 10^5$ m/s, though this may be fortuitous. It is difficult to interpret this agreement.

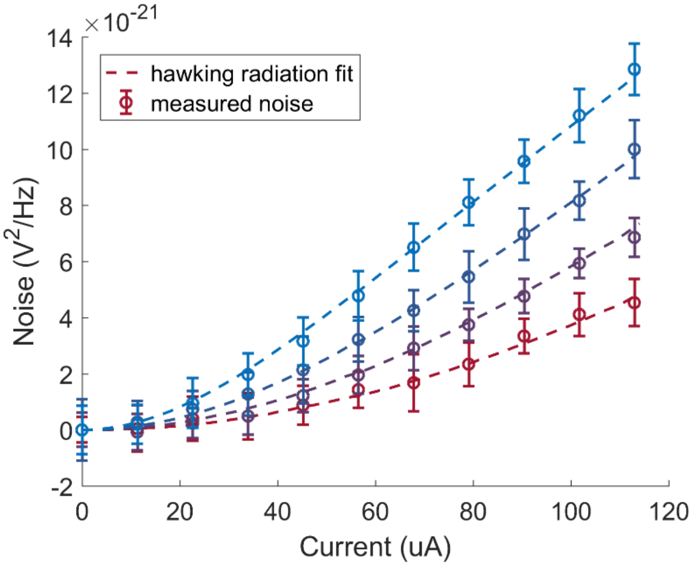

Figure 6-14. Comparison of measured noise with the example holographic treatment of noise in the strange metal.

6.8.3. Shot noise measurement in another batch $YbRh_2Si_2$ film

We performed the same measurements on wires from a newly grown $YbRh_2Si_2$ film. The RIE parameters were adjusted get well defined structures. More details about the RIE parameters tuning can be found in Section 8.3. Figure 6-15 below shows the SEM image and differential resistance data on the short nanowire. The edge is sharp compared to previous device because we deposit Ti/Au and Cr mask together using e-beam evaporator so the alignment is better.

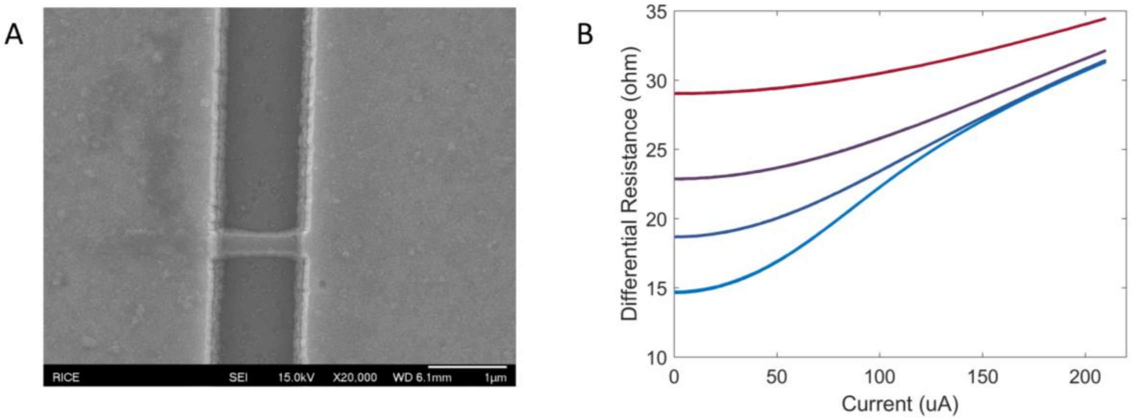

Figure 6-15. $YbRh_2Si_2$ nanowire device patterened on another film. (A). SEM image of nanowire divice connecting two large gold pads. (B). Differential resistance dV/dI as a function of bias current at 10 K, 7 K, 5 K, and 3 K (top to bottom).

Similar to previous experiments, the first thing we did is to check the basic transport properties to check if we ruined the sample, since we used different RIE parameters for etching on new batch film. The normalized resistance dependence on temperature and in-plane magnetic field is shown in Figure 6-16. We observe that the nanowire device (using different RIE parameters) for new film and the original unpatterened new film show almost identical normalized resistance depending on temperature and in-plane magnetic field. This means that our new etch parameters do not damage the film properties and resistance is dominated by the nanowires as expected.

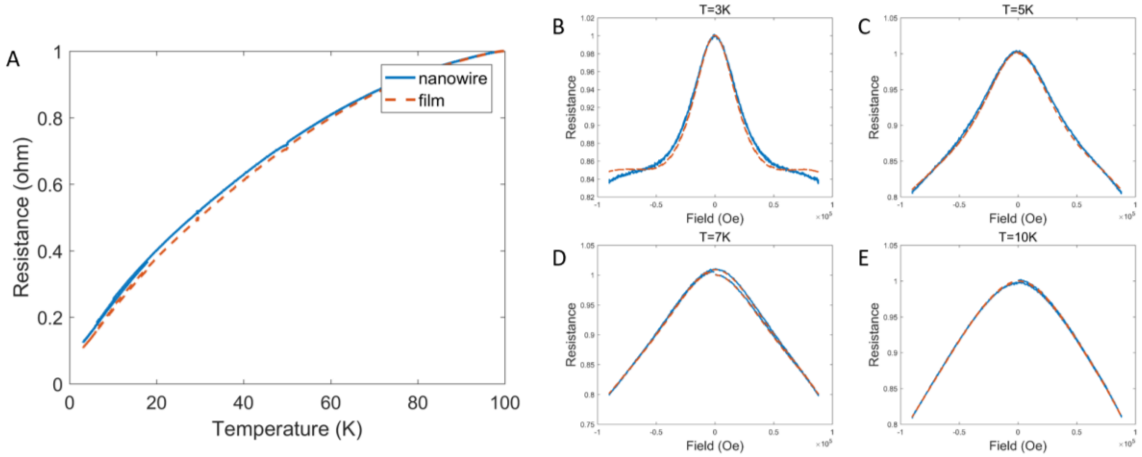

Figure 6-16. (A)Normalized resistance as a function of temperature for both the unpatterned film and the etched nanowire, showing linear-in-T resistivity in the low temperature limit. (B-E) Normalized resistance as a function of in-plane magnetic field for both the unpatterned MBE film and the etched nanowire (B oriented transverse to the nanowire) from T = 3 K to 10 K. The nearly identical response between nanowire and unpatterned film confirms that patterning did not substantially alter the electronic properties of the epitaxial $YbRh_2Si_2$ material, and that resistance is dominated by the wire.

We measure the noise signal using same setup before. Because of the smaller resistance for the new nanowire device, we increase the maximum current from 113 μA to 200 μA. This will increase the maximum voltage noise intensity and eV/k_BT ratio, to reach the region that noise intensity is proportional to the bias. the measured noise intensity dependence on current bias from T=3 K to 10 K is shown in Figure 6-17 below. Measured noise intensities are shown as orange color error bar, and theoretical shot noise with different Fano factors are plotted as dashed for comparison. The measured noise remains much smaller than Fermi liquid nanowire's 1/3 Fano factor shot noise for whole temperature range.

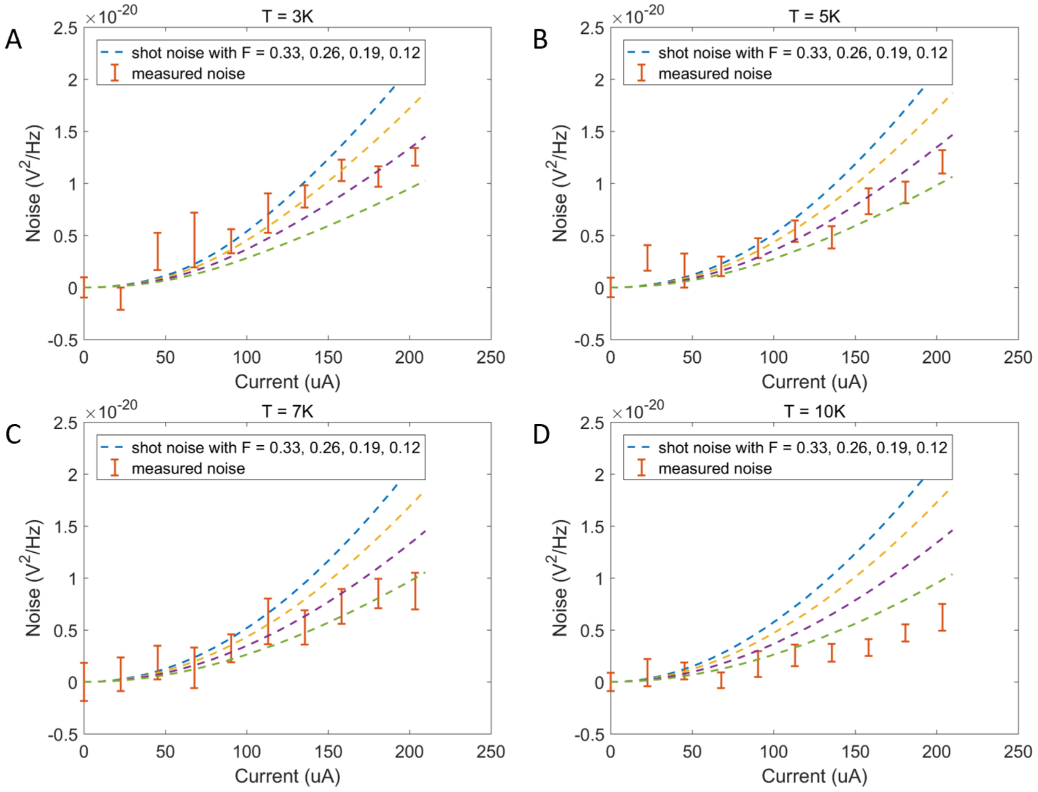

Figure 6-17. (A)-(D) Noise vs. bias current at various temperatures (3 K, 5 K, 7 K, 10 K), with comparison dashed lines showing expectations for particular Fano factors. The orange color error bars are from 15 repeated measurements data and connected through straight guide lines. The measured noise remains far below theoretical expectations for a diffusive nanowire of a conventional Fermi liquid at all temperature.

To evaluate the phonon contribution as we did before, we also fabricated a 50 μm long $YbRh_2Si_2$ wire using same process. Figure 6-18 below shows the SEM image and differential resistance data on this long nanowire.

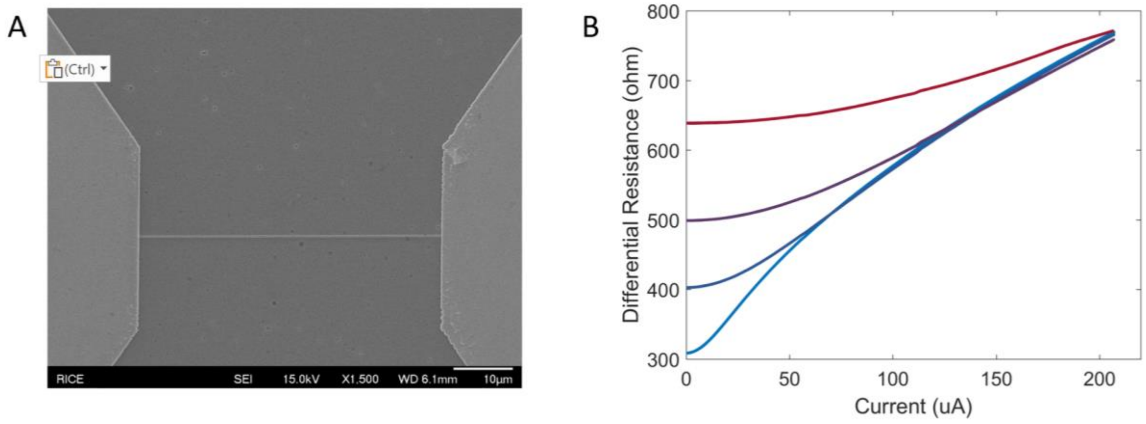

Figure 6-18. $YbRh_2Si_2$ 50 μm long nanowire device patterened on another film. (A). SEM image of nanowire divice connecting two large gold pads. (B). Differential resistance dV/dI as a function of bias current at 10 K, 7 K, 5 K, and 3 K (top to bottom).

The normalized resistance dependence on temperature on this long nanowire looks a little different with what we expect as shown in Figure 6-19. But it still remains linear in temperature dependence of resistance at low temperature range, and the normalized magnetoresistance at four different temperatures look quite similar. So we think we can still use this device to estimate the electron-phonon coupling strength parameters as we did before.

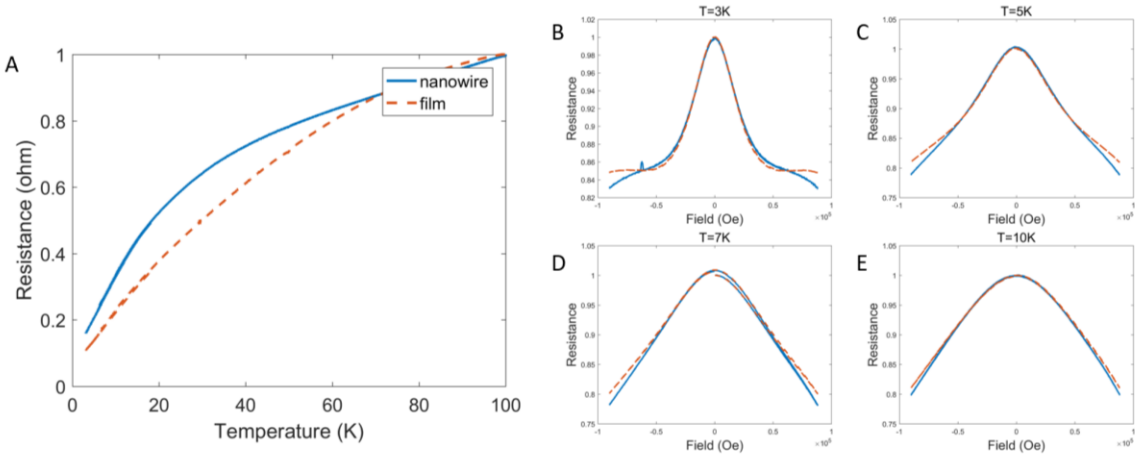

Figure 6-19. (A)Normalized resistance as a function of temperature for both the unpatterned film and the etched 50 μm long nanowire, showing linear-in-T resistivity in the low temperature limit. (B-E) Normalized resistance as a function of in-plane magnetic field for both the unpatterned MBE film and the etched nanowire (B oriented transverse to the nanowire) from T = 3 K to 10 K. The nearly identical magnetic field response between long nanowire and unpatterned film suggests that patterning did not substantially alter the electronic properties of the epitaxial $YbRh_2Si_2$ material, and that resistance is dominated by the wire.

Figure 6-20(A) shows the measured voltage noise vs. bias current data at 3 K, 5 K, and 7 K for this 50 μm long YbRh2Si2 wire, fabricated through the same process. For a long nanowire with a length much longer than the electron-phonon scattering length, thermal transport is dominated by electron-phonon coupling. Following the method in section 6.6, At each temperature the data can be fit well with a single Γ except for 7 K because of $1/f$ noise at the highest bias, the values of which are 7.5×10^9 $K^{-3}m^{-2}$, 7.5 ×

10^9 K^{-3}m^{-2}, and 7 × 10^9 K^{-3}m^{-2}, for temperatures 3 K, 5 K, and 7 K respectively. These values are close to the reported coupling for gold, 5 × 10^9 K^{-3}m^{-2}.

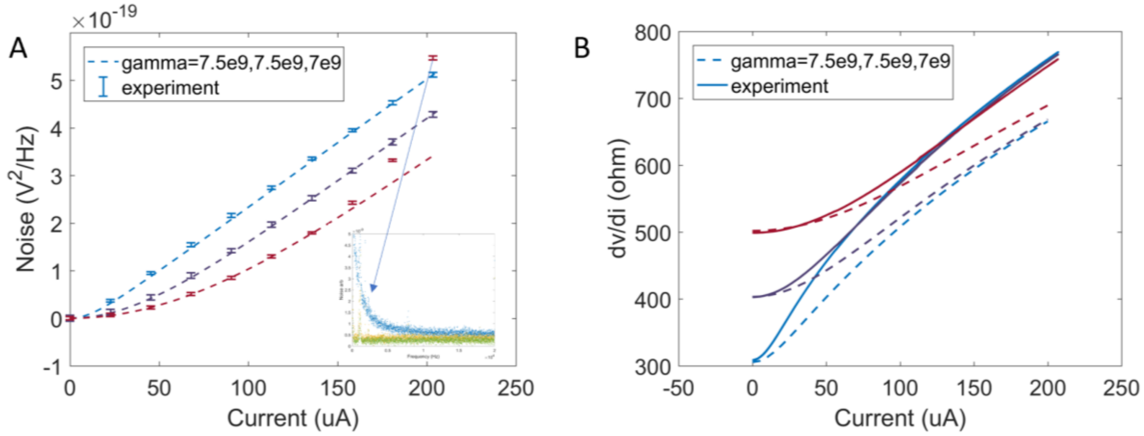

Figure 6-20. Inferring the electron-phonon coupling on new film. (A) Voltage noise as a function of bias current in a 50 μm long $YbRh_2Si_2$ wire, of roughly double width to the nanowires used in the main experiment. The dashed curves are fits to the model in secton 6.6, where the fitted electron-phonon coupling parameters are Γ = 7.5 × 10^9 K^{-3}m^{-2}, 7.5 × 10^9 K^{-3}m^{-2}, and 7 × 10^9 K^{-3}m^{-2} at T=3 K, 5 K, and 7 K, respectively. Inset shows the spectrum at I = 0 μA, 100 μA, and 200 μA. The deviation of fitting at high bias for T = 7K is caused by this $1/f$ noise. (B) Using the temperature profiles computed from the model with those values of Γ, we compare the computed $\frac{dV}{dI}$ as a function of bias (dashed lines) with the measured data (solid lines), showing good qualitative agreement while implying some intrinsic non-Ohmic response in the material. The inferred Γ values are close to gold, thus demonstrating that there is no greatly enhanced electron-phonon coupling in $YbRh_2Si_2$.

Similar with what we did in section 6.6, we used estimated electron-phonon coupling strength parameter $\Gamma = 7.5 \times 10^9$ K^{-3}m^{-2} to simulate the noise intensity in short nanowire case, as shown in Figure 6-21. We found same result as previous device that the real noise intensity is much smaller than simulation, and this means phonon is not the main reason to suppress shot noise in $YbRh_2Si_2$ nanowire. This results support our original conclusion that the suppressed shot noise in $YbRh_2Si_2$ indicates the lack of well-defined quasiparticles.

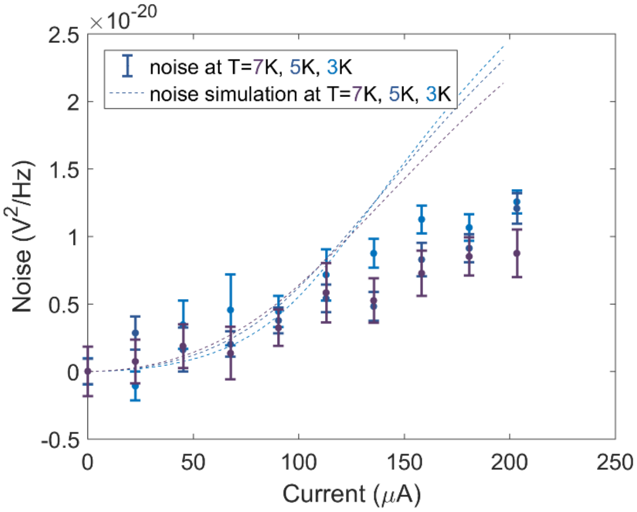

Figure 6-21. Simulations showing that the measured electron-phonon coupling cannot be the source of noise suppression. The calculated noise expected from the model (dashed lines), which disagree greatly with the measured values (solid points). This shows that with the measured electron-phonon coupling Figure 6-20, in the usual quasiparticle/Fermi Liquid treatment, there should be much greater noise than what is seen in the experiment.

References

[1] H. Nyquist, *Thermal Agitation of Electric Charge in Conductors*, Phys. Rev. **32**, 110 (1928).

[2] J. B. Johnson, *Thermal Agitation of Electricity in Conductors*, Phys. Rev. **32**, 97 (1928).

[3] A. Einstein, *Investigations on the Theory of Brownian Movement*, Ann. Physik, 1906, 19, 371-381 (n.d.).

[4] M. S. Ab-Rahman, M. F. Ibrahim, and A. A. A. Rahni, *Thermal Noise Effect in FTTH Communication Systems*, in *2008 Fourth Advanced International Conference on Telecommunications* (2008), pp. 364–370.

[5] R. Schreier, J. Silva, J. Steensgaard, and G. C. Temes, *Design-Oriented Estimation of Thermal Noise in Switched-Capacitor Circuits*, IEEE Transactions on Circuits and Systems I: Regular Papers **52**, 2358 (2005).

[6] R. Sarpeshkar, T. Delbruck, and C. A. Mead, *White Noise in MOS Transistors and Resistors*, IEEE Circuits and Devices Magazine **9**, 23 (1993).

[7] H. A. Johnson and M. Pavelec, *Thermal Noise in Cells*, Am J Pathol. 1972 Oct; 69(1): 119–130. (n.d.).

[8] H. A. Johnson, *Thermal Noise and Biological Information*, The Quarterly Review of Biology **62**, 141 (1987).

[9] D R White et al., *The Status of Johnson Noise Thermometry*, Metrologia **33**, 325 (1996).

[10] Robert Kamper, *Survey of Noise Thermometry*, in (Proc., 5th Symp. Temperature, Its Measurement and Control in Science and Industry, Washington, DC, USA, 1971).

[11] T. V. Blalock and R. L. Shepard, *Decade of Progress in High-Temperature Johnson Noise Thermometry*, New York, American Institute of Physics, 1982, 1219-1223 (n.d.).

[12] h Brixy, *Noise Thermometers*, in *Sensors*, Vol. Vol. 4 (Edited by J. Scholz and T. Ricolfi), Weinheim, VCH, 1990. (n.d.).

[13] A. Fleischmann, A. Reiser, and C. Enss, *Noise Thermometry for Ultralow Temperatures*, Journal of Low Temperature Physics **201**, 803 (2020).

[14] E. T. Patronis, H. Marshak, C. A. Reynolds, V. L. Sailor, and F. J. Shore, *Low-Temperature Thermal Noise Thermometer*, Review of Scientific Instruments **30**, 578 (1959).

[15] D. Rothfuß, A. Reiser, A. Fleischmann, and C. Enss, *Noise Thermometry at Ultra Low Temperatures*, Appl. Phys. Lett. **103**, 052605 (2013).

[16] F. N. Hooge, T. G. M. Kleinpenning, and L. K. J. Vandamme, *Experimental Studies on 1/f Noise*, Reports on Progress in Physics **44**, 479 (1981).

[17] M. B. Weissman, *1/f Noise and Other Slow, Nonexponential Kinetics in Condensed Matter*, Rev. Mod. Phys. **60**, 537 (1988).

[18] S. Kogan, *Electronic Noise and Fluctuations in Solids* (2008).

[19] P. Dutta and P. M. Horn, *Low-Frequency Fluctuations in Solids: $\frac{1}{f}$ Noise*, Rev. Mod. Phys. **53**, 497 (1981).

[20] F. N. Hooge, *1/f Noise Is No Surface Effect*, Physics Letters A **29**, 139 (1969).

[21] A. L. McWhorter, *1/f Noise and Germanium Surface Properties*, Semiconductor Surface Physics 207 (1957).

[22] F. N. Hooge, *Discussion of Recent Experiments on 1/f Noise*, Physica **60**, 130 (1976).

[23] E. Paladino, Y. M. Galperin, G. Falci, and B. L. Altshuler, *1/f Noise: Implications for Solid-State Quantum Information*, Rev. Mod. Phys. **86**, 361 (2014).

[24] T. D. Ladd, F. Jelezko, R. Laflamme, Y. Nakamura, C. Monroe, and J. L. O'Brien, *Quantum Computers*, Nature **464**, 45 (2010).

[25] J. Clarke and F. K. Wilhelm, *Superconducting Quantum Bits*, Nature **453**, 1031 (2008).

[26] A. A. Balandin, *Noise and Fluctuations Control in Electronic Devices*, American Scientific Publishers, Los Angeles, 2002 (n.d.).

[27] A. A. Balandin, *Low Flicker-Noise GaN/AlGaN Heterostructure Field-Effect Transistors for Microwave Communications.*, IEEE Trans. Microwave Theory Tech 47, 1413 – 1417 (1999) (n.d.).

[28] M. Jin, S.-J. Tang, J.-H. Chen, X.-C. Yu, H. Shu, Y. Tao, A. K. Chen, Q. Gong, X. Wang, and Y.-F. Xiao, *1/f-Noise-Free Optical Sensing with an Integrated Heterodyne Interferometer*, Nature Communications **12**, 1973 (2021).

[29] I. Bloom and Y. Nemirovsky, *1/ f Noise Reduction of Metal-oxide-semiconductor Transistors by Cycling from Inversion to Accumulation*, Appl. Phys. Lett. **58**, 1664 (1991).

[30] E. A. M. Klumperink, S. L. J. Gierkink, A. P. van der Wel, and B. Nauta, *Reducing MOSFET 1/f Noise and Power Consumption by Switched Biasing*, IEEE Journal of Solid-State Circuits **35**, 994 (2000).

[31] G. Ouyang, A. Hildebrandt, F. Schmitz, and C. S. Herrmann, *Decomposing Alpha and 1/f Brain Activities Reveals Their Differential Associations with Cognitive Processing Speed*, NeuroImage **205**, 116304 (2020).

[32] S. Dave, T. A. Brothers, and T. Y. Swaab, *1/f Neural Noise and Electrophysiological Indices of Contextual Prediction in Aging*, Brain Res. 2018 Jul 15; 1691: 34–43. (n.d.).

[33] B. Voytek, M. Kramer, and J. Case, *Age-Related Changes in 1/f Neural Electrophysiological Noise. J Neurosci.*, J Neurosci. 2015 Sep 23; 35(38): 13257–13265. (n.d.).

[34] R. Jayaraman and C. G. Sodini, *A 1/f Noise Technique to Extract the Oxide Trap Density near the Conduction Band Edge of Silicon*, IEEE Transactions on Electron Devices **36**, 1773 (1989).

[35] A. Rehman, J. A. Delgado Notario, J. Salvador Sanchez, Y. M. Meziani, G. Cywiński, W. Knap, A. A. Balandin, M. Levinshtein, and S. Rumyantsev, *Nature of the 1/f Noise in Graphene—Direct Evidence for the Mobility Fluctuation Mechanism*, Nanoscale **14**, 7242 (2022).

[36] G. Liu, S. Rumyantsev, M. A. Bloodgood, T. T. Salguero, and A. A. Balandin, *Low-Frequency Current Fluctuations and Sliding of the Charge Density Waves in Two-Dimensional Materials*, Nano Lett. **18**, 3630 (2018).

[37] Ya. M. Blanter and M. Büttiker, *Shot Noise in Mesoscopic Conductors*, Physics Reports **336**, 1 (2000).

[38] L. Sohn, L. Kouwenhoven, and G. Schon, *Mesoscopic Electron Transport* (Springer Dordrecht, 1997).

[39] G. D.C, S. M., and T. T. V. J., *Coulomb and Interference Effects in Small Electronic Structures* (Editions Frontieres, Gif-sur-Yvette, 1994, p. 405., n.d.).

[40] I. Y, *Introduction to Mesoscopic Physics* (Oxford University Press, Oxford, 1997, n.d.).

[41] W. Schottky, *Über Spontane Stromschwankungen in Verschiedenen Elektrizitätsleitern*, Annalen Der Physik **362**, 541 (1918).

[42] K. Kobayashi and M. Hashisaka, *Shot Noise in Mesoscopic Systems: From Single Particles to Quantum Liquids*, J. Phys. Soc. Jpn. **90**, 102001 (2021).

[43] S. C, O. S, S. E.V, and G. H, *Shot Noise in Schottky's Vacuum Tube*, ArXiv:Cond-Mat/0112504 (n.d.).

[44] L. Spietz, K. W. Lehnert, I. Siddiqi, and R. J. Schoelkopf, *Primary Electronic Thermometry Using the Shot Noise of a Tunnel Junction*, Science **300**, 1929 (2003).

[45] P. Zhou, L. Chen, Y. Liu, I. Sochnikov, A. T. Bollinger, M.-G. Han, Y. Zhu, X. He, I. Božović, and D. Natelson, *Electron Pairing in the Pseudogap State Revealed by Shot Noise in Copper Oxide Junctions*, Nature **572**, 493 (2019).

[46] C. L. Kane and M. P. A. Fisher, *Nonequilibrium Noise and Fractional Charge in the Quantum Hall Effect*, Phys. Rev. Lett. **72**, 724 (1994).

[47] A. Crépieux, P. Devillard, and T. Martin, *Photoassisted Current and Shot Noise in the Fractional Quantum Hall Effect*, Phys. Rev. B **69**, 205302 (2004).

[48] P. Glidic, O. Maillet, C. Piquard, A. Aassime, A. Cavanna, Y. Jin, U. Gennser, A. Anthore, and F. Pierre, *Quasiparticle Andreev Scattering in the* $\nu = 1/3$ *Fractional Quantum Hall Regime*, Nature Communications **14**, 514 (2023).

[49] M. Heiblum, *Quantum Shot Noise in Edge Channels*, Physica Status Solidi (b) **243**, 3604 (2006).

[50] Y. Ronen, Y. Cohen, J.-H. Kang, A. Haim, M.-T. Rieder, M. Heiblum, D. Mahalu, and H. Shtrikman, *Charge of a Quasiparticle in a Superconductor*, Proceedings of the National Academy of Sciences **113**, 1743 (2016).

[51] X. Jehl, M. Sanquer, R. Calemczuk, and D. Mailly, *Detection of Doubled Shot Noise in Short Normal-Metal/ Superconductor Junctions*, Nature **405**, 50 (2000).

[52] K. M. Bastiaans et al., *Direct Evidence for Cooper Pairing without a Spectral Gap in a Disordered Superconductor above Tc*, Science **374**, 608 (2021).

[53] R. de-Picciotto, M. Reznikov, M. Heiblum, V. Umansky, G. Bunin, and D. Mahalu, *Direct Observation of a Fractional Charge*, Nature **389**, 162 (1997).

[54] L. Saminadayar, D. C. Glattli, Y. Jin, and B. Etienne, *Observation of the 1/3 Fractionally Charged Laughlin Quasiparticle*, Phys. Rev. Lett. **79**, 2526 (1997).

[55] M. Reznikov, R. de Picciotto, T. G. Griffiths, M. Heiblum, and V. Umansky, *Observation of Quasiparticles with One-Fifth of an Electron's Charge*, Nature **399**, 238 (1999).

[56] M. Dolev, M. Heiblum, V. Umansky, A. Stern, and D. Mahalu, *Observation of a Quarter of an Electron Charge at the ν = 5/2 Quantum Hall State*, Nature **452**, 829 (2008).

[57] S. Tewari and J. van Ruitenbeek, *Anomalous Nonlinear Shot Noise at High Voltage Bias*, Nano Lett. **18**, 5217 (2018).

[58] R. B. Laughlin, *Anomalous Quantum Hall Effect: An Incompressible Quantum Fluid with Fractionally Charged Excitations*, Phys. Rev. Lett. **50**, 1395 (1983).

[59] R. B. Laughlin, *Current Status of Semionic Pairing Theory of High−Tc Superconductors*, Int. J. Mod. Phys. B **05**, 1507 (1991).

[60] D. C. Tsui, H. L. Stormer, and A. C. Gossard, *Two-Dimensional Magnetotransport in the Extreme Quantum Limit*, Phys. Rev. Lett. **48**, 1559 (1982).

[61] P. Fendley, A. W. W. Ludwig, and H. Saleur, *Exact Nonequilibrium Dc Shot Noise in Luttinger Liquids and Fractional Quantum Hall Devices*, Phys. Rev. Lett. **75**, 2196 (1995).

[62] A. H. Steinbach, J. M. Martinis, and M. H. Devoret, *Observation of Hot-Electron Shot Noise in a Metallic Resistor*, Phys. Rev. Lett. **76**, 3806 (1996).

[63] K. E. Nagaev, *On the Shot Noise in Dirty Metal Contacts*, Physics Letters A **169**, 103 (1992).

[64] C. W. J. Beenakker and M. Büttiker, *Suppression of Shot Noise in Metallic Diffusive Conductors*, Phys. Rev. B **46**, 1889 (1992).

[65] V. I. Kozub and A. M. Rudin, *Shot Noise in Mesoscopic Diffusive Conductors in the Limit of Strong Electron-Electron Scattering*, Phys. Rev. B **52**, 7853 (1995).

[66] K. E. Nagaev, *Influence of Electron-Electron Scattering on Shot Noise in Diffusive Contacts*, Phys. Rev. B **52**, 4740 (1995).

[67] H. P and H. W, *The Art of Electronics* ((Cambridge University Press, Cambridge, 1989), p. 432., n.d.).

[68] M. Henny, H. Birk, R. Huber, C. Strunk, A. Bachtold, M. Krüger, and C. Schönenberger, *Electron Heating Effects in Diffusive Metal Wires*, Appl. Phys. Lett. **71**, 773 (1997).

[69] M. Büttiker, *Scattering Theory of Thermal and Excess Noise in Open Conductors*, Phys. Rev. Lett. **65**, 2901 (1990).

[70] F. Liefrink, J. I. Dijkhuis, M. J. M. de Jong, L. W. Molenkamp, and H. van Houten, *Experimental Study of Reduced Shot Noise in a Diffusive Mesoscopic Conductor*, Phys. Rev. B **49**, 14066 (1994).

[71] R. J. Schoelkopf, P. J. Burke, A. A. Kozhevnikov, D. E. Prober, and M. J. Rooks, *Frequency Dependence of Shot Noise in a Diffusive Mesoscopic Conductor*, Phys. Rev. Lett. **78**, 3370 (1997).

[72] M. Henny, S. Oberholzer, C. Strunk, and C. Schönenberger, *1/3-Shot-Noise Suppression in Diffusive Nanowires*, Phys. Rev. B **59**, 2871 (1999).

[73] M. Mihaila, D. Ursutiu, and I. Sandu, *Electron-Phonon Coupling as the Source of 1/f Noise in Carbon Soot*, Scientific Reports **9**, 947 (2019).

[74] D. B. Gutman and Y. Gefen, *Shot Noise in Disordered Junctions: Interaction Corrections*, Phys. Rev. B **64**, 205317 (2001).

[75] Y. Wang, C. Setty, S. Sur, L. Chen, S. Paschen, D. Natelson, and Q. Si, *Shot Noise as a Characterization of Strongly Correlated Metals*, (2022).

[76] J. H. de Boer and E. J. W. Verwey, *Semi-Conductors with Partially and with Completely Filled3d-Lattice Bands*, Proceedings of the Physical Society **49**, 59 (1937).

[77] N. F. Mott and R. Peierls, *Discussion of the Paper by de Boer and Verwey*, Proceedings of the Physical Society **49**, 72 (1937).

[78] J. Hubbard and B. H. Flowers, *Electron Correlations in Narrow Energy Bands*, Proceedings of the Royal Society of London. Series A. Mathematical and Physical Sciences **276**, 238 (1963).

[79] M. Imada, A. Fujimori, and Y. Tokura, *Metal-Insulator Transitions*, Rev. Mod. Phys. **70**, 1039 (1998).

[80] S. Tsui, A. Baikalov, J. Cmaidalka, Y. Y. Sun, Y. Q. Wang, Y. Y. Xue, C. W. Chu, L. Chen, and A. J. Jacobson, *Field-Induced Resistive Switching in Metal-Oxide Interfaces*, Appl. Phys. Lett. **85**, 317 (2004).

[81] R. Waser and M. Aono, *Nanoionics-Based Resistive Switching Memories*, Nature Materials **6**, 833 (2007).

[82] D. B. Strukov, G. S. Snider, D. R. Stewart, and R. S. Williams, *The Missing Memristor Found*, Nature **453**, 80 (2008).

[83] J. J. Yang, M. D. Pickett, X. Li, D. A. A. Ohlberg, D. R. Stewart, and R. S. Williams, *Memristive Switching Mechanism for Metal/Oxide/Metal Nanodevices*, Nature Nanotechnology **3**, 429 (2008).

[84] D.-H. Kwon et al., *Atomic Structure of Conducting Nanofilaments in TiO2 Resistive Switching Memory*, Nature Nanotechnology **5**, 148 (2010).

[85] J. del Valle, J. G. Ramírez, M. J. Rozenberg, and I. K. Schuller, *Challenges in Materials and Devices for Resistive-Switching-Based Neuromorphic Computing*, Journal of Applied Physics **124**, 211101 (2018).

[86] P. D. Dernier and M. Marezio, *Crystal Structure of the Low-Temperature Antiferromagnetic Phase of ${\mathrm{V}}_{2}${\mathrm{O}}_{3}$*, Phys. Rev. B **2**, 3771 (1970).

[87] A. S. McLeod et al., *Nanotextured Phase Coexistence in the Correlated Insulator V2O3*, Nature Physics **13**, 80 (2016).

[88] D. B. McWhan and J. P. Remeika, *Metal-Insulator Transition in* $(V_{1-x}Cr_x)_2O_3$, Phys. Rev. B **2**, 3734 (1970).

[89] E. Abreu, S. Wang, J. G. Ramírez, M. Liu, J. Zhang, K. Geng, I. K. Schuller, and R. D. Averitt, *Dynamic Conductivity Scaling in Photoexcited* V_2O_3 *Thin Films*, Phys. Rev. B **92**, 085130 (2015).

[90] G. Lantz et al., *Ultrafast Evolution and Transient Phases of a Prototype Out-of-Equilibrium Mott–Hubbard Material*, Nature Communications **8**, 13917 (2017).

[91] N. Alyabyeva, J. Sakai, M. Bavencoffe, J. Wolfman, P. Limelette, H. Funakubo, and A. Ruyter, *Metal-Insulator Transition in V2O3 Thin Film Caused by Tip-Induced Strain*, Appl. Phys. Lett. **113**, 241603 (2018).

[92] J. del Valle et al., *Subthreshold Firing in Mott Nanodevices*, Nature **569**, 388 (2019).
[93] A. Singer et al., *Nonequilibrium Phase Precursors during a Photoexcited Insulator-to-Metal Transition in V_2O_3*, Phys. Rev. Lett. **120**, 207601 (2018).
[94] S. R. Broadbent and J. M. Hammersley, *Percolation Processes: I. Crystals and Mazes*, Mathematical Proceedings of the Cambridge Philosophical Society **53**, 629 (1957).
[95] Z. Topalian, S.-Y. Li, G. A. Niklasson, C. G. Granqvist, and L. B. Kish, *Resistance Noise at the Metal–Insulator Transition in Thermochromic VO2 Films*, Journal of Applied Physics **117**, 025303 (2015).
[96] G. A. Garfunkel and M. B. Weissman, *Noise Scaling in Continuum Percolating Films*, Phys. Rev. Lett. **55**, 296 (1985).
[97] R. Rammal, C. Tannous, P. Breton, and A.-M. S. Tremblay, *Flicker (1/f) Noise in Percolation Networks: A New Hierarchy of Exponents*, Phys. Rev. Lett. **54**, 1718 (1985).
[98] B. I. Halperin, S. Feng, and P. N. Sen, *Differences between Lattice and Continuum Percolation Transport Exponents*, Phys. Rev. Lett. **54**, 2391 (1985).
[99] C. Pennetta, G. Trefán, and L. Reggiani, *Scaling Law of Resistance Fluctuations in Stationary Random Resistor Networks*, Phys. Rev. Lett. **85**, 5238 (2000).
[100] L. B. Kiss and P. Svedlindh, *New Noise Exponents in Random Conductor-Superconductor and Conductor-Insulator Mixtures*, Phys. Rev. Lett. **71**, 2817 (1993).
[101] L. Landau, *On the Theory of the Fermi Liquid*, Sov. Phys. JETP 8.1 (1959), p. 70 (n.d.).
[102] J. Lindhard, *ON THE PROPERTIES OF A GAS OF CHARGED PARTICLES*, Kgl. Danske Videnskab. Selskab Mat.-Fys. Medd. **Vol:**, (1954).
[103] A. J. Schofield, *Non-Fermi Liquids*, Contemporary Physics **40**, 95 (1999).
[104] L. Landau and I. Pomerantschuk, *Über Eigneschaften Der Metalle Bei Sehr Niedrigen Temperaturen*, Phys. Z. Sowjet **10**, 649 (1936).
[105] W. Baber, *The Contribution to the Electrical Resistance of Metals from Collisions between Electrons*, Proceedings of the Royal Society of London. Series A-Mathematical and Physical Sciences **158**, 383 (1937).
[106] X. Lin, B. Fauqué, and K. Behnia, *Scalable T2 Resistivity in a Small Single-Component Fermi Surface*, Science **349**, 945 (2015).
[107] J. Wang, J. Wu, T. Wang, Z. Xu, J. Wu, W. Hu, Z. Ren, S. Liu, K. Behnia, and X. Lin, *T-Square Resistivity without Umklapp Scattering in Dilute Metallic Bi2O2Se*, Nature Communications **11**, 3846 (2020).
[108] *Chapter 5 Landau Theory of the Fermi Liquid*, in (n.d.).
[109] D. Neilson, *Landau Fermi Liquid Theory*, Aust. J. Phys. **49**, 79 (1996).
[110] A. J. Leggett, *A Theoretical Description of the New Phases of Liquid $^{3}\mathrm{He}$*, Rev. Mod. Phys. **47**, 331 (1975).
[111] D. Pines, *Theory Of Quantum Liquids* (CRC Press, (1966), 1966).
[112] P. Fournier, P. Mohanty, E. Maiser, S. Darzens, T. Venkatesan, C. J. Lobb, G. Czjzek, R. A. Webb, and R. L. Greene, *Insulator-Metal Crossover near Optimal*

Doping in ${\mathrm{Pr}}_{2\ensuremath{-}\mathit{x}}{\mathrm{Ce}}_{\mathit{x}}{\mathrm{CuO}}_{4}$: Anomalous Normal-State Low Temperature Resistivity, Phys. Rev. Lett. **81**, 4720 (1998).

[113] A. P. Mackenzie, S. R. Julian, D. C. Sinclair, and C. T. Lin, *Normal-State Magnetotransport in Superconducting ${\mathrm{Tl}}_{2}${\mathrm{Ba}}_{2}${\mathrm{CuO}}_{6+\mathrm{\ensuremath{\delta}}}$ to Millikelvin Temperatures*, Phys. Rev. B **53**, 5848 (1996).

[114] M. Gurvitch and A. T. Fiory, *Resistivity of ${\mathrm{La}}_{1.825}${\mathrm{Sr}}_{0.175}${\mathrm{CuO}}_{4}$ and ${\mathrm{YBa}}_{2}${\mathrm{Cu}}_{3}${\mathrm{O}}_{7}$ to 1100 K: Absence of Saturation and Its Implications*, Phys. Rev. Lett. **59**, 1337 (1987).

[115] H. Takagi, B. Batlogg, H. L. Kao, J. Kwo, R. J. Cava, J. J. Krajewski, and W. F. Peck, *Systematic Evolution of Temperature-Dependent Resistivity in ${\mathrm{La}}_{2\mathrm{\ensuremath{-}}\mathit{x}}${\mathrm{Sr}}_{\mathit{x}}${\mathrm{CuO}}_{4}$*, Phys. Rev. Lett. **69**, 2975 (1992).

[116] P. B. Allen, H. Berger, O. Chauvet, L. Forro, T. Jarlborg, A. Junod, B. Revaz, and G. Santi, *Transport Properties, Thermodynamic Properties, and Electronic Structure of ${\mathrm{SrRuO}}_{3}$*, Phys. Rev. B **53**, 4393 (1996).

[117] A. W. Tyler, A. P. Mackenzie, S. NishiZaki, and Y. Maeno, *High-Temperature Resistivity of ${\mathrm{Sr}}_{2}{\mathrm{RuO}}_{4}:$ Bad Metallic Transport in a Good Metal*, Phys. Rev. B **58**, R10107 (1998).

[118] J. Custers, P. Gegenwart, H. Wilhelm, K. Neumaier, Y. Tokiwa, O. Trovarelli, C. Geibel, F. Steglich, C. Pépin, and P. Coleman, *The Break-up of Heavy Electrons at a Quantum Critical Point*, Nature **424**, 524 (2003).

[119] J. Custers, P. Gegenwart, C. Geibel, F. Steglich, P. Coleman, and S. Paschen, *Evidence for a Non-Fermi-Liquid Phase in Ge-Substituted ${\mathrm{YbRh}}_{2}{\mathrm{Si}}_{2}$*, Phys. Rev. Lett. **104**, 186402 (2010).

[120] T. Tomita, K. Kuga, Y. Uwatoko, P. Coleman, and S. Nakatsuji, *Strange Metal without Magnetic Criticality*, Science **349**, 506 (2015).

[121] P. W. Phillips, N. E. Hussey, and P. Abbamonte, *Stranger than Metals*, Science **377**, eabh4273 (n.d.).

[122] C. Yang et al., *Signatures of a Strange Metal in a Bosonic System*, Nature **601**, 205 (2022).

[123] C. M. Varma, P. B. Littlewood, S. Schmitt-Rink, E. Abrahams, and A. E. Ruckenstein, *Phenomenology of the Normal State of Cu-O High-Temperature Superconductors*, Phys. Rev. Lett. **63**, 1996 (1989).

[124] E. W. Huang, R. Sheppard, B. Moritz, and T. P. Devereaux, *Strange Metallicity in the Doped Hubbard Model*, Science **366**, 987 (2019).

[125] S. A. Hartnoll and A. Karch, *Scaling Theory of the Cuprate Strange Metals*, Phys. Rev. B **91**, 155126 (2015).

[126] H. v. Löhneysen, T. Pietrus, G. Portisch, H. G. Schlager, A. Schröder, M. Sieck, and T. Trappmann, *Non-Fermi-Liquid Behavior in a Heavy-Fermion Alloy at a Magnetic Instability*, Phys. Rev. Lett. **72**, 3262 (1994).

[127] K. Heuser, E.-W. Scheidt, T. Schreiner, and G. R. Stewart, *Inducement of Non-Fermi-Liquid Behavior with a Magnetic Field*, Phys. Rev. B **57**, R4198 (1998).

[128] O. Trovarelli, C. Geibel, S. Mederle, C. Langhammer, F. M. Grosche, P. Gegenwart, M. Lang, G. Sparn, and F. Steglich, *${\mathrm{YbRh}}_{2}{\mathrm{Si}}_{2}$: Pronounced Non-Fermi-Liquid Effects above a Low-Lying Magnetic Phase Transition*, Phys. Rev. Lett. **85**, 626 (2000).

[129] P. Gegenwart, J. Custers, C. Geibel, K. Neumaier, T. Tayama, K. Tenya, O. Trovarelli, and F. Steglich, *Magnetic-Field Induced Quantum Critical Point in $\mathrm{Y}\mathrm{b}\mathrm{R}{\mathrm{h}}_{\mathrm{2}}\mathrm{S}{\mathrm{i}}_{\mathrm{2}}$*, Phys. Rev. Lett. **89**, 056402 (2002).

[130] P. Gegenwart, T. Westerkamp, C. Krellner, Y. Tokiwa, S. Paschen, C. Geibel, F. Steglich, E. Abrahams, and Q. Si, *Multiple Energy Scales at a Quantum Critical Point*, Science **315**, 969 (2007).

[131] S. Friedemann, T. Westerkamp, M. Brando, N. Oeschler, S. Wirth, P. Gegenwart, C. Krellner, C. Geibel, and F. Steglich, *Detaching the Antiferromagnetic Quantum Critical Point from the Fermi-Surface Reconstruction in YbRh2Si2*, Nature Physics **5**, 465 (2009).

[132] E. Schuberth et al., *Emergence of Superconductivity in the Canonical Heavy-Electron Metal YbRh2Si2*, Science **351**, 485 (2016).

[133] L. Prochaska et al., *Singular Charge Fluctuations at a Magnetic Quantum Critical Point*, Science **367**, 285 (2020).

[134] A. Kumar, L. Saminadayar, D. C. Glattli, Y. Jin, and B. Etienne, *Experimental Test of the Quantum Shot Noise Reduction Theory*, Phys. Rev. Lett. **76**, 2778 (1996).

[135] B. G. M. Vandeginste, *Robust Regression and Outlier Detection. P. J. Rousseeuw and A. M. Leroy, John Wiley & Sons, New York, 1987. No. of Pages: 329. Price: £31.95. ISBN:0 471 85233 3*, Journal of Chemometrics **2**, 299 (1988).

[136] F. Wu, L. Roschier, T. Tsuneta, M. Paalanen, T. Wang, and P. Hakonen, *Setup for Shot Noise Measurements in Carbon Nanotubes*, AIP Conference Proceedings **850**, 1482 (2006).

[137] M. Reznikov, M. Heiblum, H. Shtrikman, and D. Mahalu, *Temporal Correlation of Electrons: Suppression of Shot Noise in a Ballistic Quantum Point Contact*, Phys. Rev. Lett. **75**, 3340 (1995).

[138] L. Chen, P. Zhou, Y. Kalcheim, I. K. Schuller, and D. Natelson, *Percolation and Nanosecond Fluctuators in V2O3 Films within the Metal–Insulator Transition*, APL Materials **8**, 101103 (2020).

[139] V. Podzorov, M. Uehara, M. E. Gershenson, T. Y. Koo, and S.-W. Cheong, *Giant 1/f Noise in Perovskite Manganites: Evidence of the Percolation Threshold*, Phys. Rev. B **61**, R3784 (2000).

[140] A.-M. S. Tremblay, S. Feng, and P. Breton, *Exponents for 1/f Noise, near a Continuum Percolation Threshold*, Phys. Rev. B **33**, 2077 (1986).

[141] J. G. Ramirez, T. Saerbeck, S. Wang, J. Trastoy, M. Malnou, J. Lesueur, J.-P. Crocombette, J. E. Villegas, and I. K. Schuller, *Effect of Disorder on the Metal-Insulator Transition of Vanadium Oxides: Local versus Global Effects*, Phys. Rev. B **91**, 205123 (2015).

[142] S. Wang, J. G. Ramírez, and I. K. Schuller, *Avalanches in Vanadium Sesquioxide Nanodevices*, Phys. Rev. B **92**, 085150 (2015).

[143] H. V. Keer, D. L. Dickerson, H. Kuwamoto, H. L. C. Barros, and J. M. Honig, *Heat Capacity of Pure and Doped V2O3 Single Crystals*, Journal of Solid State Chemistry **19**, 95 (1976).

[144] O. G. Shpyrko et al., *Direct Measurement of Antiferromagnetic Domain Fluctuations*, Nature **447**, 68 (2007).

[145] R. P. Michel, N. E. Israeloff, M. B. Weissman, J. A. Dura, and C. P. Flynn, *Electrical-Noise Measurements on Chromium Films*, Phys. Rev. B **44**, 7413 (1991).

[146] Y. Kalcheim, A. Camjayi, J. del Valle, P. Salev, M. Rozenberg, and I. K. Schuller, *Non-Thermal Resistive Switching in Mott Insulators*, ArXiv:1908.08555 [Cond-Mat] (2019).

[147] J. Przybytek, J. Fink-Finowicki, R. Puźniak, A. Shames, V. Markovich, D. Mogilyansky, and G. Jung, *Robust Random Telegraph Conductivity Noise in Single Crystals of the Ferromagnetic Insulating Manganite $La_{0.86}Ca_{0.14}MnO_3$*, Phys. Rev. B **95**, 125101 (2017).

[148] L. Chen et al., *Shot Noise Indicates the Lack of Quasiparticles in a Strange Metal*, (2022).

[149] C. M. Varma, *Colloquium: Linear in Temperature Resistivity and Associated Mysteries Including High Temperature Superconductivity*, Rev. Mod. Phys. **92**, 031001 (2020).

[150] A. Legros et al., *Universal T-Linear Resistivity and Planckian Dissipation in Overdoped Cuprates*, Nature Physics **15**, 142 (2019).

[151] J. Ayres et al., *Incoherent Transport across the Strange-Metal Regime of Overdoped Cuprates*, Nature **595**, 661 (2021).

[152] R. L. Greene, P. R. Mandal, N. R. Poniatowski, and T. Sarkar, *The Strange Metal State of the Electron-Doped Cuprates*, Annu. Rev. Condens. Matter Phys. **11**, 213 (2020).

[153] I. M. Hayes, R. D. McDonald, N. P. Breznay, T. Helm, P. J. W. Moll, M. Wartenbe, A. Shekhter, and J. G. Analytis, *Scaling between Magnetic Field and Temperature in the High-Temperature Superconductor BaFe2(As1−xPx)2*, Nature Physics **12**, 916 (2016).

[154] J. A. N. Bruin, H. Sakai, R. S. Perry, and A. P. Mackenzie, *Similarity of Scattering Rates in Metals Showing T-Linear Resistivity*, Science **339**, 804 (2013).

[155] T. Park, F. Ronning, H. Q. Yuan, M. B. Salamon, R. Movshovich, J. L. Sarrao, and J. D. Thompson, *Hidden Magnetism and Quantum Criticality in the Heavy Fermion Superconductor CeRhIn5*, Nature **440**, 65 (2006).

[156] D. H. Nguyen, A. Sidorenko, M. Taupin, G. Knebel, G. Lapertot, E. Schuberth, and S. Paschen, *Superconductivity in an Extreme Strange Metal*, Nature Communications **12**, 4341 (2021).

[157] Y. Cao, D. Chowdhury, D. Rodan-Legrain, O. Rubies-Bigorda, K. Watanabe, T. Taniguchi, T. Senthil, and P. Jarillo-Herrero, *Strange Metal in Magic-Angle Graphene with near Planckian Dissipation*, Phys. Rev. Lett. **124**, 076801 (2020).

[158] P. Coleman and A. J. Schofield, *Quantum Criticality*, Nature **433**, 226 (2005).

[159] J. A. Hertz, *Quantum Critical Phenomena*, Phys. Rev. B **14**, 1165 (1976).

[160] A. J. Millis, *Effect of a Nonzero Temperature on Quantum Critical Points in Itinerant Fermion Systems*, Phys. Rev. B **48**, 7183 (1993).

[161] Q. Si, S. Rabello, K. Ingersent, and J. L. Smith, *Locally Critical Quantum Phase Transitions in Strongly Correlated Metals*, Nature **413**, 804 (2001).

[162] P Coleman, C Pépin, Qimiao Si, and R Ramazashvili, *How Do Fermi Liquids Get Heavy and Die?*, Journal of Physics: Condensed Matter **13**, R723 (2001).

[163] T. Senthil, M. Vojta, and S. Sachdev, *Weak Magnetism and Non-Fermi Liquids near Heavy-Fermion Critical Points*, Phys. Rev. B **69**, 035111 (2004).

[164] R. A. Davison, K. Schalm, and J. Zaanen, *Holographic Duality and the Resistivity of Strange Metals*, Phys. Rev. B **89**, 245116 (2014).

[165] T. Delattre et al., *Noisy Kondo Impurities*, Nature Physics **5**, 208 (2009).

[166] O. Zarchin, M. Zaffalon, M. Heiblum, D. Mahalu, and V. Umansky, *Two-Electron Bunching in Transport through a Quantum Dot Induced by Kondo Correlations*, Phys. Rev. B **77**, 241303 (2008).

[167] A. G. Green, J. E. Moore, S. L. Sondhi, and A. Vishwanath, *Current Noise in the Vicinity of the 2D Superconductor-Insulator Quantum Critical Point*, Phys. Rev. Lett. **97**, 227003 (2006).

[168] J. Sonner and A. G. Green, *Hawking Radiation and Nonequilibrium Quantum Critical Current Noise*, Phys. Rev. Lett. **109**, 091601 (2012).

[169] S. Paschen, T. Lühmann, S. Wirth, P. Gegenwart, O. Trovarelli, C. Geibel, F. Steglich, P. Coleman, and Q. Si, *Hall-Effect Evolution across a Heavy-Fermion Quantum Critical Point*, Nature **432**, 881 (2004).

[170] E. Bakali et al., *A Knudsen Cell Approach for the Molecular Beam Epitaxy of the Heavy Fermion Compound YbRh2Si2*, Journal of Crystal Growth **595**, 126804 (2022).

[171] A. Solanki and H. Um, *Chapter Two - Top-Down Etching of Si Nanowires*, in *Semiconductors and Semimetals*, edited by S. Mokkapati and C. Jagadish, Vol. 98 (Elsevier, 2018), pp. 71–149.

[172] S Hartmann, N Oeschler, C Krellner, C Geibel, and F Steglich, *Low-Temperature Thermopower Study of YbRh2Si2*, Journal of Physics: Conference Series **150**, 042049 (2009).

[173] D. Pines and P. Nozieres, *The Theory Of Quantum Liquids Volume I: Normal Fermi Liquids* (Basic Books, 1989).

[174] M. S. Gupta, *Thermal Noise in Nonlinear Resistive Devices and Its Circuit Representation*, Proceedings of the IEEE **70**, 788 (1982).

[175] J. L. Wyatt and G. J. Coram, *Nonlinear Device Noise Models: Satisfying the Thermodynamic Requirements*, IEEE Transactions on Electron Devices **46**, 184 (1999).

[176] J. del Valle, N. Ghazikhanian, Y. Kalcheim, J. Trastoy, M.-H. Lee, M. J. Rozenberg, and I. K. Schuller, *Resistive Asymmetry Due to Spatial Confinement in First-Order Phase Transitions*, Phys. Rev. B **98**, 045123 (2018).

[177] R. Luo, X. Zhao, L. Chen, T. J. Legvold, H. Navarro, I. K. Schuller, and D. Natelson, *Spin Seebeck Effect at Low Temperatures in the Nominally Paramagnetic Insulating State of Vanadium Dioxide*, Appl. Phys. Lett. **121**, 102404 (2022).

Chapter 7

Future research

7.1. ~~f~~Follow up works

There are many possible follow up works based on my projects.

1. For the ~~m~~Mott~~-~~insulator V_2O_3, it would be interesting to investigate the noise signal in nano devices. In our previous work, we found the percolation properties and existence of very fast (ns level) fluctuators. The percolation properties comes from the coexistence of metal and insulator phases domains during the metal insulator transition [87], and the source of nanosecond fluctuators ~~are~~ is still unclear. To further understand the dynamics inside the metal insulator transition, it is better to measure the noise signal in nano devices with dimensions comparable or smaller than the single phase domain during the transition. The domains sizes can be as large as 1 μm during the metal insulator transition based on Ref [87] and some fabrication processes for nanowires are provided in Ref [176], these make the fabrication of nano devices practical. It would be possible to isolate a single fluctuator or few

fluctuators using nano devices. If it works, people can vary the size of devices and take more measurement to obtain statistic results.

2. It is probably worth trying same $1/f$ noise measurement on other ~~m~~Mott insulators such as NiO, and it would help us to find the common or different properties between different mott insulators.
3. For the shot noise measurements in $YbRh_2Si_2$ nanowires, it is worth trying The same measurements at lower temperatures. Lower temperatures measurements allow people to field tune the phase of $YbRh_2Si_2$ from strange metal to Fermi liquid, and direct comparison would be possible.
4. Shot noise in other strange metal ~~heavy fermions~~ nanowires such as $Sr_3Ru_2O_7$ would be interesting. $Sr_3Ru_2O_7$ can be tuned in and out of The strange metal phase by applying magnetic field in our PPMS setup, so we can compare the shot noise in strange metal phase and Fermi liquid phase directly. It also help us to check if the suppressed shot noise is universal in heavy fermions strange metal.
5. Noise measurements in different structures, such as STM and planar tunnel junction, made with $YbRh_2Si_2$ might be interesting, although we are still not sure whether 'quasiparticles' properties vary with devices structure.

7.2. Other research directions

In our previous work, we found the preformation of electron pairs indicated by shot noise in LSCO tunnel junction [45]. It is possible to measure shot noise in the high Tc superconductor nanowires. The noise signal across the Tc could be interesting (would be hard to measure voltage noise in superconducting state). To minimize the phonons effects, we need to use underdoped or overdoped sample that with Tc as low as possible, such as Tc = 3 K. We might see shot noise intensity higher than Fermi liquid nanowires' case if electrons form pairs.

In other work,

We saw spin seebeck effect in paramagnetic insulating state of VO_2 at low temperatures [177]. It is interesting to see whether an antiferromagnetic insulator V_2O_3 has similar properties at low temperature. This experiment is more practical than the research ideas mentioned above as we have the materials ready and fabrication processes are relatively simple.

Chapter 8

Appendix

8.1. Noise probe design

Voltage fluctuations in noise measurements are very small signal compared to th e signal in usual transport measurement. To precisely measure the noise intensity, a customized noise probe is required to pick up real signal from device and eliminate unwanted noise. The picture of our two noise probes are shown in Figure 8-1. All important parts are label by number in the picture, and I will explain some tips in following paragraphs.

The probe is inserted into the PPMS, and get good termal contact using a PPMS puck stage(13). The copper stage(13) is electrically isolated from other parts of probe by very thin tape and thermal grease, to avoid noise in the PPMS's groud going into voltage amplifiers' ground. All other part are electrically connected as the ground for amplifiers.

Probe wires(manually twisted 32 AWG copper wire with insulating coat) and samples are always shielded inside to reduce environmental background noise. Since the top part of probe is exposed to the air, there is always heat transfering from wires to sample. To reduce the direct transfering of heat from wires to athe sample and make the sample temperature closer to the big copper parts(9,11), the wires close to the samples are designed to attach tightly to the big copper parts(9,11) to let heat on the wire transfer to big copper parts(9,11) before reaching the samples. In probe 1, this is done by pressing the wire to the copper part (11) using another piece of copper plate, rubber and two screws. For probe 2, this is done by wrapping the wires and copper part(9) using aluminum foil and Kapton tape, and appling thermal grease between wire and alminum foil to increase thermal conductivity.

It is not very practical to have perfect match between probe length and PPMS chamber depth. If the probe is a little longer then PPMS chamber depth, it either cause too much strain along the rods and make it bent or even break, or it will cause small leakage on the top sealing part, or it will cause the bending of PPMS puck stage(13). If the probe is a little shorter than the PPMS chamber depth, there would be no enough pressure to make good thermal contact between PPMS puck stage(13) and bottom of PPMS chamber. Furthermore, because of thermal expansion across the broad sample temperature range, it becomes harder to find the perfect length. To solve this problem, we design a spring like structure using rubber inside customized part(2). The natural length of probe when the rubber is totally relaxed is a few millimeters longer than PPMS chamber depth, and when we load the probe into PPMS, the compressed rubber will provide pressure to guarantee good contact between PPMS puck stage(13) and bottom of PPMS chamber, and thus we don't need to worry about thermal expansion during temperature change.

One key method to reduce environmental noise is using twisted pair wires and shielding. In both probes, our twisted wires are capsulated in a conducting shield. For probe 1, we used stainless steel wire shielding mesh(5), and the shield is tightly attached to the g10 rod(4). For probe 2, the twisted pair wires are inside the hollow stainless steel rod(3). For now, there are 3 twisted pair wire, so 6 wires in total, for both probes. 6 wires are enough for most of noise measurement requirements, it is possible to add more wires in the future, but it will take effort to rewire everything.

Another thing that needs care is the vacuum sealing. We drill a hole through the vacuum tube fitting end caps(1), to fit through the 14 pin adapter(8). We add a o-ring between adapter and cap for vacuum seal. However, because our adapters are not designed for high vacuum applications, there is leakage at the pins' positions. To solve this issue, we used solder to cover all unused pins and used stycast to cover the gaps between pins and surrounding plastic part.

Our probe 1 follows similar design with our previous probe used in Ref [45], it works well with a customized sample box(12), but it can only hold sample vertically, and applied magnetic field is always in-plane. Probe 2 solves this issue using more complicated bottom part design. It is compatible with PPMS standard sample holder(10) and it can hold the sample chips both vertically and horizontally. Another advantage of our probe 2 is that the wire connection at bottom is less likely to break compared to probe

1. Every time when we load/unload sample using probe 1, we need to connect/disconnect the sample box(12) from the socket plug-in adapters, and the wires connecting to the socket plug would be bent and might be broken.

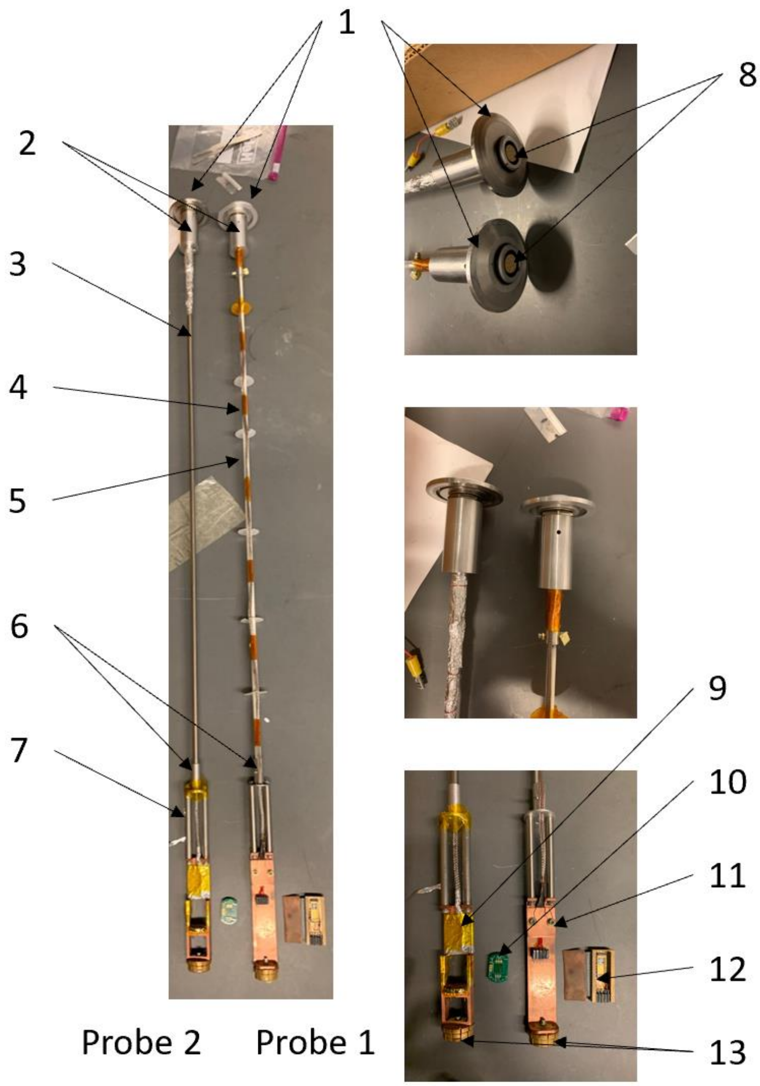

Figure 8-1. Two customized noise probes. (1) vacuum tube fitting end caps made with either stainless steel or aluminum, with hole in middle for adapters(8), (2)

customized part connecting adapters(8) and g10 rod(4) or hollow stainless steel rod(3). (3). hollow stainless steel rod with thin wall for probe 1. (4) g10 rod for probe 2. (5) stainless steel wire shielding mesh covering twisted wires. (6) customized part connecting main rod and two short stainless steel rods. (7) two short stainless steel rods connecting part(6) and big copper part(9,11). (8) 14 pins adapter for wire connections. (9) customized copper structure for sample holder of probe 2. (10) standard Quantum Design PPMS chip carrier. (11) customized copper structure for sample holder of probe 1. (12) customized sample box for probe 1. (13) PPMS puck stage for thermal contact with bottom.

Some parts of customized components are shown in the following Figures with scale in unit inch.

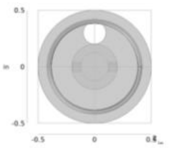

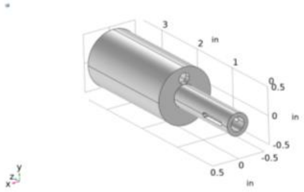

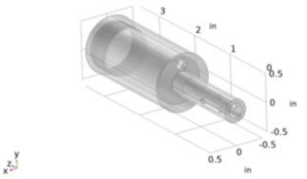

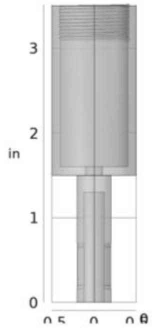

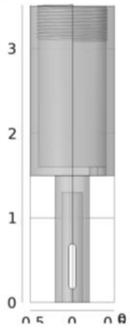

Figure 8-2. muti views of part(2): customized part connecting adapters(8) and g10 rod(4) or hollow stainless steel rod(3).

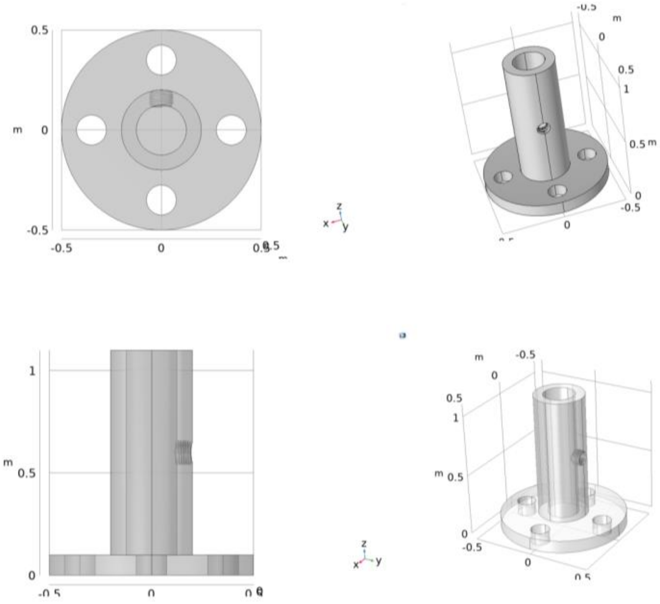

Figure 8-3. multi views of part(6): customized part connecting main rod and two short stainless steel rods.

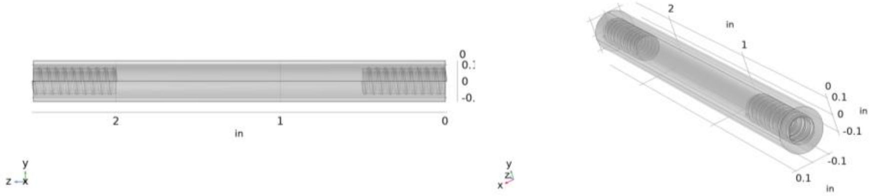

Figure 8-4. multi views of part(7): two short stainless steel rods connecting part(6) and big copper part(9,11).

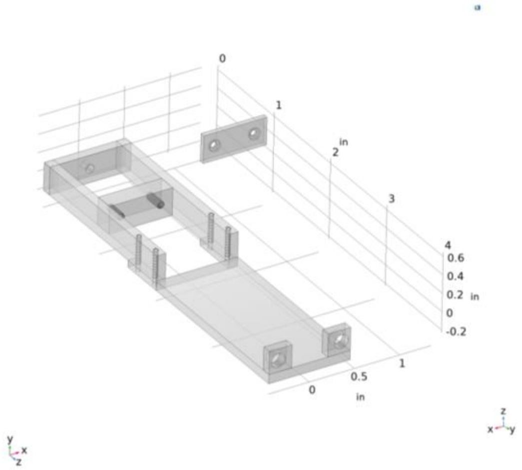
0
1
2
in
3
4
0.6
0.4
0.2
in
0
-0.2
1
0.5
0
in
y
x
z
z
x
y

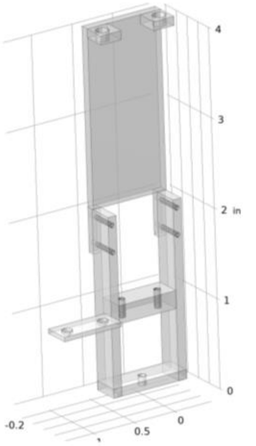
4
3
2 in
1
0
-0.2
0.5
0

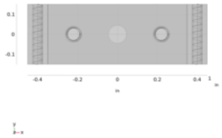
0.1
0
-0.1
-0.4
-0.2
0
0.2
0.4
in

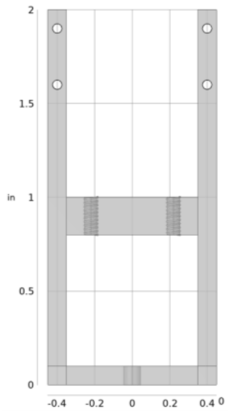
2
1.5
in 1
0.5
0
-0.4
-0.2
0
0.2
0.4
0

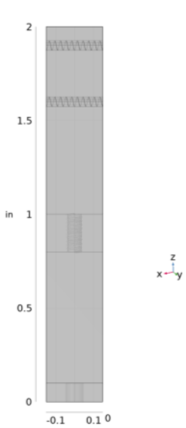
2
1.5
in 1
0.5
0
-0.1
0.1
0
z
x
y

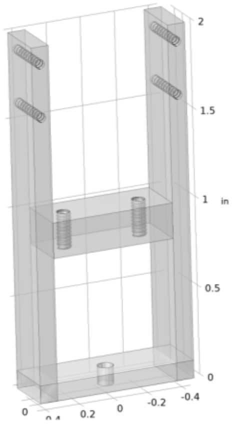
2
1.5
1 in
0.5
0
0
0.2
0
-0.2
-0.4

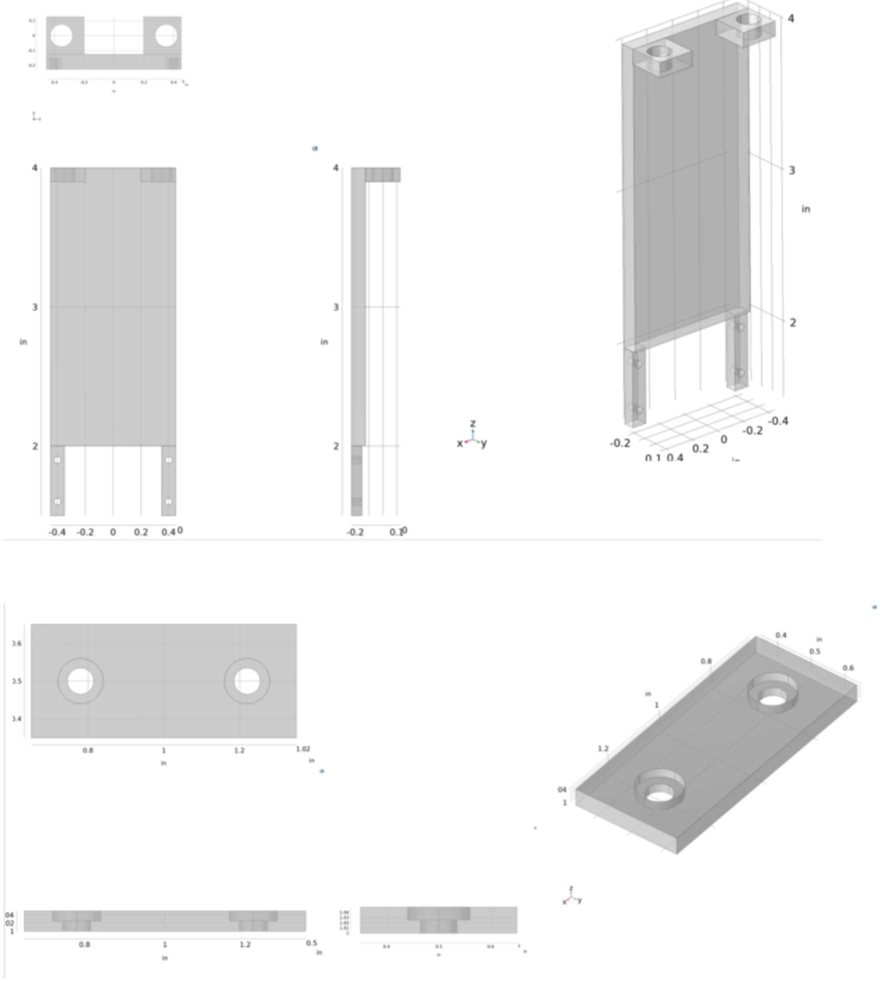

Figure 8-5. multi views of part(9): customized copper structure for sample holder of probe 2 and each individual smaller components.

8.2. Tips for getting better noise spectra

1. Always be careful about the noise from ground, especially PPMS ground. We found that some instruments generate large noise on their ground, and connecting their ground to amplifiers' ground would pick up large background noise. The most effective way is to isolate the amplifiers' input ground with PPMS ground.
2. Twisted pair wire is necessary for noise measurement. Any loop between the noise measurement wire can pick up environmental noise, and this noise might change with time and cause large variations of measured signal.
3. Customized noise detector could help to find noisy source. We made coil(10-20 1 inch diameters loops) and attach it to the end of a rod, we directly read noise spectrum from the coil to find the noisy source in lab. We did find a UPS in our lab generating a few strong noise peaks while working when we move the coil close to the UPS.
4. Use two twisted pair wires to connect noise from samples. When sample resistance and voltage signal are small, we need to consider the thermal noise from the probe wires. One way to solve this problem is to use two twisted pair wires, each connects the sample and one amplifiers chain, the thermal noise from two twisted probe wires will be eliminated by cross-spectrum because they are uncorrelated to each other.
5. If there is still noise background, try to remove this by measuring noise increase/decrease. If the background noise is bias independent, we can measure the noise increase at given bias compared to zero bias. If the background is temperature independent, we can measure thermal noise at different temperature to find the background noise.
6. Shielding is important. We recommend checking ground shielding on the probe to the amplifiers' input ground, and make sure it is connected. Disconnection of ground shield might increase background noise based on our experience.

7. Some noise peaks at 60×n Hz where n=1,2,3…. Is related to the US power frequency, and are hard to remove. One practical method is to remove the data at these frequencies and even 60×n±5 Hz.
8. The system also picks up the thermal noise from the current limiting resistors, and the value is related to the sample resistance. When sample resistance is much smaller than the currently resistor, we don't need to worry about this. However, if the sample resistance is not much smaller than current limiting resistor, we need to calculate the contribution from thermal noise of current limiting resistors. One of the solutions is to put the current limiting resistors together with sample, so the temperature of resistors would be much lower.

8.3. Reactive ion etch parameters tuning

The performance of RIE vary with film and working conditions of RIE instruments. We found that the parameters we used in 6.1.2 does not work well on the new $YbRh_2Si_2$ film, it is either because the film property changed or the maintenance of RIE instrument changed the working conditions. We adjust the parameters including working pressure, RF power, ICP power and time duration. Here I explain how each parameter change the etching result, and final parameters we used for etching the nanowire in section 6.8.3.

Pressure is a very important parameter that decide the mean free path of Ar ion. Lower pressure means lower collision chance between Ar ion before hitting the sample, and this means the Ar ion will have relatively high energy and the etching process is more anisotropic. However, if the pressure is too low, the instrument will not be able to generate plasma. For our instrument, the lower limit is around 1.7 mtorr and we decided to use 2 mtorr for our experiment.

RF power for our instrument is used to generate DC voltage bias on sample and accelerate the Ar ion. However, the voltage generated on sample is also related to the plasma density, so for the parameters tuning process, we always adjust ICP power first, then adjust the RF power to make the DC bias constant(around 400V).

ICP power is mainly used to generate Ar plasma and higher plasma density leads to higher etching rate, however, it can affect how anisotropic the etching is. As shown in Figure 6-1, ICP power can generate fast switching magnetic field, and the switching field will generate circular electric field in the chamber. The accelerated Ar ion will suffer the force in horizontal direction and the etching process would be isotropic. We found under etch issue when we fabricate nanowire on new film after RIE instrument maintenance.

Here I show the etching results on Si using two different parameters setting. Parameter 1: RF power 190 W, ICP power 600 W, Pressure 2 mtorr, Flow 20 cc, temperature 13 degree, time 2 minutes. Parameter 2: RF power 120 W, ICP power 100 W, Pressure 2 mtorr, Flow 20 cc, temperature 13 degree, time 12 minutes. The etching result are shown in Figure 8-6. It is clear that the etching using parameter 2 is more anisotropic. And we decided to use to fabricate the nanowires on new film in section 6.8.3.

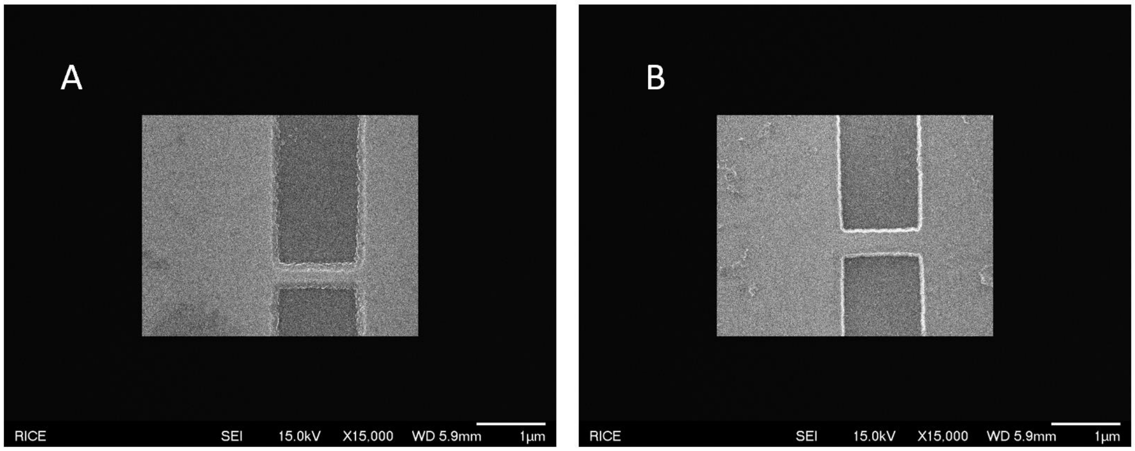

Figure 8-6. RIE etching comparison using parameter 1(A) and parameter 2(B) using Cr as hard mask and removed by Cr etchant.

The etching rate use also recalculated using parameter 2 and etching for 6 minutes. The results are shown in Figure 8-7. The etching rate is around 33 nm for 6 minutes, to make sure etching away exposed $YbRh_2Si_2$, we increase the etching duration to 15 minutes when fabricating the nanowire device in section 6.8.3.

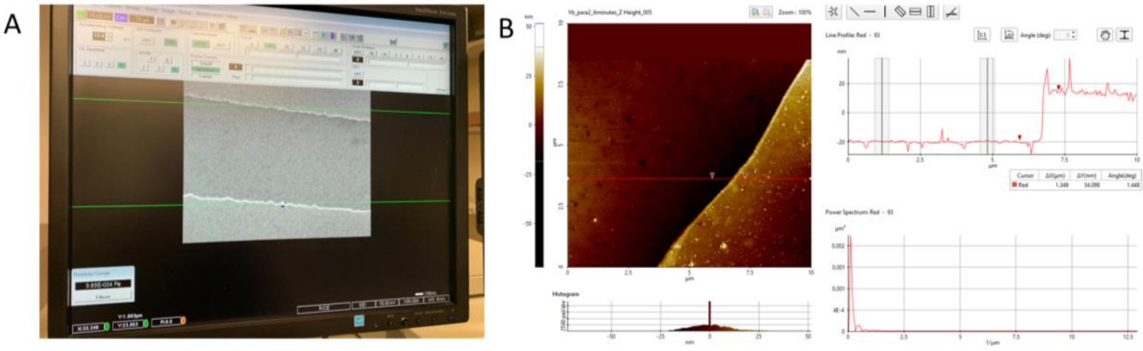

Figure 8-7. RIE etching test using new parameters on new film. (A) etched strip shape imaged by SEM. (B) AFM image across the edge showing etching rate around 33 nm for 6 minutes.